Abstract

Title of Document:	New Sensing Modalities for Bacterial and Environmental Phenomena
	Jordan Foster Phillips Betz, Doctor of Philosophy, 2013
Directed By:	Professor Gary W. Rubloff, Minta Martin Professor of Engineering, Department of Materials Science & Engineering and Institute for Systems Research

Intercellular communication is a ubiquitous phenomenon across all domains of life, ranging from archaea to bacteria to eukarya. In bacteria, this is often achieved using small molecules that allow bacteria to sense and respond to environmental cues about the presence, identity, and number of neighboring bacteria. This confers survival and competitive advantages to bacteria by providing a coordinated, population-scale response to a given stimulus in the environment.

This dissertation describes the development of a microfluidic system for immobilizing and culturing of cells that also enables control over the genetic composition of the bacteria and their subsequent response to environmental stimuli via a new nonviral nucleic acid delivery mechanism. This nonviral nucleic acid delivery occurs outside the parameter space of traditional nonviral nucleic acid delivery methods such as electroporation and chemical transformation. The bacteria are immobilized in an optically clear alginate hydrogel which simulates the physical and chemical environment normally experienced by bacteria in a biofilm.

Complementing the microfluidic cell culture work, surface enhanced Raman spectroscopy (SERS), a label-free vibrational spectroscopic technique that lends itself well to use in aqueous systems, was used to detect bacterial signaling molecules. SERS was performed with three different examples of bacterial communication molecules: the universal quorum sensing molecule autoinducer-2 (AI-2), the species-specific *Pseudomonas* Quinolone Signal (PQS), and the stationary phase indicator molecule indole. SERS substrates were formed by galvanic displacement, a substrate fabrication method that can be adapted to many SERS applications.

Taken together, these new sensing modalities represent a step toward developing systems that allow researchers to investigate, understand, and ultimately control a cell's response to its environment.

NEW SENSING MODALITIES FOR BACTERIAL AND ENVIRONMENTAL PHENOMENA

By

Jordan Foster Phillips Betz

Dissertation submitted to the Faculty of the Graduate School of the
University of Maryland, College Park, in partial fulfillment
of the requirements for the degree of
Doctor of Philosophy
2013

Advisory Committee:
Professor Gary W. Rubloff, Chair
Professor William E. Bentley
Professor Gregory F. Payne
Professor Herman O. Sintim
Professor Ian M. White

Dedication

To my wife Yelena and my children Maria and Gabriel

Acknowledgments

I had an incredible amount of help and support to get to where I am today, typing up the last few words of this dissertation. I tried to acknowledge everyone involved in the work in the respective chapters to which they contributed, and hopefully I didn't forget anyone. I would like to take some space here to thank several people who have contributed greatly to this dissertation.

First, I thank my family for all their love and support. My wife Yelena, in particular, has been instrumental to my success in graduate school. She has made countless sacrifices to make this possible, picking up the slack when I had to stay all night taking time points, travel to a conference, or lock myself in my office to meet a deadline. My kids have also been very understanding and supportive when "papa can't play now, he has to finish writing".

My advisor, Gary Rubloff, has been incredibly supportive of the wild and crazy directions in which I took my project. He gave me a lot of leeway in designing these experiments and trying out new things. He also constantly challenged me to justify the experiments and come up with clearer explanations for my results, both of which have helped me grow as a scientist and a communicator of science (arguably one of the most important aspects of research). I really appreciate all the time and effort he put into my professional development.

I have received a great deal of assistance and advice from the members of my committee as well. They have been generous with providing feedback and advice with manuscripts and abstracts, allowing me to make use of the equipment and personnel in

their laboratories, and of course sharing their insight and experience to help me get unstuck when I got stuck. The open and collaborative environment that they have fostered has certainly enriched my experience as a graduate student, and is something I plan to emulate throughout my research career.

I am grateful to the members of the Maryland Biochip Collaborative. The postdocs and grad students that have made up the Biochip Collaborative over the years have helped make my graduate career a fun and interesting one. Our monthly Biochip meetings were a great forum to learn about the research going on in our collaborators' labs, bounce new ideas off one another, and also practice our scientific presentation skills. The research I conducted as a graduate student has been highly interdisciplinary and collaborative, and these graduate students and postdocs have made that possible by teaching me the nuts and bolts of what eventually became my thesis.

My labmates in the Rubloff Group, both past and present, have been a continuous source of ideas and encouragement throughout my graduate career. I learned the overwhelming majority of what I know about microfluidics and microfabrication from past group members, and even picked up a thing or two about ultrahigh vacuum technology and atomic layer deposition (probably by osmosis). I hope I was able to contribute to your research experience at least some fraction of what you have contributed to my project over the years.

Research doesn't happen by itself, and I acknowledged the funding agencies that supported the research in each chapter. However, I want to make a special note of the generosity of the Robert W. Deutsch Foundation, which has supported the research of the

Maryland Biochip Collaborative throughout my entire graduate career. This support has given us great flexibility to pursue new and interesting avenues of research as they arise.

Thank you all – family, friends, and mentors – for making this work possible.

Contents

Chapter 1: Introduction and Motivation

This chapter will provide a brief introduction to the field, describe the overall motivation for the work, and provide some context for the research detailed in this dissertation. Each chapter is designed to be relatively self-contained, with an abstract, introduction, and experimental section preceding the results and discussion to provide appropriate background and context.

Introduction

Intercellular communication is a ubiquitous phenomenon across all domains of life, ranging from archaea to bacteria to eukarya. In bacteria, one such communication process is called “quorum sensing”. Quorum sensing confers survival and competitive advantages to bacteria by providing a coordinated, population-scale response to a given stimulus in the environment. Two quorum sensing related behaviors that are of immediate interest and relevance to the biomedical and clinical communities are biofilm formation and production of virulence factors[1].

Biofilms are communities of bacteria that adhere to a surface through a sticky extracellular polymer matrix composed primarily of polysaccharides, but also incorporating proteins and nucleic acids. This extracellular polymeric substance, as it is called, protects the enclosed bacteria from a host’s immune response, and slows diffusion of drugs such as antibiotics through the biofilm[2]. Biofilms can form on almost any surface, and the CDC estimates that biofilms are present in almost two thirds of all bacterial infections[3]. This places additional financial and manpower burdens on an

already stressed healthcare system in the United States. In addition to the direct costs incurred from extended hospital stays, additional treatment by doctors and nurses, these infections require higher doses of more powerful antibiotics[2], indirectly leading to increased antibiotic resistance. Given the high cost and diminishing returns of producing new antibiotics relative to other possible drug candidates, pharmaceutical companies have increasingly shied away from developing new antibiotics. Without addressing this problem, this portends an untenable situation in which the current healthcare system applies selective pressures toward increased antibiotic resistance in bacteria while fewer and fewer new antibiotic treatments are developed and commercialized, leading to a potential crisis in the medical community.

In recent years, several research groups have begun to address this problem by researching the quorum sensing mechanisms that modulate biofilm formation and virulence factor production. The main hypothesis behind this approach is that understanding quorum sensing pathways and phenomena will allow researchers to design new drugs and strategies to interrupt and "rewire" quorum sensing, preventing invading bacteria from reaching a population density high enough to induce biofilm formation or virulence factor production. This would allow a host's immune system to clear the infection before it progressed to a stage where antibiotics were needed, with the added benefit of not applying a selective pressure on the bacteria toward those mutants immune to the effects of the autoinducer molecules that govern quorum sensing behavior. By avoiding the most common antibiotic mechanisms (e.g., inhibiting the formation of cell

walls, protein synthesis, or DNA synthesis), resistance to these new drugs and methods should not arise as quickly if at all.

However, the autoinducers that govern these cooperative behaviors tend to be small molecules or oligopeptides[1] with relatively limited methods for detection. Intrinsic fluorescence is minimal in the vast majority of the autoinducer-1 (AI-1) and autoinducer-2 (AI-2) families of compounds, and would be indistinguishable from other amino acid fluorescence in the case of the autoinducing peptide (AIP or AI-3) family of oligopeptides. Researchers have used molecular biology and genetic engineering techniques to circumvent this limitation by introducing genes for the production of fluorescent proteins into the operons that govern the synthesis, sensing, and transduction of the autoinducers, but this technique too has its own limitation. Fluorescent proteins take time to be synthesized, to fold properly, and to develop the fluorophore that gives them their fluorescence. In the case of the most commonly used fluorescent protein, green fluorescent protein (GFP), the folding and maturation time has been estimated to be on the order of 1.5 to 2 hours, which is effectively 2-4 generations of bacteria. Other methods that have been developed to detect autoinducers are offline methods that can take hours to perform. A label-free detection method would provide a higher resolution picture of quorum sensing dynamics, and allow for researchers to fine-tune their approaches and develop new experiments to better understand bacterial quorum sensing.

Motivation

The initial motivation for this work was to develop a microfluidic system that would enable researchers to immobilize cells at specified points in a microfluidic device and detect signaling molecules produced by one population as they traveled to another population of cells, shown schematically in Figure 1-1. This would give researchers a way to detect and better understand the signaling phenomena that can lead to increased virulence factor production and antibiotic resistance. This could potentially have downstream implications in monitoring and treatment of opportunistic pathogenic bacteria that form biofilms and communicate via quorum sensing, such as *Pseudomonas aeruginosa* in the case of patients with cystic fibrosis[4].

We had originally envisioned using a label-free detection method for these molecules, because the development of a system capable of the label-free detection of autoinducers would be a significant improvement over current technologies. A label-free method offers researchers a more accurate picture of cellular processes than a method requiring a label. Labeling methods, most commonly exemplified by fluorescent labeling of molecules using reactive esters of fluorophores, introduce a new variable into the system under study. Given that fluorophores tend to be bulky aromatic molecules, this can change the physicochemical properties of the molecule under study, potentially leading to less accurate results. Furthermore, a label-free detection system has the potential to be more broadly applicable than a specific label, making this useful to other researchers as well.

Powerful analytical techniques such as chromatography, mass spectrometry, and enzymatic methods tend to be limited to *ex situ* analyses. A sample must be collected and

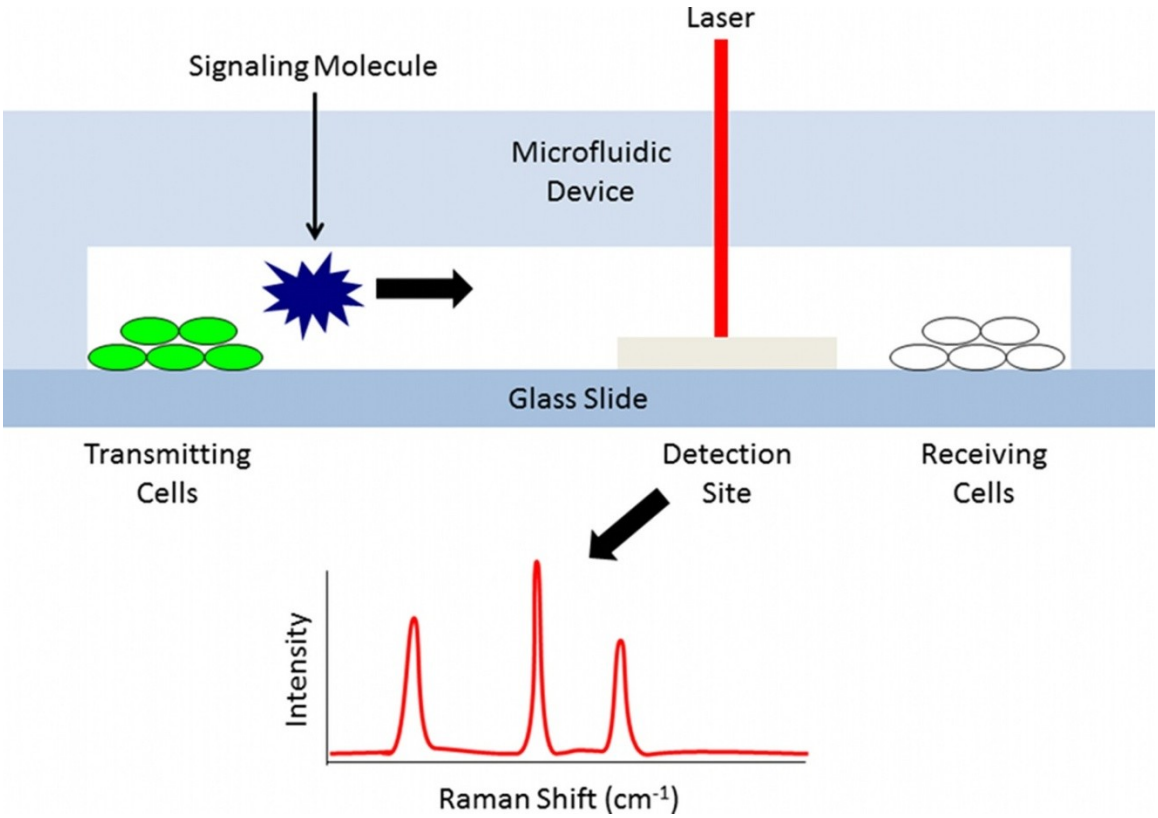

Figure 1-1. Schematic overview of the original proposed device. Two populations of cells, a "transmitting" population that produces an intercellular signaling molecule, and a "receiving" population that senses and responds to the signaling molecule. In between the populations is a detection site, which is excited by a laser in this case for surface enhanced Raman spectroscopy.

prepared prior to being analyzed by these methods. This adds time and complexity to the analysis while possibly disrupting the system during the sampling process. By using a surface enhanced vibrational spectroscopy, which is inherently label-free, in conjunction with transparent packaging materials, this system would provide a significant improvement in spatial and temporal resolution of intercellular signaling phenomena, allowing for near real-time monitoring and spatial resolution governed by the substrate and microchannel geometry. Surface enhanced vibrational spectroscopies, such as surface enhanced Raman spectroscopy (SERS) have the added advantage of not requiring an affinity molecule of some sort, as many other label-free methods do. This system would be applicable to detection of other molecules beyond autoinducers, and could readily be combined with other cell culture systems beyond model bacterial biofilms.

Research context

To achieve our goal of integrating cell culture and *in situ* detection in microfluidics, we needed to develop three main technologies:

1. A method to immobilize populations of cells at a desired point in space and time
2. A method to control a cell's response to a chemical signal in its environment
3. A label-free method to detect intercellular signaling molecules

Cell immobilization

The ability to put a specific thing in a specific place at a specific time opens up a plethora of experimental possibilities. Our work within the Maryland Biochip Collaborative has focused on the integration of biological molecules with microfabricated devices to do just

that. In fact, techniques developed within the Biochip Collaborative detail the electrodeposition of populations of cells within a calcium alginate hydrogel, as well as the underlying chemical mechanism responsible for this process[5-7]. However, the technique involves creating a hydrogel laden with $CaCO_3$ particles, which block light transmission, leading to a system in which bright field optical microscopy does not allow a researcher to obtain information about the state of the cells in the hydrogel, and fluorescence microscopy is limited to a small segment of the hydrogel.

In Chapter 2, we describe a technique that allows for the entrapment of cells in a calcium alginate hydrogel that is optically clear- no $CaCO_3$ particles are present in the layer containing the cells. This enables a researcher to use both optical and fluorescent microscopies to observe and interrogate cell populations. It also enables the use of confocal microscopy to image the entirety of the gel, giving a 3D picture of cell behavior throughout the gel.

Cell response to environmental signals

While not explicitly required in the "immobilize cells and detect signaling" paradigm, the ability to control a cell's response to a specific environmental signal can help immensely in debugging the proposed experimental system. This is traditionally done *ex situ* using molecular biology methods that have been developed and optimized over the last three to four decades. Controlling a cell's response to an environmental signal has uses above and beyond the initial motivation of detecting cell signaling- cells can have altered sensitivity to a specific molecule, or a sensitivity to a molecule can be introduced where it did not

exist before, effectively "teaching" a cell to speak a new "language" [8, 9]. This process is a mainstay of modern biotechnology and synthetic biology, and is used extensively within the research of the Maryland Biochip Collaborative.

In Chapter 3, we describe a new way to deliver DNA to a population of bacteria while simultaneously immobilizing them in a calcium alginate hydrogel. In fact, the method is directly adapted from our previous work electroaddressing populations of cells at specific sites. This allows researchers to not only control where and when they put something somewhere, but also control how it responds to a specific environmental cue.

Label-free detection method

Raman spectroscopy is a form of vibrational spectroscopy that allows a researcher to get a vibrational "fingerprint" of a molecule without the need to label it with a fluorophore or affinity molecule (*e.g.* an antibody). It is a powerful analytical technique but is hindered by relatively low signal. This limitation is often overcome by using surface enhanced Raman spectroscopy (SERS), a technique that takes advantage of the interaction of photons with nanoscale metal features, resulting in an enhancement of the Raman signal by several orders of magnitude. SERS also offers the advantage of requiring little to no sample preparation prior to spectrum acquisition. These characteristics made it a promising sensing method to detect intercellular signaling molecules.

In Chapter 4, we describe the development of a simple and inexpensive SERS substrate fabrication method based on a reaction called "galvanic displacement" that provided good enhancement of Rhodamine-6G (R6G), a popular SERS probe molecule

due to its large Raman cross-section. We demonstrate the utility of this method to form highly enhancing nanoscale metal features on a number of surfaces, including that of a penny and a dime. We also describe an exciting result that indicates that galvanic displacement, normally a highly variable and random process, may be made more reproducible by controlling the oxide layer defects on the surface through which the nanoscale metal features form.

This SERS substrate fabrication method is also amenable to formation under fluid flow conditions, which would enable the on demand fabrication of SERS substrates within a microfluidic device. We designed and fabricated microfluidic systems that would allow us to test this, and attempted to detect 1 μM R6G flowing over the substrate formed in the microfluidic channel. Figure 1-2 shows the result, comparing first the SERS spectrum from 1 μM R6G on a substrate formed on a penny (Figure 1-2a) and then showing the spectrum from inside the device (Figure 1-2b). The loss of two orders of magnitude worth of signal-to-noise ratio (SNR) for one of the best SERS probes meant that *in situ* detection of signaling molecules was effectively doomed using these substrates formed by galvanic displacement.

Chapter 5 details our attempts to detect three classes of intercellular signaling molecules: the AI-2 family of molecules, *Pseudomonas* quinolone signal (PQS), and indole. We had success with detecting AI-2 using SERS, which represents a step in the right direction for monitoring intercellular communication using label-free detection methods. However, we were unsuccessful in using these specific SERS substrates to detect these signaling molecules under physiologically relevant conditions. The results

described herein will help to inform future label-free detection methods for intercellular signaling molecules.

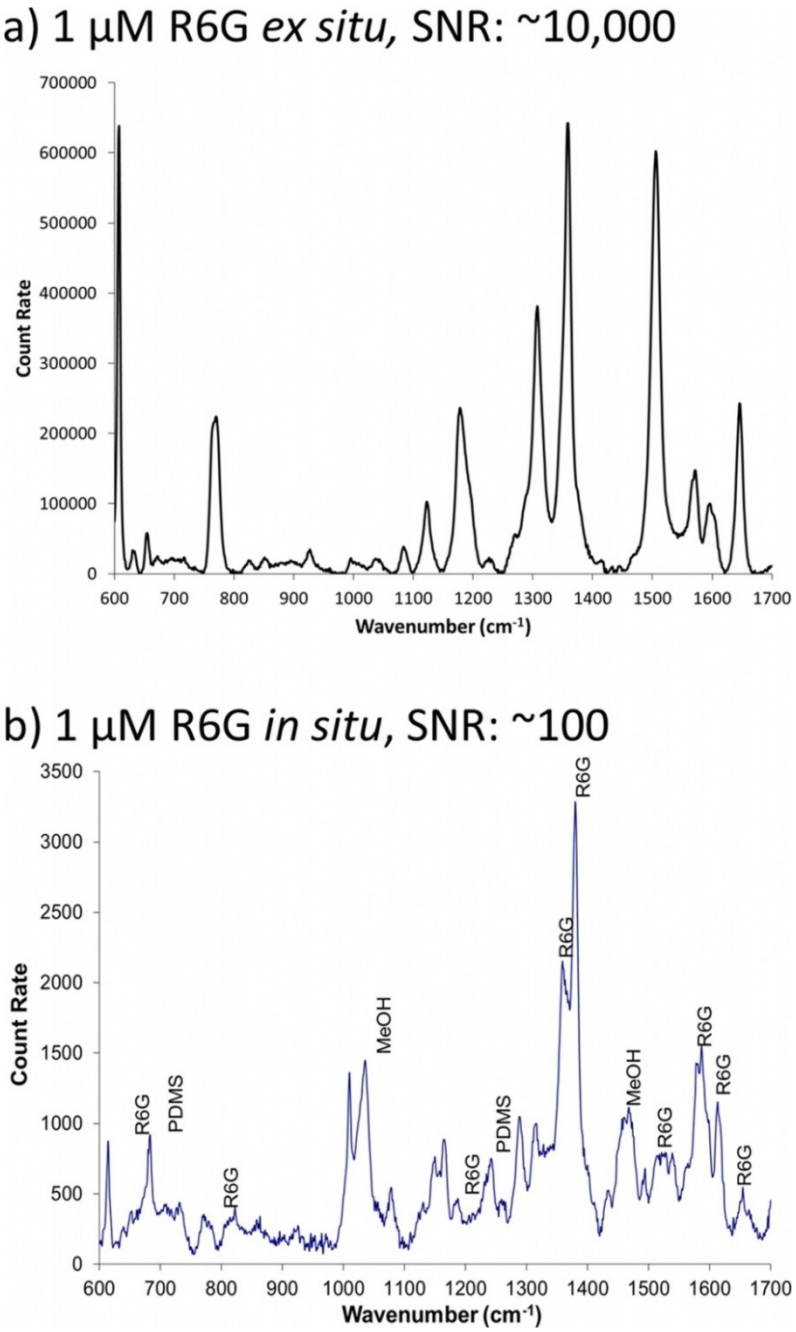

Figure 1-2. Comparison of *ex situ* and *in situ* SERS spectra of 1 µM Rhodamine-6G. a) *Ex situ* spectrum acquired on galvanic displacement substrate. b) *In situ* spectrum acquired on galvanic displacement substrate in microfluidic device with a flow rate of 100 µL/min. Abbreviations: R6G: Rhodamine-6G, PDMS: polydimethylsiloxane (from microfluidic device), MeOH: methanol (R6G solvent).

Chapter 2: Optically Clear Calcium Alginate Hydrogels for Localizing, Observing, and Interrogating Populations of Cells

Note: The contents of this chapter were primarily reproduced directly or adapted from Betz, J. et al., *Optically clear alginate hydrogels for spatially controlled cell entrapment and culture at microfluidic electrode surfaces*, Lab on a Chip, 2013. **13**: p. 1854-1858, with permission.[10]

Chapter abstract

This chapter describes an innovation in the immobilization, culture, and imaging of cells in calcium alginate within microfluidic devices. This technique allows unprecedented optical access to the entirety of the calcium alginate hydrogel, enabling observation of growth and behavior in a chemical and mechanical environment favored by many kinds of cells. Applications are demonstrated in the immobilization of multiple cell types and the use of this technique for studying quorum sensing phenomena in bacteria.

Introduction

The ability to culture a wide variety of cell types is increasingly important to the microfluidics and lab-on-a-chip community[11], and careful selection of the cells' supporting material is essential[12]. The mechanical and chemical environment in which a cell is cultured is critical to a cell's ability to grow and thrive[13]. A calcium alginate

hydrogel has been demonstrated to provide the mechanical and chemical environment necessary to support cell growth in a wide variety of cell types[14, 15], including bacterial, yeast, insect, and several mammalian cell lines. There are several examples of alginate hydrogels being used in conjunction with microfabricated systems[16-26], and the majority of these systems encapsulate cells within calcium alginate microspheres formed by variants on hydrodynamic focusing and microfluidic emulsion techniques. While these systems are capable of creating relatively uniform, monodisperse hydrogels, tracking cell growth and behavior within these hydrogels over time becomes more challenging due to their spatially dispersed nature.

Our group has recently described a technique to entrap cells within a calcium alginate hydrogel formed via electrodeposition with $CaCO_3$ particles[5]. We then elucidated the underlying chemical mechanism of gelation[27]. We demonstrated that this technique can be used to culture cells at specified locations[6, 28] and with a given geometry[7, 29] within a microfabricated system. The electrodeposited calcium alginate hydrogels offer several advantages over the droplet microfluidics-based calcium alginate microspheres for time-dependent cell culture studies, such as the ability to control the hydrogel shape and spatial distribution of the cells; however, the incorporation of relatively large particles of $CaCO_3$ renders these hydrogels opaque to transmitted light[5, 27]. This biases the observation of the distribution of cells and limits the usefulness of optical methods, including powerful fluorescence microscopy techniques that have been developed over the years to interrogate and understand cellular systems. The hydrogels

can be made clear by immersing them in an acidic solution to dissolve excess $CaCO_3$[5], but this is not conducive to preserving the intrinsic activity of labile biological systems.

Figure 2-1 illustrates schematically an approach to overcome this limitation. We previously observed that a thin layer of calcium alginate gel can be triggered to assemble at the electrode surface, by the electrochemically-induced release of Ca^{2+}[27]. Here, we used this method to electrodeposit an initial, $CaCO_3$-rich, alginate film to serve as a Ca^{2+}-feeder layer. This feeder layer could then be contacted with a mixture of sodium alginate and cells, and an electrical input (anodic current) that induces the release of free Ca^{2+} from the feeder layer could trigger the formation a second Ca^{2+}-alginate film that was free of $CaCO_3$ particles and therefore optically transparent. Such a transparent film should allow a population of cells to be immobilized and observed over time using optical methods that are ubiquitous to biology.

Experimental

Microfluidic system fabrication

The fabrication of the sidewall electrode microfluidic device used for deposition and culture [6, 30] can be seen schematically in Figure 2-2 and can be described as follows: First, glass slides were soaked in piranha solution (H_2SO_4: H_2O_2 = 3:1) for 10 minutes followed by thorough rinsing with DI water (Figure 2-2a). Second, a bent (90º) metallic shadow mask with parallel slits (width: 1 mm) pattern was place onto the glass slide (Figure 2-2b). Multiple parallel electrodes were defined by angled thermal evaporation of chromium (Cr) (20 nm) and gold (Au) (100 nm) onto the top and the side of the glass

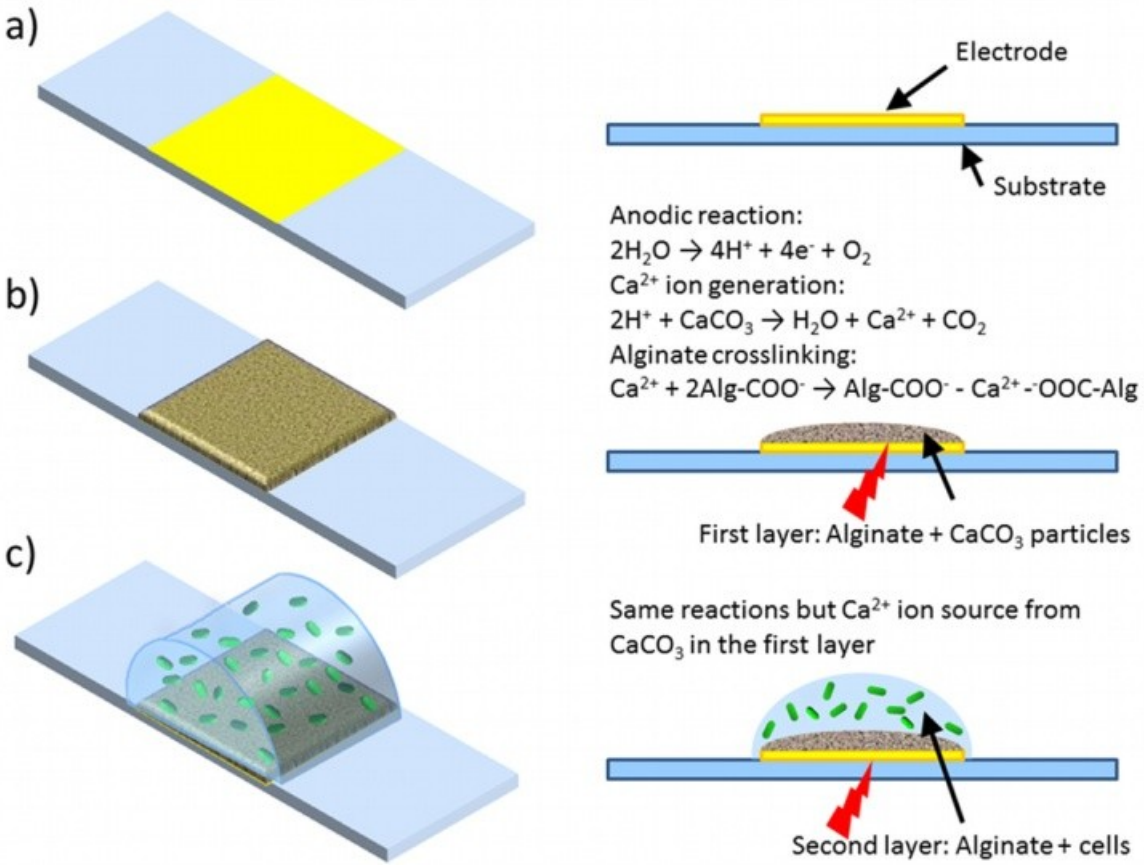

Figure 2-1. Schematic illustration of the method to deposit an optically clear alginate gel at an electrode address. a) A planar electrode is fabricated on a substrate. b) A thin calcium alginate hydrogel is deposited at an electrode address by generating a current between two electrodes, entrapping an excess of $CaCO_3$ particles. c) An optically clear solution of alginate containing cells is deposited by using the $CaCO_3$ particles from the first layer of alginate as a source for Ca^{2+} ions to gel the second layer.

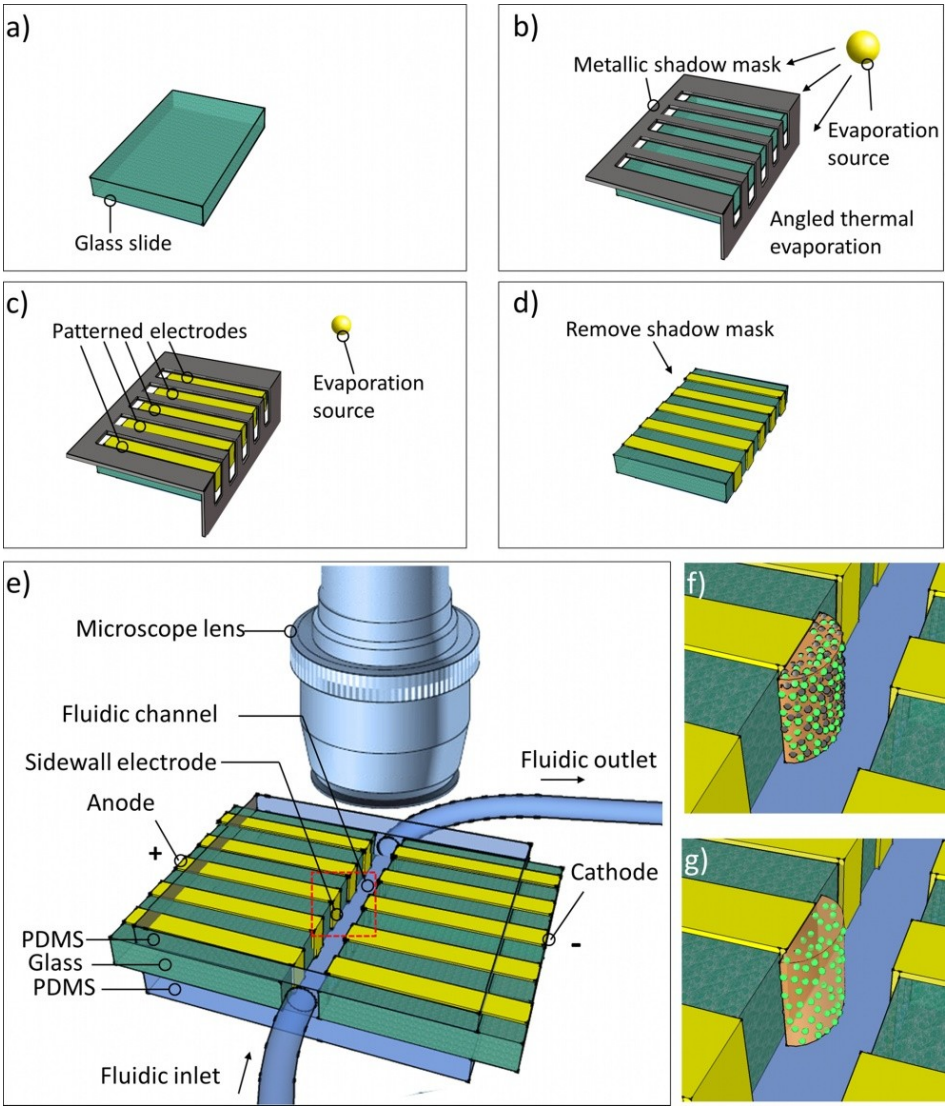

Figure 2-2. Schematic diagrams illustrating the fabrication procedure of transparent microfluidic device with built-in sidewall electrodes. (a) A glass slide is cleaned with piranha solution and DI water. (b) A bent metallic shadow mask with parallel slits pattern is placed on the glass slide. (c) Multiple parallel electrodes were defined by angled thermal evaporation of Cr and Au. (d) Patterned electrodes on the top and the side of the slide after removal of the shadow mask. (e) Schematic diagram of the microfluidic device with integrated sidewall electrodes. (f) Cell assembly with anodic electrodeposition of 1% alginate and 0.5% $CaCO_3$ particles. (g) Cell assembly with sequential, bilayer anodic electrodeposition of 1% alginate and 0.5% $CaCO_3$ particles.

slide (Figure 2-2c). Both the electrode width and the separation between electrodes are 1 mm (Figure 2-2d). Two glass slides with such patterned electrodes were placed side by side with a separation of ~1 mm (Figure 2-2e). They were permanently bonded to two thin layers of cured PDMS (Sylgard 184 Silicone Elastomer Kit, Dow Corning) with oxygen plasma treatment (pressure: 450 mTorr, forward power: 20W, Oxygen flow rate: 20 sccm O_2, plasma treatment time: 30 seconds) to form the ceiling and the floor of the channel (Figure 2-2e). The channel height is 1 mm, as defined by the glass slide thickness. The active sidewall electrode areas in the fluidic channel are 1 mm × 1 mm. PTFE tubing was then inserted into the channel to define the inlet and outlet of the channel. The connections between tubing and channel were sealed with PDMS gel and cured rapidly at 150 ºC on a hotplate. Planar gold electrodes (100 nm Au, 20 nm Cr adhesion layer) were fabricated on a Si wafer by standard microfabrication techniques.

Reagents

Sodium alginate and $CaCO_3$ were purchased from Sigma Aldrich. FluoSpheres green fluorescent microspheres (2 μm diameter) were purchased from Invitrogen. LB and ampicillin were purchased from Fisher Scientific.

Alginate solutions

A solution of 1% (w/v) alginate and 0.5% (w/v) $CaCO_3$ was prepared to act as a source for free Ca^{2+}. A solution of 1% (w/v) alginate was boiled for 15 minutes, cooled, and mixed with an equal volume of cells prepared as described above or a 0.1% suspension of the fluorescent microspheres in water.

Electrodeposition conditions

Single-layer gels of 1% (w/v) alginate and 0.5% (w/v) $CaCO_3$[5, 27] were deposited at a constant current density of 4 A/m^2 for 3 min. For the clear bilayer gels, a thin first layer with the same composition as the single-layer gel was deposited at a current density of 10 A/m^2 for 30 sec. The second, optically clear layer was deposited at a constant potential of 3 V for 3 min.

Cells, Plasmids, and Culture Conditions

Escherichia coli strain BL21 (DE3) were transformed with the pQE60-T5-DsRedExpress2[31] plasmid using standard electroporation methods[32]. For the initial depositions, *E. coli* were cultured overnight in LB medium supplemented with 50 μg/mL ampicillin at 37ºC while shaking at 250 rpm. Overnight cultures were inoculated 1:50 into fresh LB and grown to an OD_{600} of 0.4 before being mixed with an alginate solution.

For continuous monitoring of cell growth and behavior, transformed *E. coli* were cultured in LB medium supplemented with 50 μg/mL ampicillin and 10 mM $CaCl_2$ at a constant volumetric flow rate of 2.5 μL/min in a humidified incubator maintained at 37ºC. The devices were removed from the incubator and the media flow was stopped only for the time necessary to image the cells.

HCT-8 cells (ATCC) were cultured in RPMI1640 medium (ATCC) with 10% (vol/vol) horse serum (ATCC) at 37ºC in the presence of 5% CO_2 humidified air, according to ATCC specifications, resuspended in DPBS (Invitrogen), and stained with 2

μM calcein-AM (Invitrogen) for 1 hour. Excess dye was removed by centrifuging and resuspending in DPBS (Gibco) before mixing with alginate.

To investigate signaling, an engineered *E. coli* (W3110 Δ*luxS* Δ*lsrFG*)[9] strain (referred to as CT104) was transformed with both pCT6[8] and pET-DsRed using standard electroporation methods. Cells were cultured overnight in LB medium supplemented with 50 μg/mL ampicillin and 50 μg/mL kanamycin at 37ºC while shaking at 250 rpm. Overnight cultures were inoculated 1:100 into fresh LB and grown to an OD_{600} of 0.4 before being mixed with an alginate solution. CT104 cells were cultured in LB medium supplemented with 50 μg/mL ampicillin, 50 μg/mL kanamycin, and 10 mM $CaCl_2$ at a constant volumetric flow rate of 1 mL/hr in a humidified incubator maintained at 37ºC. The media in one device was supplemented with 10 μM chemically synthesized DPD, and the media in a second device was supplemented with 10 μM chemically synthesized nitrophenyl-DPD, an AI-2 analogue. DPD and the analogue were synthesized as previously described[33-35]. The devices were removed from the incubator and the media flow was stopped only for the time necessary to image the cells.

Optical and Fluorescence Microscopy

Bright field optical and fluorescence micrographs were acquired using a Zeiss LSM310 fluorescence microscope with a 5× air objective lens. The objective lens was located directly above the device and was focused on the anode surface in the channel. The optical micrographs were obtained with transmitted light coming from the bottom through the transparent PDMS layers. For fluorescence imaging, the FITC filter set

(Chroma) was used for the fluorescein-labeled microspheres and the TRITC filter set (Chroma) was used for the *E. coli* expressing DsRed. ImageJ[36] image analysis software was to analyze both the bright field and fluorescence images.

Confocal Fluorescence Microscopy and Analysis

Confocal images were acquired using a Zeiss LSM710 confocal laser scanning microscope in the Imaging Core Facility of the Department of Cell Biology and Molecular Genetics at the University of Maryland. A 10× air objective was used for the confocal stack acquisition of beads entrapped in the clear alginate hydrogel. A 40× oil immersion objective was used for confocal stack acquisition of HCT-8 and *E. coli* multilayers. Stack reconstruction and maximum intensity projections were created using Zeiss ZEN 2009 software. Analysis of fluorescence was performed using ImageJ.

Optical Density (OD) Calculation

An optical density for the cells in the alginate hydrogels was calculated using ImageJ. The same four hydrogels were measured for each time point. The region of the gel containing cells was outlined using the polygon selection tool and the grayscale intensity was measured. A blank was created by averaging measurements from 10 images of alginate hydrogels without cells. The optical density was calculated using the following equation:

$$OD = log_{10}(255 - sample) - log_{10}(255 - blank) \quad \text{(Equation 2-1)}$$

Results and discussion

Effect of electrodeposition conditions

The electrodeposition conditions directly impact the hydrogel characteristics. The initial deposition time for the bilayer is critical for ensuring adhesion of the hydrogel to the electrode surface. We found that for initial deposition times less than 30 seconds at a constant current density of 10 A/m^2, the hydrogels would delaminate under flow while culturing cells. 30 seconds of deposition was enough to create a first layer with enough $CaCO_3$ to gel a substantial second layer, nearly 600 μm thick during the 3V deposition. Increasing the deposition voltage above 3V for the second layer results in the formation of bubbles at the electrode surface due to electrolysis of water; this weakens the hydrogel adhesion to the electrode surface. Our empirical results indicate that the given deposition conditions provide a good balance between creating a first layer thin enough to maximize the amount of cells that can be entrapped within the second layer while still retaining enough $CaCO_3$ to gel the thick second layer. While we did not systematically investigate the deposition conditions in this work, we have previously demonstrated that both the electrodeposition current density and $CaCO_3$ concentration impact the resulting dimensions of the hydrogel[27].

Comparison with previous alginate gel entrapment method

Figure 2-3 shows a comparison of the hydrogels formed by the single layer method[5, 27], in which $CaCO_3$ particles are dispersed throughout the entire hydrogel (Fig. 2-3a), and the bilayer clear gel method, where a smaller first layer of $CaCO_3$-laden alginate

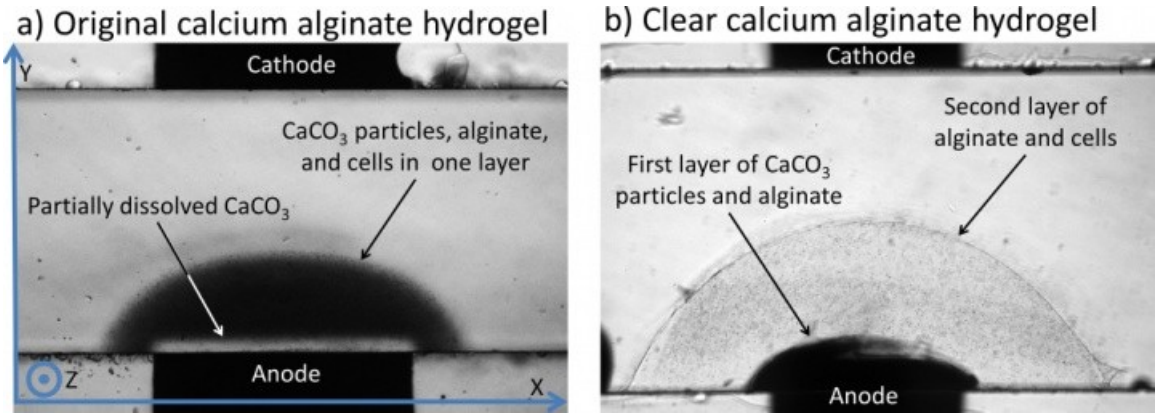

Figure 2-3. Comparison of calcium alginate gels formed from by the single and bilayer methods. a) Incorporating all components into a single layer limits the amount of information that can be obtained optically. b) Using a bilayer approach allows optical analysis of cells in the clear second layer.

provides free Ca^{2+} to a second, transparent layer free of $CaCO_3$ particles (Fig. 2-3b). These bright field micrographs, with light transmitted from below (or out of the page), clearly show a difference in the amount of light transmitted through the hydrogels. The single layer gel is almost entirely opaque, with the exception of a thin region near the electrode surface where the $CaCO_3$ particles are nearly completely dissolved by H^+ generated at the electrode surface during the electrodeposition process. The bilayer gel, on the other hand, allows almost all of the light through in the clear layer, with the exception of the light blocked or scattered by the bacterial cells. Given that fluorescence was clearly observed in previous reports of alginate-$CaCO_3$ electrodeposition[5-7, 27], we sought to determine the effect of $CaCO_3$ particles on the fluorescence intensity.

Confocal analysis of bilayer alginate hydrogels

Figure 2-4 shows the results of the confocal fluorescence microscopy that was employed to investigate the fluorescence observed from single and bilayer hydrogels. The hydrogels were decorated with fluorescent microspheres for easy visualization. The 2 μm bead diameter is similar to the size of most bacteria (approximately 1 μm in length) and somewhat smaller than eukaryotic cells, thus serving as a good approximation for several cell types in terms of size. Representative images of the single and bilayer gel depth profiles (from top down) are shown in Figure 2-4a and 2-4b, respectively. In the single layer gel, fluorescence can be observed down to approximately 400 μm and for this depth

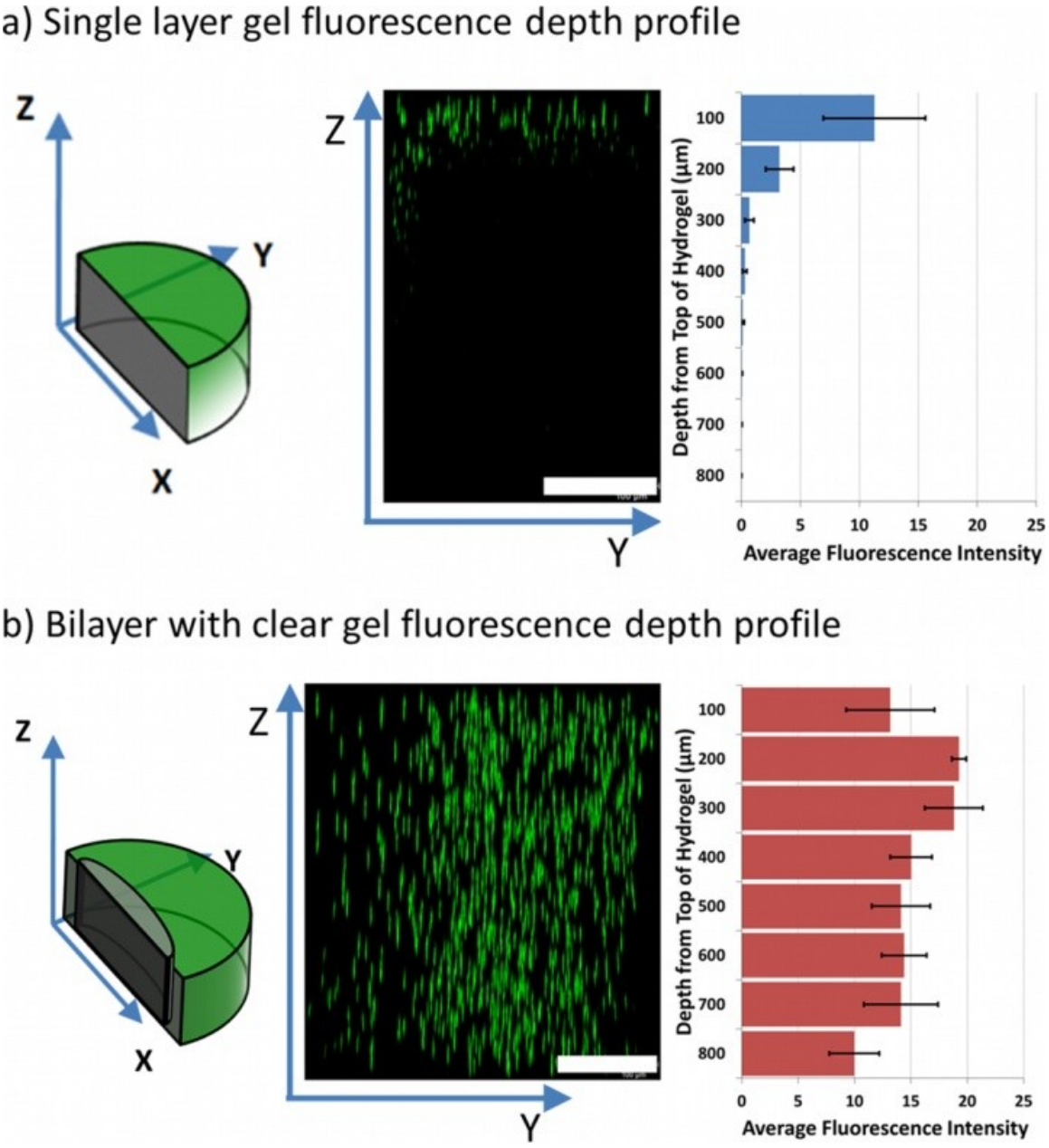

Figure 2-4. Fluorescent confocal microscopy analysis of fluorescence as a function of gel thickness. Representative depth profiles and average fluorescence observed in gels formed by a) the single layer method and b) the bilayer method. The scale bar in both images represents 200 µm. The image in b) is larger than a) because the bilayer gels are thicker than the single layer gels for the specified deposition conditions, as in Figure 2-3.

only very near the microchannel wall (y dimension near zero). This is attributed to (1) the opaque nature of the gel and (2) fluorescence from beads in the thin, optically-neutral region relatively free of $CaCO_3$ particles nearest the electrode surface, as observed in Figure 2-3a. That is, Figure 2-4 shows that, on average, the bilayer clear gels consistently exhibit more fluorescence than the single layer gels. This is confirmed using the maximum intensity projection of the hydrogels created using a single layer of 1% alginate, 0.5% $CaCO_3$ particles with fluorescent microspheres (Figure 2-5a) and the bilayer method described in this chapter (Figure 2-5b). These results indicate that $CaCO_3$ particles partially obscure the fluorescent signal. More than 70% of the total fluorescence observed in the single layer gels comes from the first 100 μm of the hydrogel and 90% within the first 200 μm.

On the other hand, the bilayer clear gel displays an almost linear relationship between cumulative fluorescence and depth, as shown in Figure 2-6. Each reconstructed confocal stack was converted to a 32-bit grayscale image, and the depth of the hydrogels was divided into 100 μm segments. The average grayscale pixel intensity was determined for each of the segments of each gel. The average grayscale pixel intensity of each of the four gels at each 100 μm depth increment was averaged. The near top-to-bottom uniformity in fluorescence indicates both that the deposition process and the optical properties are fairly uniform along the channel's vertical

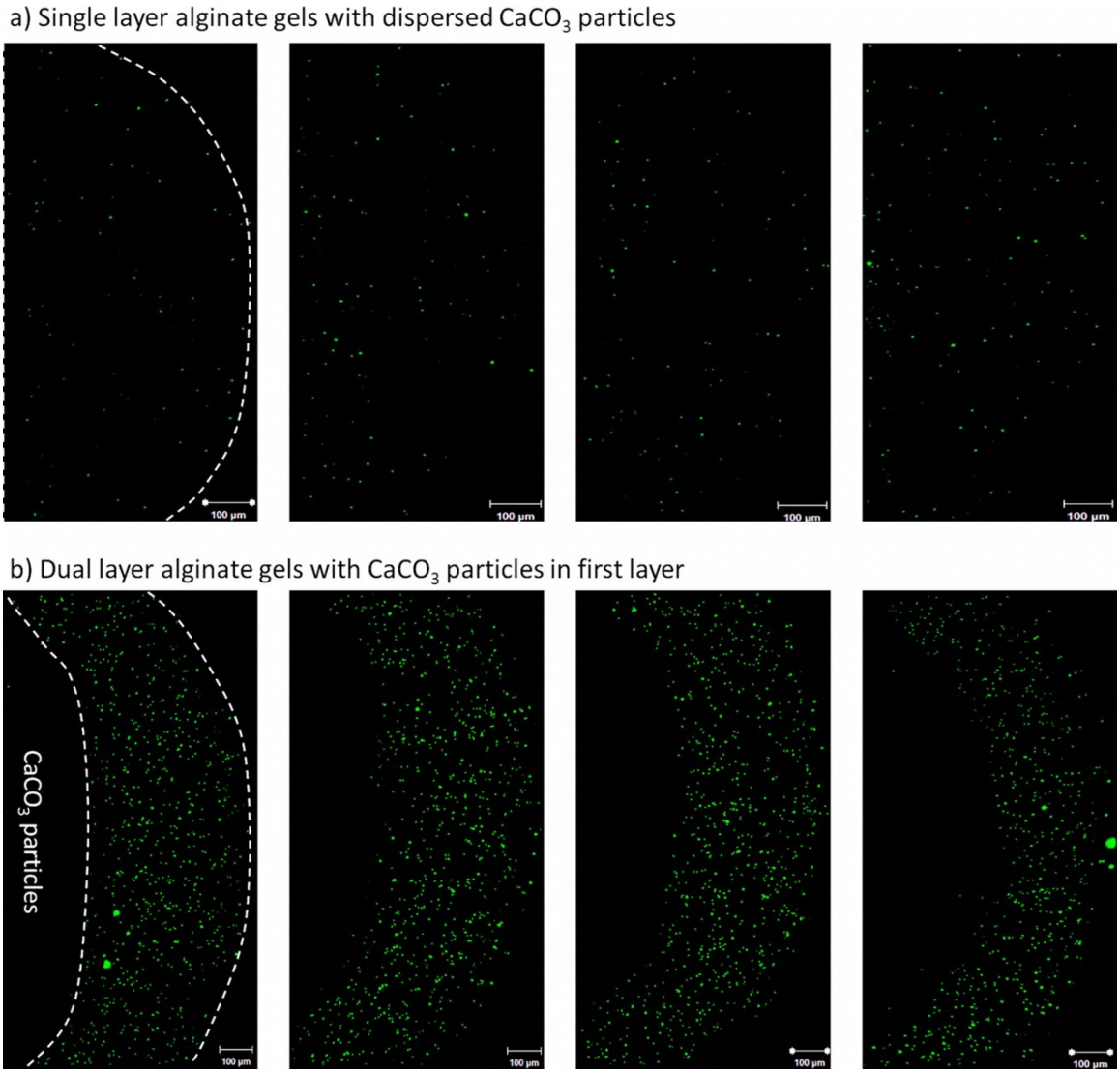

Figure 2-5. Maximum intensity images constructed from confocal stacks. a) Maximum intensities of the alginate hydrogels created with 1% alginate and 0.5% $CaCO_3$ particles dispersed throughout the hydrogels. The $CaCO_3$ particles block light from the fluorescent microspheres in the hydrogel below. The outline of the hydrogel can be seen faintly, and the first gel is outlined by the dashed white lines. b) Maximum intensities of the alginate created with a 1% alginate and 0.5% $CaCO_3$ particle first layer and a clear 1% alginate second layer. The first layer, devoid of fluorescent microspheres, can be seen as a dark region at the left edge of the images. The edges of the first gel have been outlined by dashed white lines. The anode is located on the left hand side of each image, and brightness and contrast were artificially enhanced.

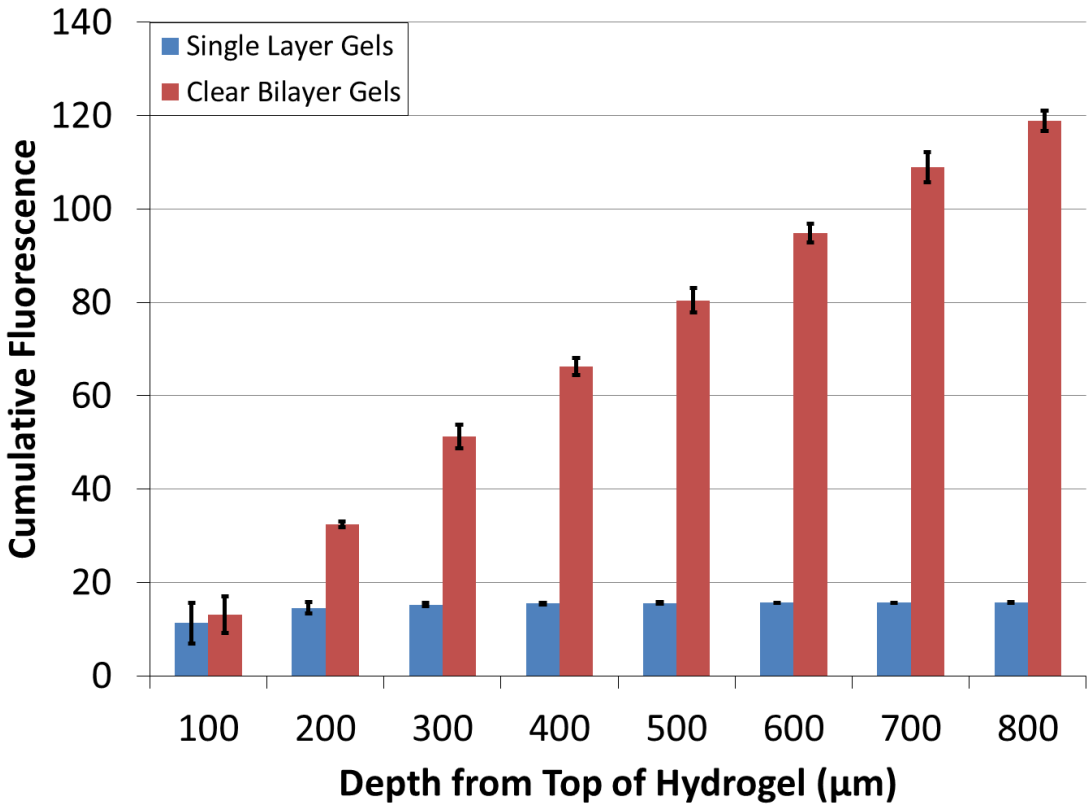

Figure 2-6. Comparison of the cumulative fluorescence in the single layer and clear bilayer gels. The cumulative fluorescence was measured for each 100 µm of depth of each hydrogel and added to the previous value, giving a measure of the total amount of fluorescence observed by confocal fluorescent microscopy. This figure indicates that the clear bilayer gels allow observation and analysis of hydrogel components at all depths, leading to a more accurate and possibly quantitative approach to observing cells entrapped in calcium alginate hydrogels in microfluidic devices.

dimension. Thus, this technique can be used to create calcium alginate hydrogels to entrap cells while also allowing optical access throughout the entirety of the hydrogel, enabling researchers to employ powerful optical analytical techniques to interrogate the cells entrapped and cultured within. Experiments taking advantage of this technique will be more accurate and more quantitative in terms of optical and fluorescent measurements.

Observing cell growth and behavior in situ

Figure 2-7 demonstrates the usefulness of these clear calcium alginate hydrogels for monitoring cell growth and behavior (represented by protein expression) over the course of time. Clear gels containing *E. coli* constitutively expressing DsRed, a red fluorescent protein, were cultured overnight. A control set of clear gels not containing any cells was also subjected to the same culture conditions to provide a baseline for comparison.

Optical density measurements

ImageJ image analysis software was used to calculate the optical densities of the hydrogels, giving a measure of cell density. A value of 255 is the maximum white value for a pixel, representing a complete transmission of light. Subtracting the grayscale value from 255 gives a measure of absorbance. Since the OD_{600} is an absorbance measurement relative to the absorbance of the blank expressed in a logarithmic fashion, the difference of the log value of the hydrogel to the log value of the blank gives a value equivalent to the optical density for a given light source. Using this method allows researchers to track cell growth without needing to place the device in a spectrophotometer, which has its own associated set of complications. One drawback to this method relative to the OD_{600}

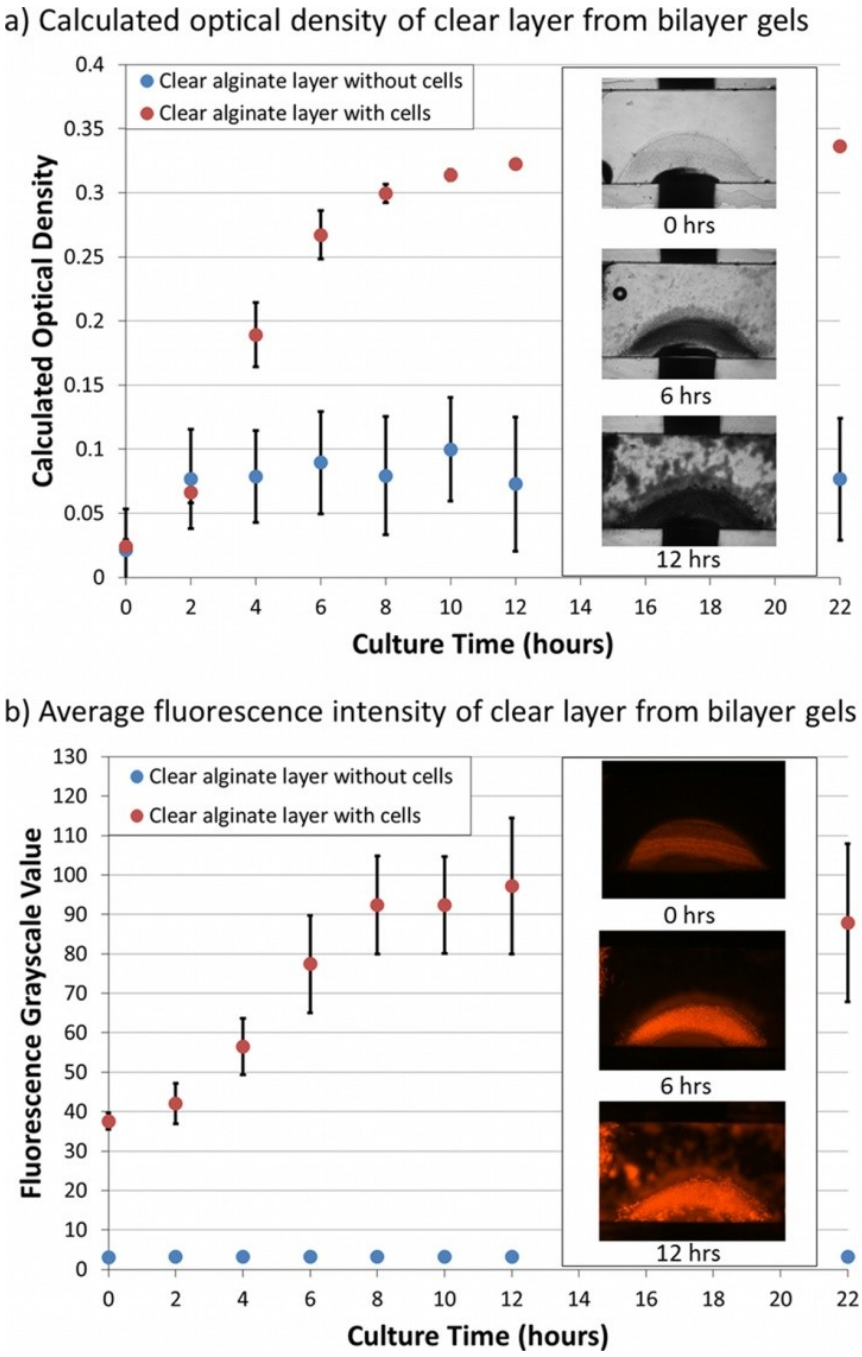

Figure 2-7. Monitoring cell behavior in bilayer gels. a) Optical density of cells growing in the hydrogels (red) as calculated from optical micrographs, some of which are shown in inset. b) Average fluorescence intensity of bacteria expressing DsRed in hydrogels as calculated from fluorescent micrographs, some of which are shown in inset. The blue marker symbols are from gels without cells.

is that for a given OD_{600}, the approximate cell density (number of cells per unit volume) is known. For this method, more extensive work would be required to determine this value and whether it is stable across different light sources.

Using this method of image analysis, the apparent variability in the hydrogels containing cells decreases over time. This is because a given volume of calcium alginate hydrogel can support only so many bacteria. As the cells grow and approach this upper limit, the optical image becomes uniformly dark, and the fluorescence image becomes uniformly bright. As each gel is measured and averaged, the initial, random differences in population density and protein expression are averaged out, and the variability decreases. There is little variability in the fluorescence image of alginate gels without cells, and this is solely due to system noise. The variability in the optical image of the alginate gels without cells arises from small inclusions of $CaCO_3$ particles in parts of one or two of the gels, but is relatively consistent over time, indicating that the increase in optical density arises solely from the presence and growth of cells in the alginate hydrogel.

Cell growth

The calculated optical density in Figure 2-7a allows researchers to follow trends in cell growth and density using only bright field microscopy and image analysis software without having to put the culture device inside a spectrophotometer or control for variables such as the thickness of the layer containing $CaCO_3$ particles. This allows researchers to fine-tune their experiments just by using image analysis methods- for

instance, enabling one to properly time the introduction of induction or other test media for use in protein expression or animal on a chip applications.

The gels containing *E. coli* exhibit a trend that follows a standard bacterial growth curve. After a brief adaptation or lag phase (~2 hours), the *E. coli* begin to grow more rapidly. The bacterial growth rates under these culture conditions are substantially lower than in shaker flasks (generation time of approximately 2 hours) likely due oxygen limitations intrinsic to such microfluidic environments. After reaching an appreciable cell density, the growth curve reaches a plateau. The plateau coincides with the maximum cell population held within the gel, as supported by the observation of cells escaping the hydrogel and colonizing other areas of the microfluidic channel (seen in both the optical and fluorescent inset images in Figure 2-7).

Cell behavior

Figure 2-7b shows that examining fluorescent protein production as a measure of cell behavior is likewise easy, requiring fluorescence microscopy and image analysis software. The fluorescent response of the cells follows the same growth curve trend as the optical density, which is to be expected given that these cells were constitutively producing DsRed prior to and during their culture in the clear alginate gels. These results indicate that entrapment within the clear alginate gel does not negatively impact protein production. Thus, this technique can be used to immobilize cells at a desired location within a microfluidic device with a given geometry[6] and thickness, culture the cells,

and observe the behavior of many types of cells using standard optical and fluorescent microscopic techniques.

Deposition of multiple cell types in multiple layers

Figure 2-8 shows an exciting application of this technique. The clear gels allow researchers to conduct more complex experiments that take advantage of powerful optical techniques such as confocal fluorescence microscopy to study the distribution and interaction between cells of different species or kingdoms. In this proof-of-principle demonstration, a multilayer structure of *E. coli* expressing DsRed is located underneath a group of human epithelial cells stained with calcein-AM, all deposited on a planar Au electrode (as opposed to the sidewall electrodes in Figures 2-1 through 2-7). This multilayer structure reinforces our suggestion that novel geometries and configurations of cell layers can be biofabricated in microfluidic systems, allowing researchers to create new models of physiological systems for studying complex phenomena such as the interaction of the microbiome with host cells.

Investigating intercellular signaling phenomena with bilayer alginate hydrogels

Given the overarching theme of developing a suite of new tools and techniques for investigating intercellular signaling phenomena and bacterial-environmental interactions, we set out to demonstrate the utility of this method for such investigations in microfluidics. CT104 is a strain of *E. coli* that has been engineered to be extremely sensitive to AI-2[9]. The strain lacks the ability to produce endogenous AI-2 due to the

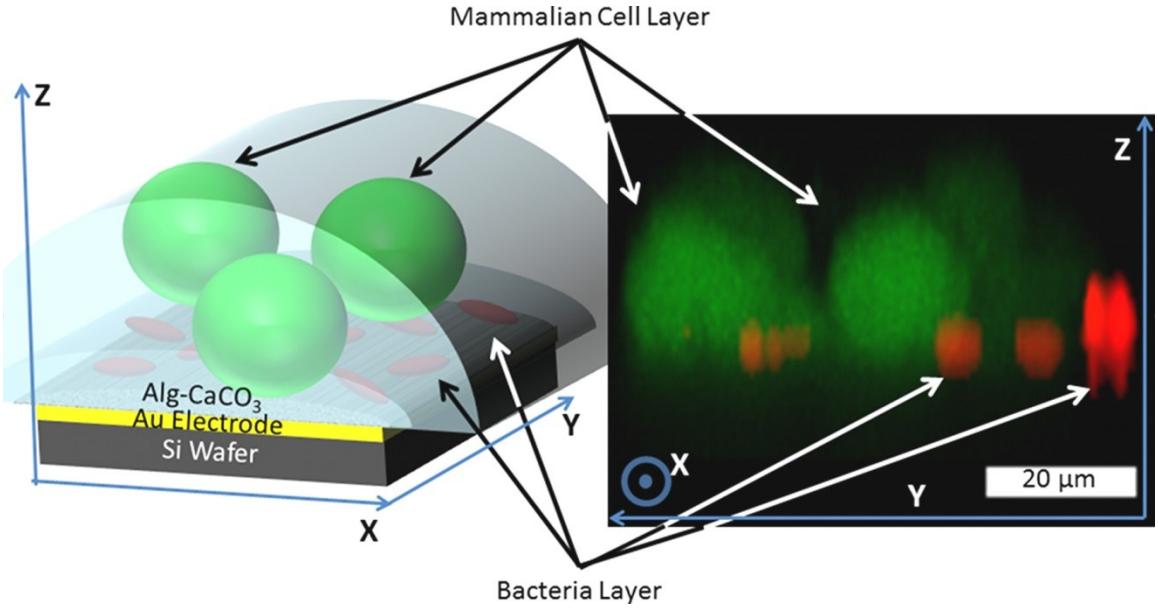

Figure 2-8. Sequential assembly of multiple clear layers of cells, including bacteria and human epithelial cells (HCT-8), on a planar electrode to study interkingdom interactions in a spatially controlled manner. A confocal fluorescent image stack, shown on right, enables investigation of cell distribution and behavior. Scale bar is 20 µm. Brightness and contrast of the fluorescent image was artificially enhanced.

Δ*luxS* mutation, and the introduction of the Δ*lsrFG* mutation reduces the strain's ability to degrade AI-2 within the cell. Thus any AI-2 within the cell is able to continuously de-repress LsrR, leading to an increased translation of any genes under the control of the *lsr* repressor. pCT6 is a plasmid that contains the T7 RNA polymerase under the control of the *lsr* repressor[8]. When CT104 is transformed with pCT6, this leads to an increased production of T7 RNA polymerase in response to the presence of AI-2. This has the effect of increasing transcription of any genes under the control of the T7 promoter, as in the case of the pET family of plasmids. In this case, CT104 with pCT6 and pET-DsRed will produce DsRed in response to exogenous AI-2.

Figure 2-9 shows a schematic overview and the results of the signaling experiment. CT104 with pCT6 and pET-DsRed were entrapped within the clear layer of a bilayer alginate hydrogel and cultured under three separate conditions, shown schematically in Figure 2-9a: LB media (control), LB media with 10 μM chemically synthesized DPD[35] (a physiologically relevant AI-2 concentration), and LB media with 10 μM chemically synthesized nitrophenyl-DPD[34] (an equivalent concentration of an AI-2 analogue designed to inhibit quorum sensing). Fluorescence images were analyzed using ImageJ, and normalized to the increase in fluorescence of the control due to nonspecific ("leaky") expression of the pET system. As would be expected, the cells in the device receiving LB with 10 μM DPD had a significantly increased overall average fluorescence (p=0.029, student's t, paired, one-tailed). The paired, one-tailed student's t test is an appropriate metric in this case due to *a priori* knowledge that the introduction of

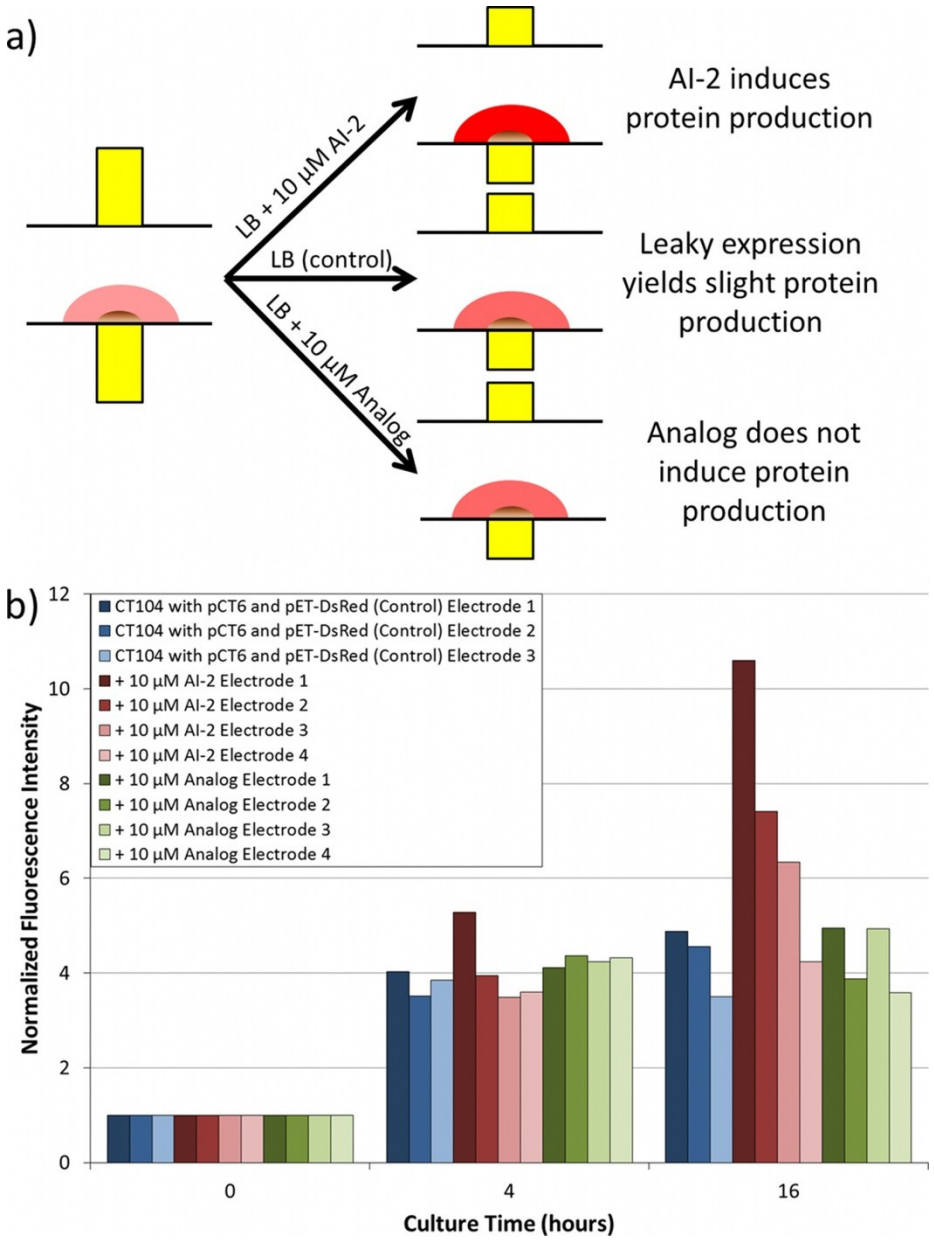

Figure 2-9. Application of bilayer clear gel technique to sensing intercellular signaling phenomena. a) Schematic overview of the experiment: *E. coli* strain CT104 containing the plasmids pCT6 and pET-DsRed are immobilized in the clear alginate gels. Two experimental conditions (LB media with 10 µM of AI-2 or nitrophenyl-DPD) and one control condition (LB media alone) are included. b) Normalized fluorescence intensity of the control and experimental conditions. Electrodes are in order (1-4) from upstream to downstream, separated by 3 mm of space between each electrode.

DPD (AI-2) will result in an increase in the production of T7 RNA polymerase, and subsequently the production of DsRed and increased red fluorescence.

Another effect worthy of note is observed in Figure 2-9b. There is a clear distance/positional dependence of the fluorescence in the device that received DPD, relative to the device that received the DPD analogue designed to inhibit quorum sensing. The first electrode, located closest to the fluidic inlet, receives the highest flux of both nutrients and AI-2 from the media. This effect decreases further down the channel due to the consumption of nutrients and uptake of AI-2 by cells in the hydrogels located closer to the fluidic inlet. This depletion effect is far less pronounced in the control case and in the device that received the quorum sensing-inhibiting DPD analogue. Indeed, over time it seems as though the cells from the first electrode in the device that received AI-2 migrated toward the fluidic inlet, as AI-2 is a known chemoattractant[37].

Future work

This technique has been developed using a relatively limited set of parameters. A more extensive characterization of the parameter space (including $CaCO_3$ mass fraction, alginate concentration, volumetric and linear flow rates of media, initial seeding density of cells, and many other factors) would provide a more complete picture of this technique and help other researchers adapt it to their individual experimental systems. The media composition is especially important, as the calcium-alginate hydrogels are prone to the accumulation of autofluorescent species from LB media, which renders blue and green fluorescence difficult, if not impossible, to use. This is potentially problematic, as blue

and green fluorescence are two of the three most prevalent fluorescence channels used in modern fluorescence microscopy.

Beyond the obvious parameter space characterization and reaction optimization, this technique can be applied to a number of possible areas. We have shown simple proof-of-principle experiments to demonstrate that these gels can be used to study intercellular signaling and create multilayered structures of different cell types. Extensions of these studies could include studying signaling in stratified biofilm mimics or migration of cells within the biofilm. One could even consider studying how the thickness of the hydrogel above a layer of cells (created by adding a layer of clear alginate) affects cell viability due to reduced diffusion or nutrient influx and waste efflux. Arrays of cell-based biosensors are another possibility.

Conclusions

We described a new technique to electrodeposit optically clear calcium alginate hydrogels to entrap, culture, and observe cells in microfluidic systems. This technique allows researchers to control where and when the cells are immobilized, as well as the geometry within which they are confined through consideration of electrode geometry and deposition time. Optical and confocal fluorescence microscopies demonstrate the gels are uniformly clear throughout their thickness, yielding unprecedented optical access throughout the entirety of the calcium alginate gel. This can lead to more accurate and quantitative studies of cell behavior in microfluidic systems. Cell growth and protein expression were observed over time, demonstrating that this technique is compatible with

cell culture and does not impede protein production within cells. Multilayer assembly between human epithelial cells and *E. coli* was demonstrated, serving as a proof of principle that this technique can enable the study of interactions between cell populations of different types. Additionally, applications in studying intercellular signaling and quorum sensing inhibition were demonstrated. Given the ubiquity of calcium alginate hydrogel entrapment in tissue engineering and cell culture research, we anticipate that this technique will enable a wide variety of new and useful experimental setups in microfluidics research[7, 24].

Acknowledgments

I gratefully acknowledge assistance from Yi Cheng, Chen-Yu Tsao, Hsuan-Chen Wu, Min Guo, Amin Zargar, Xiaolong Luo, Gregory F. Payne, Herman O. Sintim, William E. Bentley, and Gary W. Rubloff for this portion of my dissertation work. This work was supported by grants from the Robert W. Deutsch Foundation and the Department of Defense (DTRA #BO08SPO008). Device fabrication was performed using equipment in the Maryland Nanocenter and its FabLab for device fabrication. Confocal images were acquired in the Imaging Core Facility of the Department of Cell Biology and Molecular Genetics at the University of Maryland.

Chapter 3: Nonviral Nucleic Acid Delivery to Bacteria outside the Traditional Electroporation and Heat Shock Regimes

Note: This chapter will be adapted into a manuscript shortly after the dissertation defense, and should be published some time in 2014.

Chapter abstract

The ability to deliver nucleic acid sequences to cells is central to molecular biology and modern biotechnology. Nonviral nucleic acid delivery methods used in bacteria primarily include the use of a strong electric field (electroporation) or a heat shock to induce nucleic acid uptake. We describe a new form of nonviral nucleic acid delivery in bacteria which results from a synergistic effect between a much weaker DC electric field than experienced with electroporation and the use of calcium ions at a temperature much lower than experienced for heat shock. Typical transformation efficiencies using this technique are empirically lower than those of traditional electroporation. After transformation in a microfluidic environment, viable cells are cultured under conditions that allow expression of the newly delivered genes. Applications demonstrating intercellular communication and the formation of cell-based sensors of small molecules are demonstrated.

Introduction

Bacteria are capable of evolving to thrive in a wide range of environments. Short generation times enable relatively rapid adaptation to selective pressures imposed by the environment. However, the acquisition of a new metabolic function or pathway *de novo* is considerably less common than simple mutation of an extant gene or multiple genes within a pathway on the bacterial chromosome. Bacteria have evolved the ability to uptake and utilize extracellular DNA in the form of plasmids, small circular pieces of DNA that contain accessory genes to expand the functionality of the host cell, such as antibiotic resistance[38]. Bacterial have also evolved ways to transfer plasmids from one cell to another through a process called "conjugation"[39].

Viruses have evolved to infect specific bacteria, allowing another route for scientists to introduce nucleic acids into a bacterium. This process, termed "transduction", enables the introduction of a specific nucleic acid sequence (engineered into the viral genome) to a bacterium, followed by the propagation of this sequence to other neighboring bacteria following the viral life cycle. Transduction is somewhat limited in the size of nucleic acid that can be incorporated[40], as this is dictated by the geometry of the viral capsid; deviating greatly from the original viral genome size reduces the packing efficiency of the nucleic acid into the viral capsid, resulting in lower transduction rates[41, 42]. Additionally, the specificity of the virus/host system limits a broad applicability of the technique.

Nonviral nucleic acid delivery methods have become popular for their relative host independence and high efficiency. As with many research techniques, there are a

plethora of methods for introducing nucleic acid to cells without the use of viruses[40]. In bacteria, electroporation and chemical transformation are far and away the most popular[32, 43], but they are not the only methods in use[44, 45]. Some methods that are used industrially for nonviral nucleic acid delivery to eukaryotic cells include lipid complexes, polymers, and biolistic delivery (the "gene gun"), in which nucleic acids are adsorbed onto dense metal (W, Au, Ag) particles that are fired at target cells. Needless to say, delivery of specific nucleic acids to specific cell populations has been central to modern biotechnology and future gene therapy.

Given its prominence in the biotechnology field for delivering nucleic acids to both prokaryotic and eukaryotic cells, the physical underpinnings of electroporation have been relatively well studied[46, 47]. Movahed and Li have an excellent explanation of the electroporation mechanism, including the governing equations, limitations of current theory, and extensive references to primary literature[48]. When subjected to an electric field, charge builds up on the opposite sides of the membrane, with the hydrophobic core of the lipid bilayer acting as an insulator. This leads to a force compressing the membrane in the direction of the applied electric field. When the transmembrane potential exceeds a critical value (usually accepted to be on the order of hundreds of mV to 1V, representing a maximum field strength of 2,000 kV/cm for a "typical" lipid bilayer 5 nm thick), pores form in the membrane. Small, transient pores are believed to allow a discharging of the membrane, relieving the membrane compression and allowing the pores to reseal. Higher transmembrane potentials and longer exposure to the electric field can induce irreversible poration, which results in cell death. Electroporation has been miniaturized and integrated

into microfluidic systems, but mostly has been limited to eukaryotic cells and high electric field strengths (~600V/cm to 2 kV/cm; eukaryotic cells require lower fields than bacteria)[48-50]; few reports of bacterial transformation in microfluidics exist[51].

Chemical transformation, on the other hand, has a less well understood mechanism[32]. The general explanation is that Ca^{2+} ions in the solution (usually introduced by dissolution of $CaCl_2$) screen the negative charges found on the DNA backbone and the surface of many cells, allowing the DNA to diffuse into the cell when pores form in response to a heat shock. Hanahan and Bloom hypothesize a possible mechanism wherein Ca^{2+} interference in the formation of covalent bonds with lipopolysaccharide on the outer leaflet of the membrane leading to increased fluidity of the membrane[52]. They also attribute the DNA uptake to rapid changes in membrane fluidity due to rapid changes in temperature (the heat shock part of chemical transformation), but as with the lipopolysaccharide hypothesis, there is a lack of direct physical evidence. Despite lacking a known physical mechanism, chemical transformation via heat shock is readily adaptable to microfluidic systems, as has been demonstrated in the literature[53, 54].

We developed a new method for nonviral nucleic acid delivery to bacteria that occurs outside the parameter space of traditional electroporation and heat shock. Using a low voltage DC field, we are able to introduce plasmids to electrocompetent bacteria, enabling the alteration of the behavior of a population of cells. The transformation of the bacteria occurs at electric field strengths nearly two orders of magnitude below those typically used in electroporation of bacteria, and simulation results indicate that any heat

shock experienced by the cells is much more mild and brief than the conditions used for typical heat shock transformation. We then culture and monitor bacterial growth and protein production in a microfluidic device. Thus, to the best of our knowledge, this represents the first report of a mild, low-electric field strength transformation of a population of bacteria.

Experimental

Reagents, media, and consumables

LB media and ampicillin were purchased from Fisher Scientific. Sodium alginate, $CaCO_3$, isopropyl β-D-1-thiogalactopyranoside (IPTG) and kanamycin were purchased from Sigma Aldrich. Gene Pulser cuvettes with a 1 mm electrode gap were purchased from Bio-Rad.

Cells and plasmids

Escherichia coli strains BL21 (DE3), W3110 Δ*luxS* Δ*lsrFG* (referred to as CT104)[9], and W3110 Δ*luxS* (referred to as MDAI2)[55] were used from laboratory stocks. The plasmids used were pQE60-T5-DsRedExpress2[31], pET-DsRed, and pCT6[8]. Plasmids were isolated using QIAprep Spin Miniprep kits from Qiagen. CT104 was transformed with pCT6 and pET-DsRed using standard electroporation methods[32]. MDAI2 was transformed with pCT6 following the same electroporation protocol. Electrocompetent *E. coli* DH10B (ElectroMAX DH10B Cells) and chemically competent *E. coli* DH10B (MAX Efficiency DH10B Competent Cells) were purchased from Invitrogen.

Electrocompetent cell preparation

Electrocompetent cells were prepared from an overnight culture of *E. coli* (either BL21(DE3), CT104, or MDAI2) inoculated into LB media at 1% and grown at 37ºC with shaking at 250 rpm until an OD_{600} of 0.4 was reached. Cells were placed on ice for 30 minutes, transferred to chilled 50 mL conical centrifuge tubes, and pelleted at 8000×*g* for 20 min in a refrigerated centrifuge. The supernatant was decanted, and the cells resuspended in 25 mL of deionized water. The cells were centrifuged using the same parameters and resuspended in 15 mL of deionized water. The centrifugation and decanting were repeated, and the cells were resuspended in 5 mL deionized water. The cells were centrifuged a final time, the supernatant decanted, and the cells were resuspended in 1 mL of a 10% glycerol solution before being aliquoted into 50 µL aliquots in microcentrifuge tubes. The tubes were flash frozen in liquid nitrogen, and stored at -80ºC. Electrocompetence was confirmed using traditional electroporation methods described below.

Traditional electroporation

Traditional electroporation was achieved using a Bio-Rad Gene Pulser system with Bio-Rad Gene Pulser cuvettes. One aliquot of 50 µL electrocompetent cells was placed into a chilled cuvette, and 10 ng plasmid DNA was added to the cuvette. The voltage was set to 2.50 kV (field strength of 25 kV/cm for the 1 mm electrode gap), the capacitance to 2.5 µF, and the resistance set to 200 Ω. Immediately after electroporation, 1 mL LB media

was added to the cuvette, and it was placed in a 37ºC incubator for one hour before plating on LB-agar plates supplemented with appropriate antibiotics.

Traditional heat shock

Heat shock was achieved by incubating an aliquot of chemically competent cells with 10 ng plasmid DNA in a culture tube on ice for 30 minutes. The tube containing the mixture was immersed in a 42 ºC water bath for 90 seconds. Immediately after heat shock, 1 mL LB media was added to the tube, and it was placed in a 37 ºC incubator for one hour before plating on LB-agar plates supplemented with appropriate antibiotics.

Electro-assisted nucleic acid delivery and cell immobilization in microfluidics

Electro-assisted transformation with simultaneous alginate immobilization was performed in a microfluidic device whose fabrication is described in Chapter 2. Briefly, on ice, 10 µL of electrocompetent cells was mixed with 10 µL of 40 ng/µL plasmid DNA and 20 µL of a mixture of 1% (w/v) sodium alginate, 0.5% (w/v) $CaCO_3$ that had been boiled and cooled. The mixture was loaded into the microfluidic device (also on ice) via 1 mL syringe, and electrode leads were connected to a Keithley 2400 SourceMeter. A 3V potential was applied between each pair of electrodes for 3 minutes. Fresh LB media supplemented with 10 mM $CaCl_2$ was added to the device, and the device was placed in a humidified 37 ºC incubator for 1 hour prior to imaging and culture.

Culture conditions

Cells in the microfluidic devices were cultured in a humidified 37 ºC incubator for the duration of their culture, with brief excursions to room temperature in order to image the cells. While in the incubator, LB media supplemented with 10 mM $CaCl_2$ and appropriate antibiotics (50 μg/mL Ampicillin for pQE60-T5-DsRedExpress2 or pCT6, 50 μg/mL Kanamycin for pET-DsRed) was pumped at a constant volumetric flow rate of 15 μL/min using a syringe pump. For *E. coli* BL21(DE3) transformed with pET-DsRed, DsRed protein production was induced by using LB media supplemented with 10 mM $CaCl_2$, 50 μg/mL Kanamycin, and 1 mM IPTG at the indicated time. The media for CT104 with pCT6 and pET-DsRed or MDAI2 with pCT6 was supplemented with 10 μM chemically synthesized DPD[33-35]. The devices were removed from the incubator and the media flow was stopped only for the time necessary to image the cells.

Optical microscopy, image processing, and analysis

Bright field optical and fluorescence micrographs were acquired using a Zeiss LSM310 fluorescence microscope with a 5× air objective lens. The objective lens was located directly above the device and was focused on the anode surface in the channel. The optical micrographs were obtained with transmitted light coming from the bottom through the transparent PDMS layers. For fluorescence imaging, the FITC filter set (Chroma) was used for the fluorescein-labeled microspheres and the TRITC filter set (Chroma) was used for the *E. coli* expressing DsRed. ImageJ[36] image analysis software was to analyze both the bright field and fluorescence images. The fluorescent

background was subtracted from images by taking an average grayscale intensity value of an area free of transformed cells (defined as a region of interest in a stack including optical and fluorescent images), and then subtracting that value from the entire image. Average grayscale values for the fluorescence were calculated by converting the color .jpg image to an 8-bit grayscale and defining a region of interest around the alginate hydrogel in the optical micrograph in an image stack containing both the optical and fluorescent image. The region of interest is then measured for the fluorescent image, and the average value is recorded.

Simulation of deposition conditions

COMSOL Multiphyiscs v. 4.1 was used to simulate the electric field and resulting Joule heating of the solution inside the microfluidic device during the electrodeposition and transformation. The conductivity of the solution was estimated from literature values[56], based on an upper-bound estimate for the amount of Ca^{2+} generated during the electrodeposition. During electrodeposition, the average current density is approximately 10 A/m^2. Assuming every electron entering the anode comes from the electrolysis of water according to Equation 3-1, and every proton generated from the electrolysis of water is used to dissolve CaCO3 according to Equation 3-2, the maximum amount of Ca^{2+} generated corresponds to a concentration of approximately 40 mM.

$$2\,H_2O \rightarrow O_2 + 4\,H^+ + 4\,e^- \qquad \text{(Equation 3-1)}$$

$$CaCO_3 + 2\,H^+ \rightarrow Ca^{2+} + H_2O + CO_2 \qquad \text{(Equation 3-2)}$$

Results and discussion

Figure 3-1 shows a schematic overview of the process and a representative fluorescent micrograph of the resulting transformed bacteria cultured in the calcium alginate hydrogel. Electrocompetent bacteria are mixed with plasmid, alginate, and calcium carbonate before being placed into a microfluidic device. An electric field is passed between two vertical sidewall electrodes at a constant electric field of 3V, resulting in an average current density of approximately 10 A/m^2 over the course of the 3 minute electrodeposition. During the electrodeposition, Ca^{2+} ions are liberated from the dissolution of $CaCO_3$, causing the alginate to form a hydrogel, entrapping the bacteria within the hydrogel. During this process, some bacteria take up the extracellular plasmid, becoming transformed in the process. The bacteria are then cultured by flowing media that also contains an antibiotic that selects for the plasmid, resulting in those bacteria that were transformed by the plasmid being able to grow and reproduce. Additional chemical signals can be added to the media, inducing the bacteria to produce a fluorescent response to those extracellular signals.

Cell-based sensors of small molecules present in the media

Transformation can be used to make cell-based sensors, and the *in situ* programming of an array of cell-based sensors would open up the possibility of the dynamic creation of a custom cell- based sensor platform for a given compound or suite of analytes. Figure 3-2 shows an example of this. *E. coli* BL21(DE3) was transformed with pET-DsRed.

Figure 3-1. Schematic overview of the electro-assisted transformation of electrocompetent bacteria in a microfluidic device. a) Electrocompetent bacteria, plasmid, sodium alginate, and $CaCO_3$ are mixed together and placed in the microfluidic device. b) An electric field induces the electrolysis of water, dissolution of $CaCO_3$, and the release of Ca^{2+}; some combination of these factors leads electrocompetent bacteria to uptake plasmid. c) Remaining cells, plasmid, alginate, and $CaCO_3$ are flowed out of the device, and the bacteria are entrapped in the calcium alginate hydrogel at the electrode surface. d) Culture medium with appropriate antibiotics to select for transformed bacteria is flowed through the device, allowing transformed bacteria to survive and multiply. e) Transformed bacteria are able to grow and respond to small molecule cues in their extracellular environment. f) Fluorescent micrograph of *E. coli* BL21(DE3) transformed with pET-DsRed producing DsRed in response to extracellular IPTG.

a) Bacteria, plasmid in device

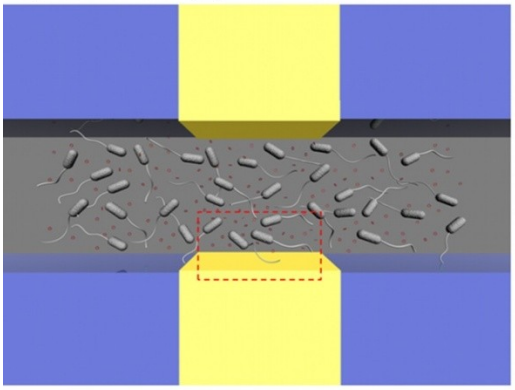

b) Plasmid uptake by bacteria

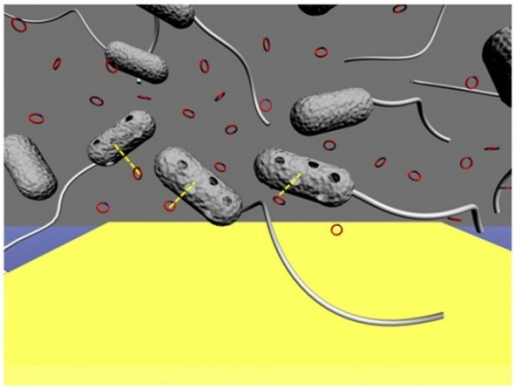

c) Transformed bacteria in gel

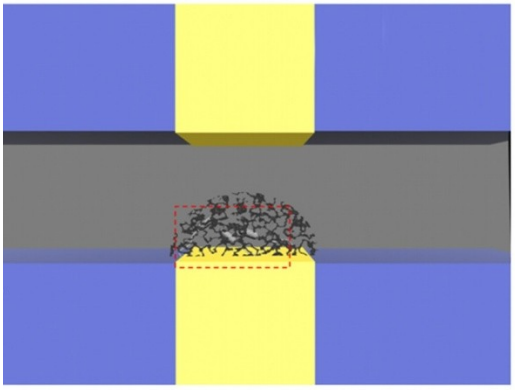

d) Bacteria cultured over time

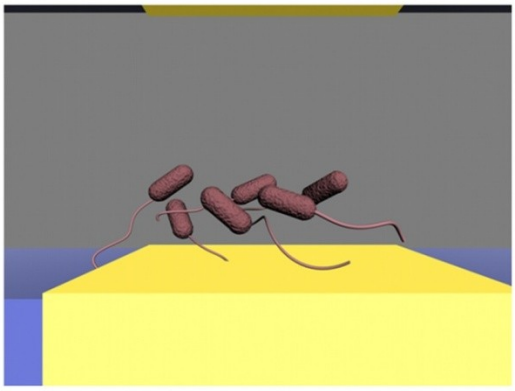

e) Cell growth, protein production

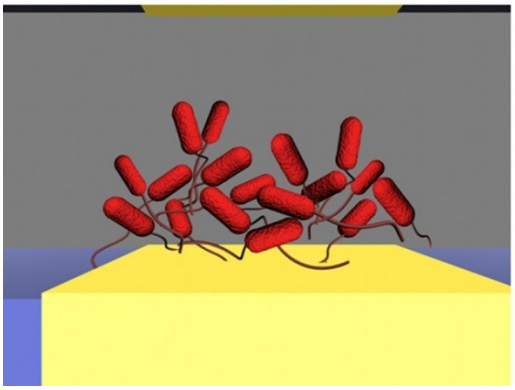

f) Fluorescent micrograph

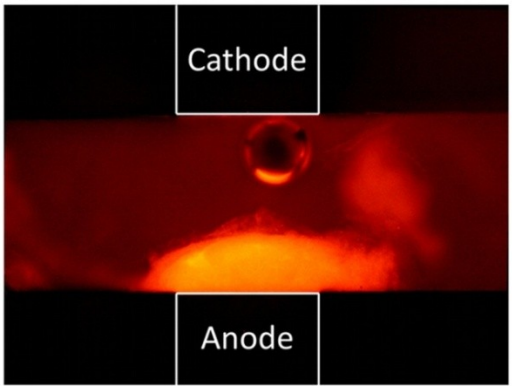

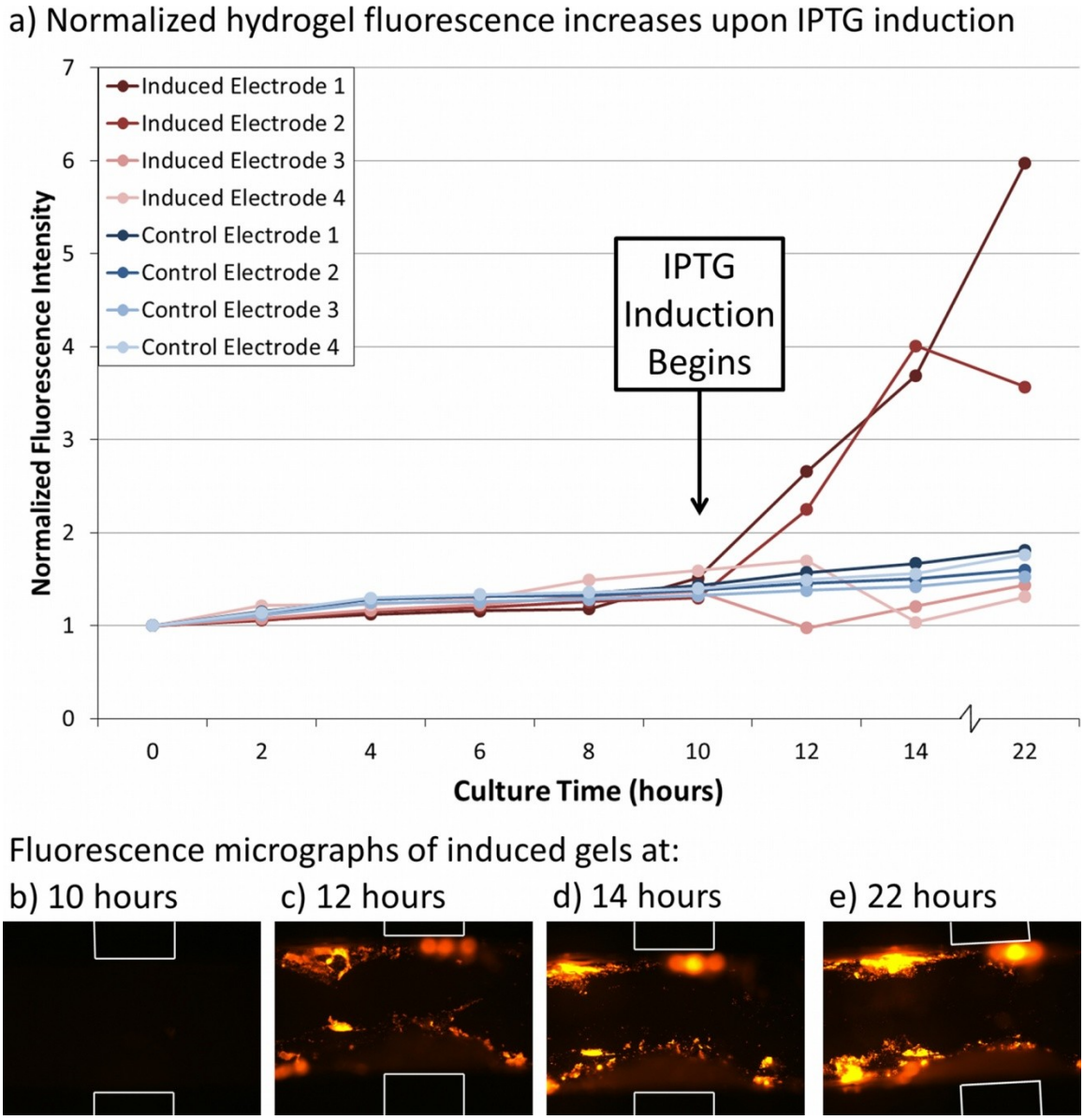

Figure 3-2. Transformation of *E. coli* BL21(DE3) with pET-DsRed in a microfluidic device. a) Average hydrogel fluorescence as a function of culture time. Both the control and induced populations have been transformed using the method described in this chapter. The media for the induced population was changed at the 10 hour mark to include 1 mM IPTG. b-e) Representative fluorescent micrographs of the induced population of cells at the indicated times. The electrodes are outlined in white and are 1 mm wide, separated by 3 mm. Electrodes (1-4) are in order from upstream to downstream.

BL21(DE3) naturally expresses a low level of the T7 RNA polymerase, leading to a low level of expression of DsRed when transformed with pET-DsRed. This phenomenon has been called "leaky expression", as the *lac* repressor does not completely prevent transcription of genes downstream of the repressor binding site. However, when exposed to lactose or derivatives thereof, the *lac* repressor changes conformation and allows transcription of downstream genes- in this case, the production of DsRed. After 10 hours of culturing, IPTG is added to the media to induce DsRed production. There is a distinct increase in the fluorescence of the first two hydrogels in the device that received IPTG relative to those that did not (the control group). However, as discussed in Chapter 2, there is a clear depletion effect that occurs down the length of the channel, with the cells in the first two hydrogels receiving and consuming the largest amount of IPTG. In the device that received IPTG, the cells in the third and fourth hydrogels did not receive enough IPTG to induce additional protein expression, resulting in fluorescence levels similar to those of the control gels.

Programming bacteria with a new response to exogenous signaling molecules

The ability to introduce plasmids to a bacterium opens up many possibilities in terms of both *what* the bacteria can be used to sense and *how* they respond to a stimulus. As a proof of concept, in Figure 3-3, we introduce pET-DsRed into a bacterium that is unable to produce endogenous autoinducer 2 (AI-2), but is still able to sense the molecule and respond according to its genetic programming. In this case, pET-DsRed is used as a

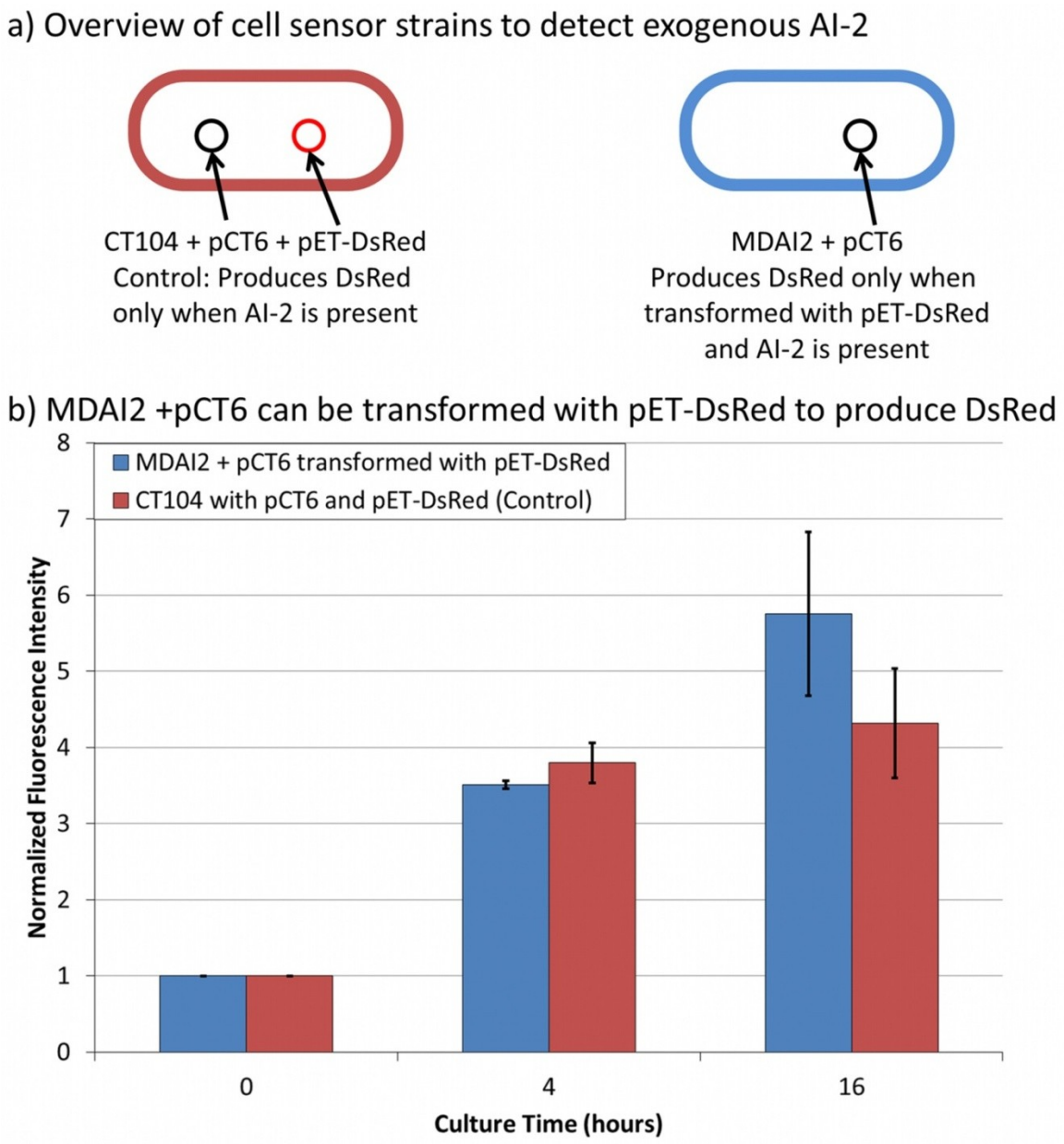

Figure 3-3. Programming a new response to exogenous signaling molecules. a) Schematic overview of the two strains of bacteria involved in this experiment. b) Normalized fluorescence as a function of culture time in the presence of 10 μM AI-2.

model plasmid, but in actuality, any plasmid containing a T7 RNA polymerase promoter site can be used to transcribe a desired set of genes. This is compared with a related bacterium that produces DsRed upon exposure to AI-2 in an effectively constitutive manner. As can be seen from the results, expression of DsRed upon exposure of the cells to 10 μM AI-2 results in similar increases in fluorescence, normalized to the initial fluorescence of the hydrogels in each device. This indicates that a desired genetic program can be introduced to a population of electrocompetent cells electrodeposited within a calcium alginate hydrogel, effectively allowing researchers to program customized genetic responses to extracellular signaling molecules.

Electro-assisted transformation mechanistic insights

Of the possible nonviral nucleic acid delivery methods that could lead to transformation under these conditions[44], electroporation and chemical transformation are the most probable mechanisms. To investigate the possible contribution of electric field (essential for electroporation) and heat shock (essential for chemical transformation), COMSOL Multiphysics software was used to conduct a finite element analysis of both the electric field in the device, and any resultant Joule heating of the solution. Figure 3-4 shows the results of the simulations. In Figure 3-4a, the electric field in the main channel does not exceed approximately 60 V/cm, which is still far below the 25,000 V/cm field strength normally used in traditional electroporation[32, 43]. This reduces the likelihood that the mechanism is a traditional electroporation.

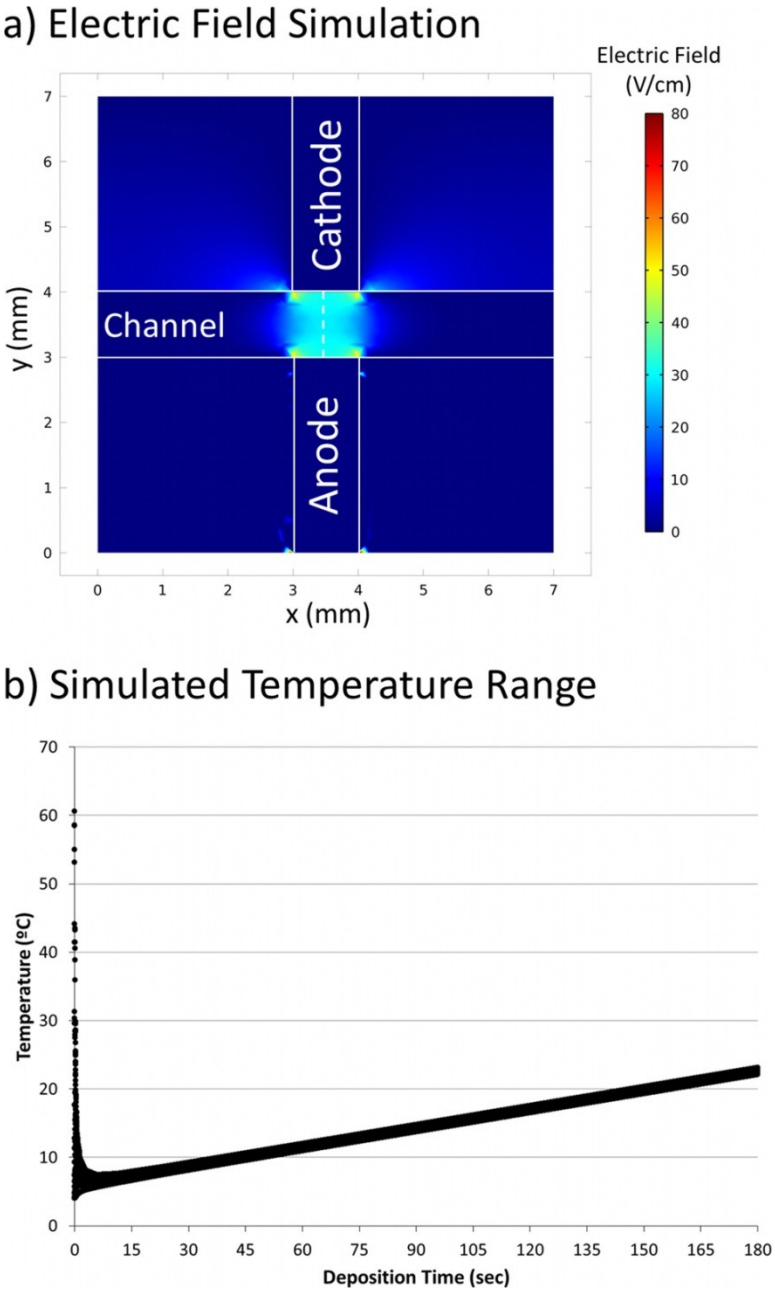

Figure 3-4. COMSOL Multiphysics simulation of conditions during electro-assisted transformation in the microfluidic device on ice. a) Electric field simulation for a constant potential of 3V. The maximum electric field strength in the channel does not exceed 60 V/cm, even at the edges of electrodes. b) Simulation of joule heating along the white dashed line indicated in a). A brief initial heat shock lasts for a few seconds, followed by linear temperature increase.

Heat shock mediated chemical transformation is a less likely candidate mechanism, as chemically competent and electrocompetent cells are prepared differently[32]. The generation of divalent cations (Ca^{2+}) and the Joule heating effect during electrodeposition made it a possibility worth investigating. As seen in Figure 3-4b, there is a brief spike in temperatures initially, followed by a rapid convergence and gradual warming of the solution. However, this is far from the 0ºC to 42ºC heat shock for 90 seconds that is typically used for chemical transformations.

To confirm that the electrocompetent BL21(DE3) were unable to be transformed by a standard chemical transformation protocol, the cells were subjected to the traditional heat shock protocol outlined earlier in this chapter. No transformants were obtained. The protocol was demonstrated to work with Invitrogen's MAX Efficiency DH10B chemically competent cells. Additionally, the MAX Efficiency DH10B cells were unable to be transformed using the electro-assisted transformation method described in this chapter. Furthermore, mid-log *E. coli* that were not prepared to be electrocompetent were unable to be transformed using the new method described in this chapter. These results point toward an electroporation mechanism that occurs outside the parameter space of traditional electroporation.

An interesting aspect to note is that a naïve calculation of the total charge transferred in the case of traditional electroporation (using the traditional electroporation parameters and Ohm's Law, multiplying by the 5 ms pulse duration) is 0.0625 C, and the amount of charge transferred during the electro-assisted transformation described in this chapter is approximately 0.0018 C (approximating the average current as 10 μA and the

time of 180 s), a 35 fold difference. In the electro-assisted transformation, higher voltages (or currents) result in the formation of gas bubbles, which destabilize the hydrogel, causing it to detach from the electrode in some cases. Perhaps running a longer deposition may result in more efficient transformation.

Additional experimental evidence indicates that some form of electroporation is responsible for the electro-assisted transformation in the microfluidic devices. When distilled water (rather than deionized water) was used to prepare electrocompetent cells, the average current densities were noticeably higher than normal, and no transformation was observed. Furthermore, while attempting to transform these cells using traditional electroporation methods, electricity arced across the solution. This indicates that residual ions in the distilled water provided an alternative pathway for the electricity, avoiding the membrane-destabilizing effects typically experienced with lower conductivity solutions[43]. While indirect, these additional results support an electroporation mechanism for the transformation described in this chapter.

Future work

There are two main thrusts of future work for this new transformation method. The first, a basic science approach, involves determining the mechanism of transformation and optimizing transformation conditions. We have not been able to conclusively determine the mechanism to be a low-level electroporation, and calcium ion flux could play a more important role. Determining the effect of the temperature on transformation efficiency would be important for determining the mechanism and optimization. Production of

fluorescent proteins under the control of a heat sensitive promoter and recent advances in "molecular thermometers" would be beneficial for addressing this. Developing a way to quantitatively assess the transformation efficiency is something that has been elusive thus far. The effective volume of cells exposed to the transformation conditions is approximately 1 μL, and removing the cells entrapped in the hydrogel is difficult to do without knowing what effect this has on transformation efficiency and cell viability. Optimizing the deposition conditions, such as field strength/current density, plasmid concentration, cell density, alginate concentration, and $CaCO_3$ mass fraction, would be extremely beneficial. We performed some preliminary experiments and found a set of conditions that generally worked well, but a more thorough exploration of the parameter space would provide both mechanistic insight and improved transformation efficiency. Additionally, the fringing effect of electric fields at the edge of an electrode can provide very high localized electric fields. It could be that bacteria closest to the electrode edges are preferentially transformed by the higher local electric field strength. This could be investigated by a reconfiguration of the electrode geometry, creating narrower or wider electrodes to observe how this changes protein production and cell growth. Finally, scanning probe microscopy may provide a quantitative measure of the effects of field strength on electroporation of bacteria.

The second main thrust is a practical one- using this method to do new science or perform old experiments with a new twist. We performed this method with *Trichoplusia ni* High Five cells from Invitrogen with success once, but were unable to reproduce the results when we tried a second time. HeLa cells from ATCC were unable to be

transfected unless the vector was mixed with a transfection reagent prior to the electrodeposition. Perhaps some set of parameters may make the one-step entrapment and reprogramming of eukaryotic cells a viable process. Demonstrating RNA interference with eukaryotic cells via this nucleic acid delivery technique would be an exciting advance. Additionally, studying intercellular communication with dynamically assembled and *in situ* programmed bacterial populations would enable combinatorial construction of bacterial consortia for a desired purpose. Finally, the *in situ* programming of an array of bacterial sensors would create a flexible cell-based biosensing platform that can be programmed on demand for a specific analyte or suite of analytes.

Conclusions

We demonstrated a new nonviral nucleic acid delivery method that occurs outside the traditional parameter spaces of electroporation and heat shock. *E. coli* were transformed with plasmids that enabled them to sense small molecules, such as the chemical inducer IPTG and the bacterial signal AI-2, in their environment and respond according to a predetermined genetic plan- in this case, the production of the DsRed fluorescent protein. COMSOL multiphysics simulations provided insight into the conditions experienced by the bacteria, indicating that the electric field is two to three orders of magnitude below that of traditional electroporation, and any heat shock experienced due to Joule heating is too weak and too brief to induce plasmid uptake. Additional experimental results pointed indirectly toward the occurrence of electroporation outside the traditional electroporation regime. More work is needed to identify the exact mechanism and optimize the

conditions, as well as expand applications into cell signaling, biosensing, and nucleic acid delivery to eukaryotic cells.

Acknowledgments

I gratefully acknowledge assistance from Yi Cheng, Chen-Yu Tsao, Hsuan-Chen Wu, Min Guo, Jessica Terrell, Xiaolong Luo, Gregory F. Payne, Herman O. Sintim, William E. Bentley, and Gary W. Rubloff for this portion of my dissertation work. This work was supported by grants from the Robert W. Deutsch Foundation and the Department of Defense (DTRA #BO08SPO008). Device fabrication was performed using equipment in the Maryland Nanocenter and its FabLab for device fabrication.

Chapter 4: Galvanic Displacement for Fabrication of Surface Enhanced Raman Scattering (SERS) Substrates

Note: Portions of this chapter were adapted or reproduced with permission from Betz, J. F. et al., *Direct SERS detection of contaminants in a complex mixture: Rapid, single step screening for melamine in liquid infant formula*, Analyst, 2012. **137**: 826-828[57] and Betz, J. F., et al., *Simple SERS substrates: Powerful, portable, and full of potential*, Physical Chemistry Chemical Physics, 2013. In Revision.[58]

Chapter abstract

Surface enhanced Raman spectroscopy (SERS) substrates were created on several common metal objects, including coins and metalized tape, by a galvanic displacement method, creating simple and effective portable SERS substrates. The reaction involves the displacement of nickel and copper from the surface of a dime and penny, respectively, by a mixture of $AgNO_3$ and NH_4OH. This method forms silver structures on the coin surface in less than 30 minutes in a one-step, room-temperature process without the use of hazardous chemicals, making it more user-friendly and amenable to portable SERS sensing applications than many other methods. The resulting SERS substrates exhibit an enhancement factor on the order of 10^9 for Rhodamine-6G under non-resonant conditions for the Raman excitation of R6G itself. Despite the random nature of the substrates, signals obtained were reproducible to within an order of magnitude or better. To further demonstrate the power and versatility of these substrates, melamine was spiked into infant formula, and was detectable down to 5 parts per million, which is above the current

1 ppm limit allowed in infant formula by the US Food and Drug Administration as well as the World Health Organization. This method opens the door to further development of rapid, simple, inexpensive, and portable SERS applications in areas such as rapid chemical detection, quality control, and remote healthcare.

Introduction

Surface enhanced Raman spectroscopy (SERS) is a highly sensitive, non-destructive spectroscopic technique that allows for the detection of molecules at concentrations down to the single molecule level[59-62]. The SERS phenomenon has enabled the development of applications in biosensing[63-65], trace analysis[66-68], bacterial typing[69, 70], *in vivo* imaging[71, 72], and many other areas. The enhancement of the Raman signal is believed to be a combination of: (1) an electronic effect, often called chemical or charge transfer, between the analyte and metal surface[73], resulting in approximately two to three orders of magnitude enhancement; and (2) an electromagnetic excitement of surface plasmons due to light interacting with the metal surface[74], which can result in up to 13 orders of magnitude enhancement. While the charge transfer component of the SERS enhancement is determined by metal-analyte interactions, the electromagnetic component is dictated largely by the nanoscale structure of the SERS substrate[75]. Many studies have described methods for producing SERS substrates with different geometries[76]- primarily nanoparticles[77, 78], nanoparticle and nanowire arrays[79-81], and roughened metal electrodes[82, 83].

Recent work has employed the well-studied galvanic displacement as a simple method to form SERS substrates with excellent enhancement characteristics[84-89]. Galvanic displacement is a spontaneous electrochemical reaction, driven by the free energy change resulting from the difference in the reduction potentials of the reacting species. The process is shown schematically in Figure 4-1. In this type of reaction, a solid metal or semiconductor atom is oxidized and displaced from a surface by a metal ion, which itself is reduced to a solid, resulting in diffusion limited growth[90] of highly pure metallic structures[91]. Due to their desirable plasmonic properties[92], Au and Ag are often used in forming SERS substrates. Given that these two metals are strong oxidizers in their cationic states, able to displace many other metals and semiconductors, this method lends itself quite readily to forming micro- and nanoscale metal geometries with a high surface area and many SERS hot spots[86]. However, in order to form these SERS substrates, prior work has used hydrofluoric acid (HF) or other strong acids to remove the surface oxide layer present on semiconductors[85-87] and metals[88, 89, 93]. Methods to create SERS substrates by galvanic displacement that do not rely on HF or other potentially dangerous or harmful reagents would be advantageous in terms of the safety and portability of the method and subsequent substrates.

This chapter presents a rapid, simple method to form powerful micro- and nanostructured SERS substrates using the galvanic displacement method without the use of HF, i.e. without the need for a separate oxide-removal step. This single step, room temperature method takes less than an hour from cleaning the metal substrates to beginning the spectroscopic measurements. The commercial availability of handheld

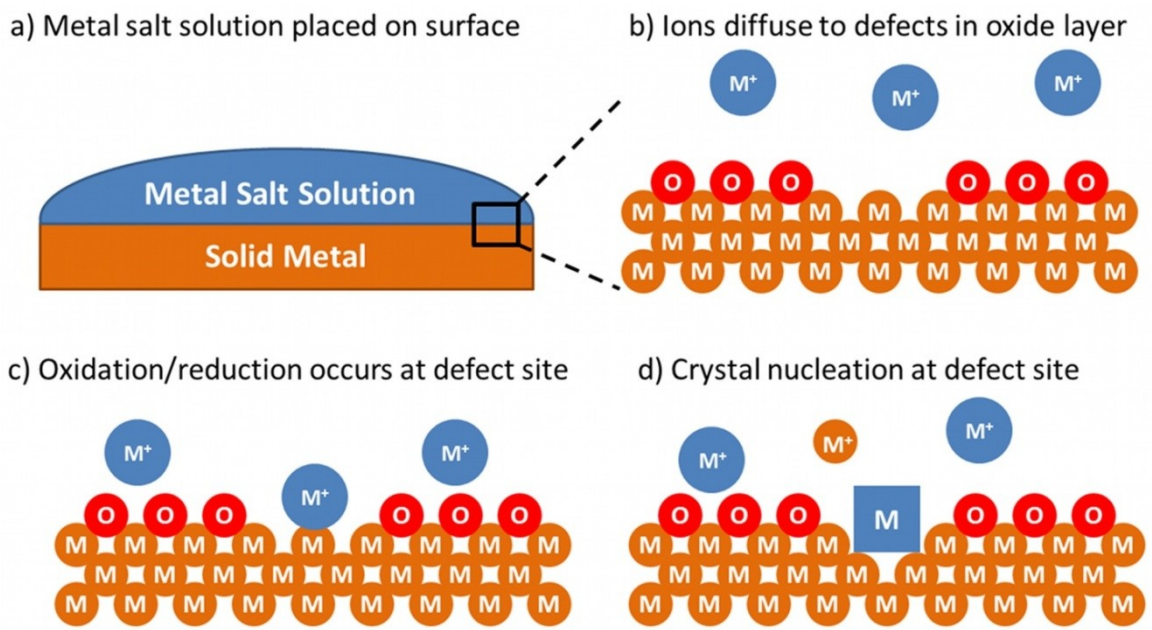

Figure 4-1. Schematic overview of the galvanic displacement mechanism. a) A metal salt solution is placed onto a solid metal or semiconductor surface, where the reaction takes place. b) At the interface highlighted in the box in part a, metal ions (blue circles) diffuse to defects in the metal oxide layer (red circles). c) The metal ion is reduced to a zero valent state by an oxidation-reduction reaction directly with the bulk metal (brown circles), presumably through a hydride transfer[94]. d) The zero valent metal acts as a nucleation point for crystal growth at the defect site through additional rounds of oxidation-reduction of other metal ions from solution.

Raman spectrometers at modest cost opens the door to remote and field applications of SERS, such as detection of environmental contaminants at improved limits of detection and medical diagnostic applications such as bacterial typing or viral identification in locations where access to a pathology lab may be limited.

To underscore the portability of this method, the galvanic displacement was done on highly portable, common metal objects- coins. The process is shown schematically in Figure 4-2. Using $AgNO_3$ and dilute NH_4OH, which could be easily and safely transported to and used in a remote location, Ni and Cu were displaced from the surface of dimes and pennies, respectively, forming Ag structures consistent with those previously described in the literature on galvanic displacement. These SERS substrates were then characterized using Rhodamine-6G (R6G), a common analyte for evaluating SERS substrates. The substrates exhibited an enhancement factor (due specifically to the SERS nanostructures) for R6G on the order of 10^9, without any resonant enhancement by excitation wavelengths for R6G. An important and practical application in point-of-sampling remote analysis was demonstrated using melamine with substrates formed on a penny and copper tape. Melamine is a toxic chemical that has been illegally used to increase the apparent protein content of pet food, infant formula, and milk, as measured by conventional food safety methods. Here, melamine was mixed with infant formula and detected at a level of 5 parts per million (ppm), which is above the current maximum allowable limit under United States Food and Drug Administration and World Health Organization regulations, both of which set the limit at 1 ppm. Thus these SERS

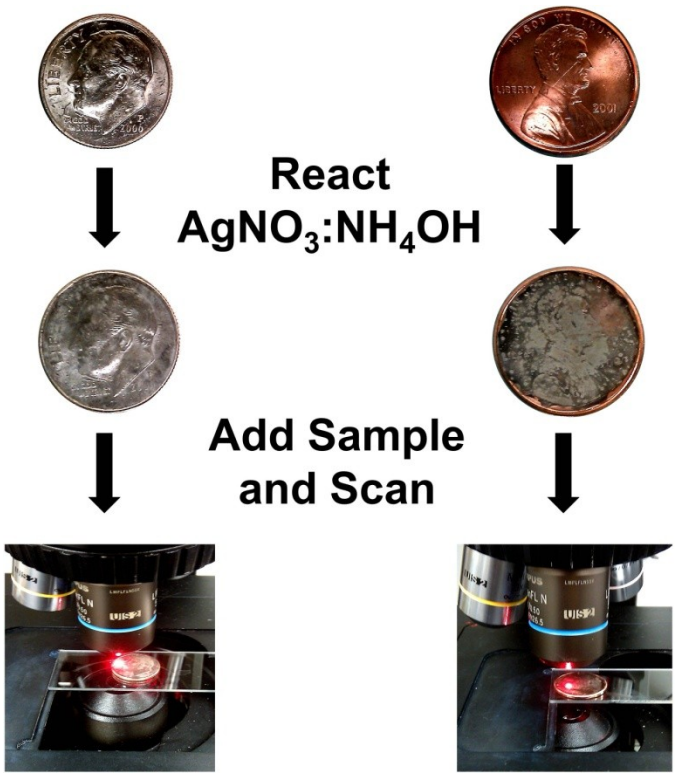

Figure 4-2. Schematic representation of the experimental process used to fabricate SERS substrates on a dime and penny. First, a solution of $AgNO_3$ and NH_4OH is dripped on the surface and allowed to react for 30 minutes before being rinsed with distilled water and dried under flowing air. The sample is placed on the substrate and allowed to dry (approximately 10 minutes) and analyzed using a Raman spectrometer.

substrates are a promising path to simple, effective, reliable, and highly portable SERS substrates and subsequent applications, including screening for food safety.

Experimental

SERS substrate formation on coins

$AgNO_3$ (ACS grade) was obtained from Alfa Aesar. Rhodamine-6G (99%) was obtained from Sigma Aldrich. NH_4OH (ACS Plus grade) was obtained from Thermo Fisher Scientific. Coins were ultrasonicated for 15 minutes in deionized H_2O, rinsed with 70% isopropanol, rinsed with deionized water, and dried under flowing air. A solution of 50 mM $AgNO_3$ was created using deionized water and combined with concentrated NH_4OH in a ratio of 10^6 $AgNO_3$: 1 NH_4OH by serial dilution. 450 µL of deionized water was placed on each coin to wet the entire surface, and 50 µL of the $AgNO_3$:NH_4OH solution was mixed with the water and allowed to react for 30 minutes in the dark before being rinsed gently with 500 µL of deionized water. The substrates were then dried gently under flowing air.

SERS substrate formation on copper tape

Copper foil tape (3M) was applied to a cleaned glass slide and cleaned using deionized water and 70% isopropanol. 10 µL of 50 mM $AgNO_3$ was spotted onto the tape surface and allowed to react for 30 minutes in the dark before being gently rinsed with 100 µL of deionized water and dried with flowing air.

SERS substrate formation on thin metal films

Standard glass slides were cleaned using piranha solution (3:1 H_2SO_4:H_2O_2). 100 nm of Cu or Ni was coated onto the cleaned glass slide using a Denton electron beam evaporator (Denton Vacuum, LLC). The slides were then patterned using standard photolithography techniques, exposing circles of metal 8 mm in diameter using SU-8 photoresist (Microchem). 80 μL of deionized water was placed on each metal circle to be reacted, and 20 μL of the $AgNO_3$:NH_4OH solution was mixed with the water and allowed to react for 30 minutes in the dark before being rinsed with 100 μL of deionized water. The substrates were then dried under flowing air.

Scanning electron microscopy characterization

Scanning electron micrographs of the substrates were obtained using a Hitachi SU-70 scanning electron microscope at an accelerating voltage of 10 keV. A Bruker silicon drift detector was used to determine elemental composition of the substrates by energy dispersive spectroscopy (EDS).

SERS characterization

To investigate the SERS activity of the substrates, 20 μL of a 1 μM solution of Rhodamine-6G (R6G) in methanol was placed on a dime and penny substrate and allowed to dry, requiring less than 10 minutes. To determine the reproducibility of the signals from different substrates on the same type of coin, 20 μL of 1 μM R6G was placed on each of five substrates of each coin type. Raman spectra were obtained at 50x magnification using a Horiba Jobin-Yvon LabRamHR-800 system using the internal

HeNe laser with a wavelength of 632.8 nm. Twenty spectra were obtained at each concentration at different points selected on the substrate, and the average of all 20 spectra was used. Spectra were acquired over the spectral range from 600 cm^{-1} to 1700 cm^{-1} for two seconds, repeated 15 times and averaged. LabSpec software (v. 5.25.15, Horiba) was used to control the instrument, acquire spectra, perform background subtraction, and analyze the spectra. Additional analysis of SERS spectra was performed using the ChemoSpec chemometrics package version 1.61-3[95], in the R statistical programming environment, version 3.0.1[96].

Detection of melamine in infant formula

Commercial infant formula (Enfamil, Mead Johnson & Company) was prepared according to manufacturer's instructions. Melamine (99%) was obtained from Sigma-Aldrich. Solutions of infant formula were either used as prepared or spiked with melamine at 1000 ppm, 100 ppm, 10 ppm, 5 ppm, 1 ppm, and 0 ppm (pure formula as a control). 2 μL of each solution was placed on penny and copper tape substrates, prepared as described above. Raman spectra were obtained over the same spectral range as above using a 785 nm diode laser, which was used to evaluate the possibility of using these substrates for portable, point-of-sampling analysis. Ten points on the substrate were scanned with a total signal acquisition time of 150 seconds (3 second acquisitions averaged 5 times per spot over 10 spots) for the 1000 ppm, 100 ppm, and 10 ppm levels and 500 seconds (10 second acquisitions averaged 5 times per spot over 10 spots) for the 5 ppm, 1 ppm, and 0 ppm (normal infant formula) levels.

Results and Discussion

Galvanic displacement was used to fabricate SERS substrates on the surface of dimes and pennies rapidly, easily, and inexpensively as previously shown schematically in Figure 4-2. A solution of $AgNO_3$ and NH_4OH spontaneously displaced Ni and Cu from the dime and penny, respectively, forming the Ag SERS substrates in a simple, one-step, room temperature process. The electrochemical reactions that occur are given in Equations 4-1 and 4-2.

$$2Ag^{+} + Cu \rightarrow Cu^{2+} + 2Ag \qquad E^{o} = 0.46V \qquad \text{(Equation 4-1)}$$

$$2Ag^{+} + Ni \rightarrow Ni^{2+} + 2Ag \qquad E^{o} = 1.08V \qquad \text{(Equation 4-2)}$$

Unlike many other galvanic displacement methods[85-87, 89, 93], this process did not require the use of HF or other caustic reagents to strip the native oxide present on the surface of the coins, either prior to or during the galvanic displacement process. Presumably, the nucleation and crystal growth occurred and defect sites in the native oxide layer, perhaps at metal grain boundaries, eliminating the need for HF. Nor did the process require overnight reaction, as is required with many semiconductor[86, 87] and metal[89] galvanic displacement processes.

SERS Substrate Characterization

The Ag features formed on the dime are highly heterogeneous. The scanning electron micrographs in Figure 4-3a-b show highly variable features spanning several orders of magnitude in size both at the 1,000× (Figure 4-3a) and 10,000× (Figure 4-3b) magnification levels. Much of the surface is covered by broad, thin Ag polyhedral

Figure 4-3. SEM and EDS characterization of the dime (a, b, c) and penny (d, e, f) SERS substrates. The scanning electron micrographs taken at 1,000× magnification show a drastic difference in the substrate morphology between the dime (a) and the penny (d), especially the pronounced linear arrangement of features as indicated by the white arrow. A 10,000× magnification view of the areas indicated in (a) and (d) further highlights the difference in morphology and coverage, with the dime (b) consisting of larger particles that tend to terminate in small, sharp edges and the penny (e) consisting of small particles composed almost exclusively of small, sharp edges. Elemental analysis by EDS of the areas indicated by crosses in b and e shows a significant amount of silver present in the particles both on the dime and penny (black traces, (c) and (f), respectively), while the surface of the coins (red traces, (c) and (f)) show an elemental composition consistent with the composition of the respective coins with only trace amounts of silver present.

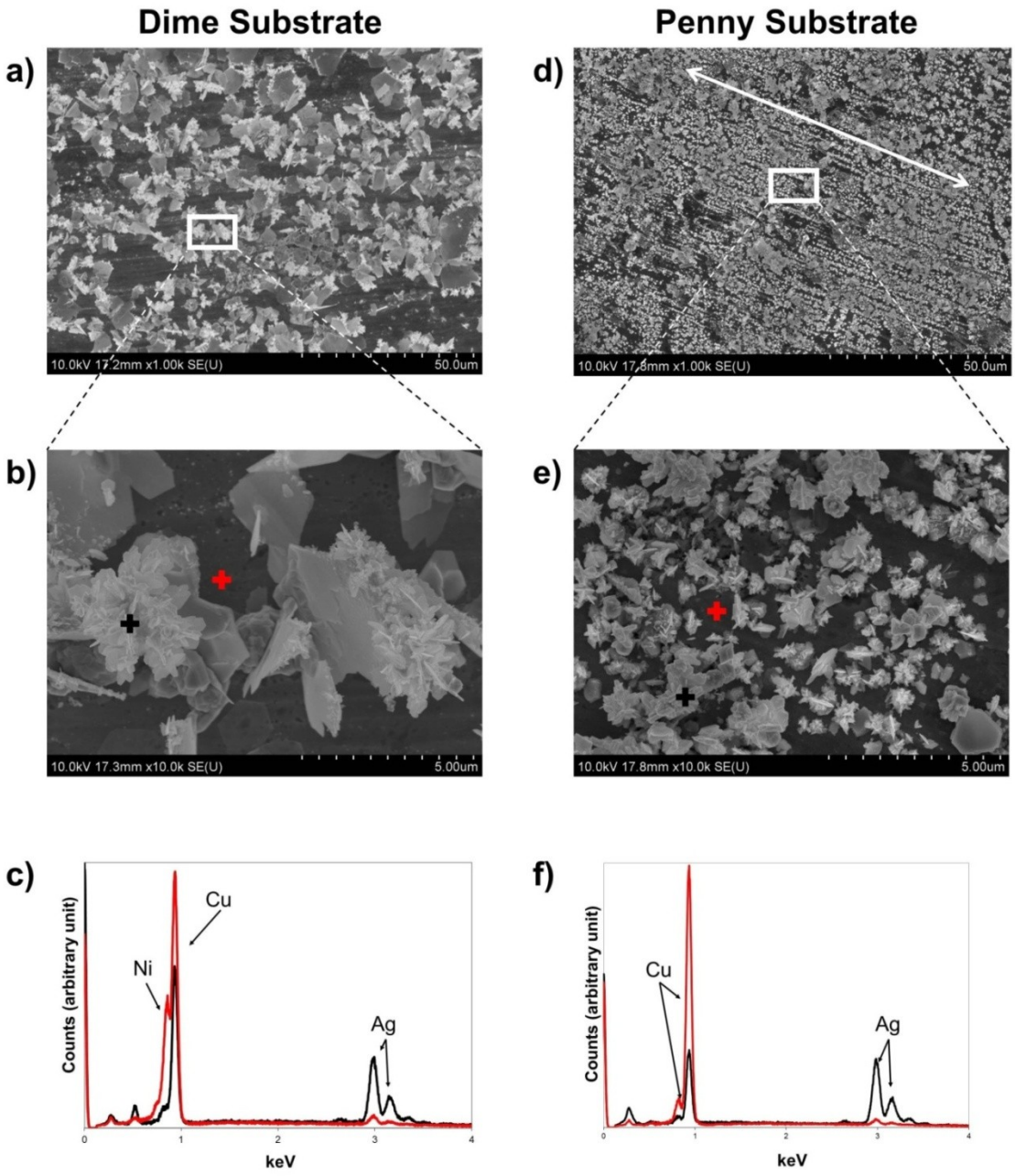
Dime Substrate
Penny Substrate
a)
d)
10.0kV 17.2mm x1.00k SE(U)
50.0um
10.0kV 17.8mm x1.00k SE(U)
50.0um
b)
e)
10.0kV 17.3mm x10.0k SE(U)
5.00um
10.0kV 17.8mm x10.0k SE(U)
5.00um
c)
f)
Counts (arbitrary unit)
Cu
Ni
Ag
keV
0
1
2
3
4

crystals which grow at different angles to the surface. These relatively flat structures tend to terminate in sharp features on the order of a few hundred nanometers in length, and less than 100 nm in width. This leaves the polyhedra with spiked features resembling nanoflowers[97], the nanodesert rose[86], and dendritic[89] or fractal[98] silver structures, which can be seen in Figure 4-4. Elemental analysis of the features (Figure 4-3c) indicates that their composition is primarily Ag, although it is difficult to quantify due to the strong signals from the Ni and Cu that compose the dime. This is not an unexpected result, as the electrons in EDS have a relatively large interaction volume. These signals can arise from electrons that pass through the Ag structures without ejecting a core electron and interact with the surrounding material, in this case Ni and Cu. This indicates that the height of the structures examined is approximately 400 nm (the X-ray range for Ag[99]) from the surface of the dime, possibly even less due to the strength of the signal from the Cu. This cannot be said for all of the structures on the dime, as there is considerable variation in feature size, as can be seen in Figures 4-3 and 4-4.

The Ag features formed on the penny are markedly different than those formed on the dime. Figure 4-3d shows a more uniform and complete coverage of the coin surface at the 1,000× magnification level, with the Ag structures exhibiting a profound linear arrangement not observed on the dime, as indicated by the white arrow. The feature size of these structures is approximately one-half to one-tenth that of the features on the dime. Interestingly, the features on the penny are similar to the sharp, spiky edges of the large polyhedra on the dime. Furthermore, these features even more strongly resemble the nanoflower, nanodesert rose, and fractal and dendritic structures found on the dime, as

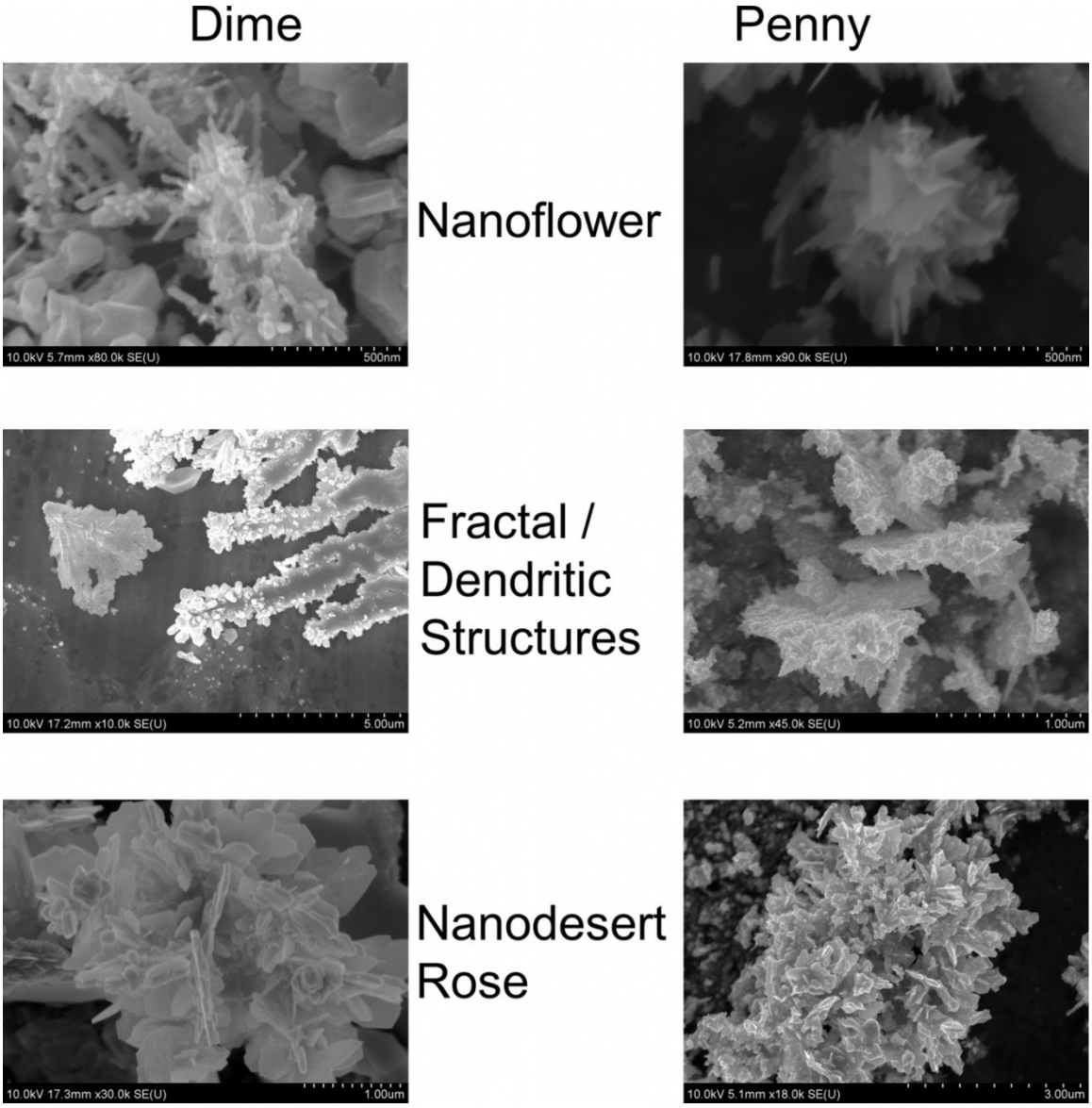

Figure 4-4. Scanning electron micrographs of the microscale and submicron features formed on the dime and penny substrates.

demonstrated in Figure 4-4. Polyhedra are still formed on the penny, but are smaller and much less frequent than on the dime. As with the dime, EDS elemental analysis of the Ag features on the penny indicate significant Ag content, but also have the strong background signal from the Cu on the penny's surface, indicating again that the structure examined is under 400 nm in height.

The difference in morphology between dime and penny substrates reflects differences underlying the surface electrochemistry governing the galvanic displacement reactions. Brevnov *et al.*[100] found that the barrier oxide layer present on Al prevents Ag ions from displacing the Al metal underlying the oxide layer, underscoring the oxide layer's inhibitory effect on the reaction. This is also the reason that many other galvanic displacement reactions use HF or strong acids to strip the native oxide present on metal or semiconductor surfaces.

In contrast, the oxides of both Ni[101] and Cu[102] are soluble in acidic solutions, with copper oxide being more soluble than nickel oxide at a given acidic pH. Because the SEM/EDS results show that the galvanic reaction occurred, we infer that the slight acidity of the solution at pH 5.5 dissolved the native oxide enough to enable the Ag ions to displace metal from the surface of the coins. Thus galvanic displacement could occur at defect sites and areas with a thinner oxide layer, without necessitating the complete removal of the surface oxide layer from the coins. This non-uniform reaction at defect sites in the passivating oxide would naturally create more nucleation points for Ag feature growth to occur on the coin surface. In turn, the greater number of starting nuclei could decrease the overall feature size for a given amount of Ag on a given surface.

To further demonstrate the importance of the surface chemistry, a more controlled and homogeneous surface was created by evaporating thin films of Ni and Cu onto glass slides and reacting with the $AgNO_3$:NH_4OH solution. As can be seen in Figure 4-5a-c, the Ni thin film has large crystalline features that are far apart, indicating that there are fewer nucleation points on Ni, resulting in large, sparse crystal growth. On the Cu thin film (Figure 4-5d-f), there are many smaller features including nanospheres, plates, and polyhedra, as well as larger, fractal structures. The comparison between the relatively smooth, controlled thin film surfaces and the rough, uncontrolled coin surfaces indicate that both surface topology and the metal being displaced play an important role in determining the ultimate structure of the substrates. In other words, the results suggest that a high density of defect sites in the oxide passivation layer on coins leads to highly heterogeneous galvanic reaction. As shown below, the limited extent of the reaction at each site produces nanostructures that are highly effective in SERS enhancement.

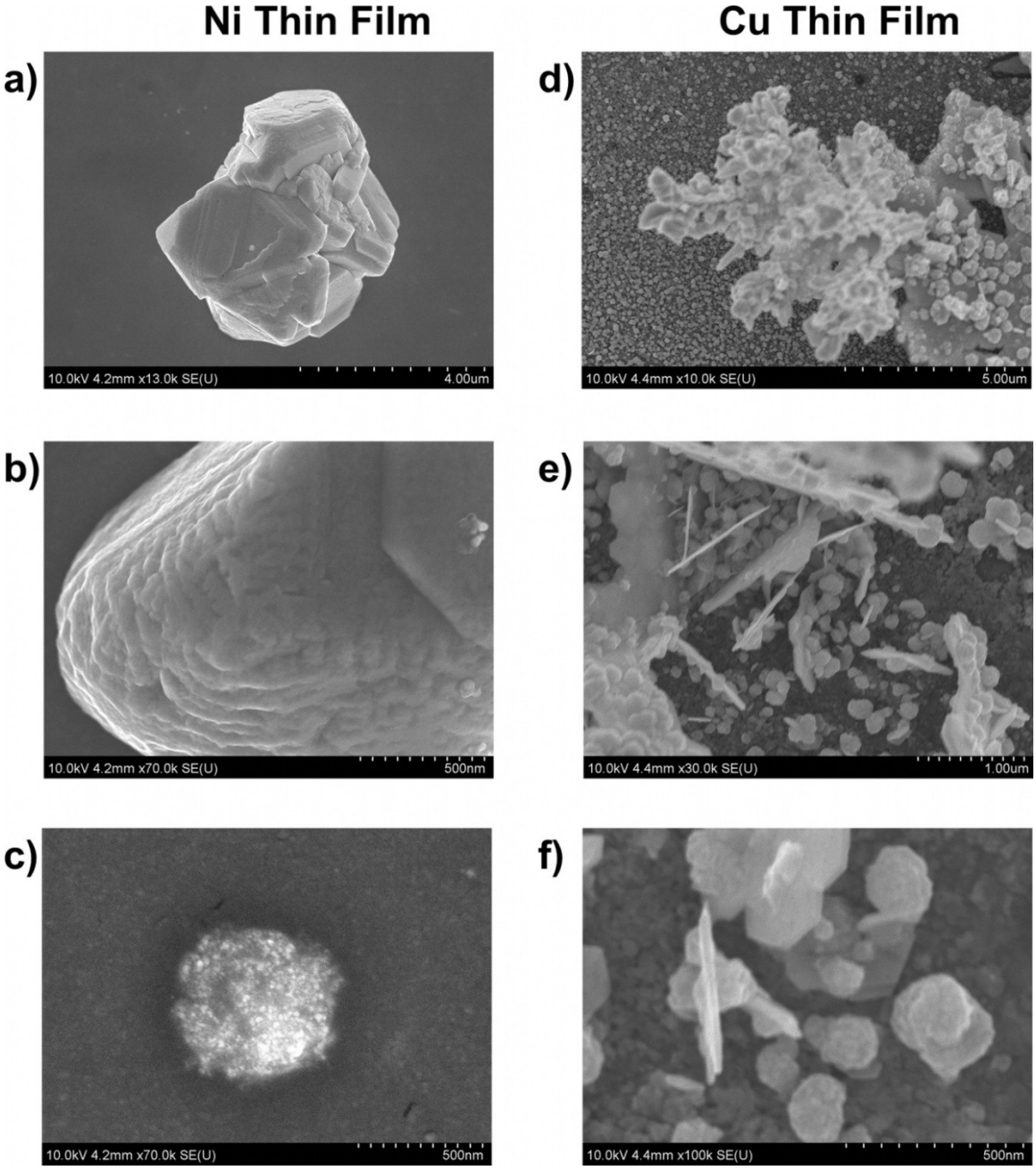

Figure 4-5. Scanning electron micrographs of reacted nickel and copper thin films. Ni thin film shows solitary crystals that are large in size as in (a), with nanoscale features as shown in (b). Small crystals also were observed on the Ni film, as in (c). The Cu thin film showed more uniform coverage with nanospheres (d-f), with fractal structures (d), plates (f), and polyhedral (f) being common.

SERS Enhancement Factor Calculation

Rhodamine-6G (R6G) was selected as the SERS probe for its large Raman cross section and the extensive characterization of its SERS spectrum in both experimental and theoretical studies. Figure 4-6 shows the SERS spectra of a solution of 1 μM R6G on the dime (Figure 4-6a) and the penny (Figure 4-6b) substrates. Prominent peaks present on both substrates, labeled in Figure 4-6, have been previously identified in experimental and DFT calculation[103] studies of R6G. Some minor peak shifting is observed from previously reported values (within ~ 4 cm^{-1}), as might be expected given the heterogeneity of naturally aged coin surfaces and particularly where localized nucleation or defect sites dominate the formation of Ag nanostructures that dominate SERS response.

An average enhancement factor was calculated for the substrates to be 1.09×10^9 for the dime substrate and 1.21×10^9 for the penny substrate using Equation 4-3:

$$EF = \frac{I_{SERS} / N_{SERS}}{I_{Raman} / N_{Raman}} \qquad \text{(Equation 4-3)}$$

where I_{SERS} is the count rate for the SERS substrate, N_{SERS} is the estimated number of molecules in the laser spot on the SERS substrate, I_{Raman} is the count rate of an unreacted thin metal film not exposed to the $AgNO_3$:NH_4OH solution, and N_{Raman} is the estimated number of molecules in the laser spot on the unreacted thin metal film. N_{SERS} was approximated by assuming uniform coverage of R6G on the coin surface, and approximating the surface of the coin to be the geometric area of the coin's face. N_{Raman} was approximated by assuming uniform coverage of R6G over the unreacted thin film

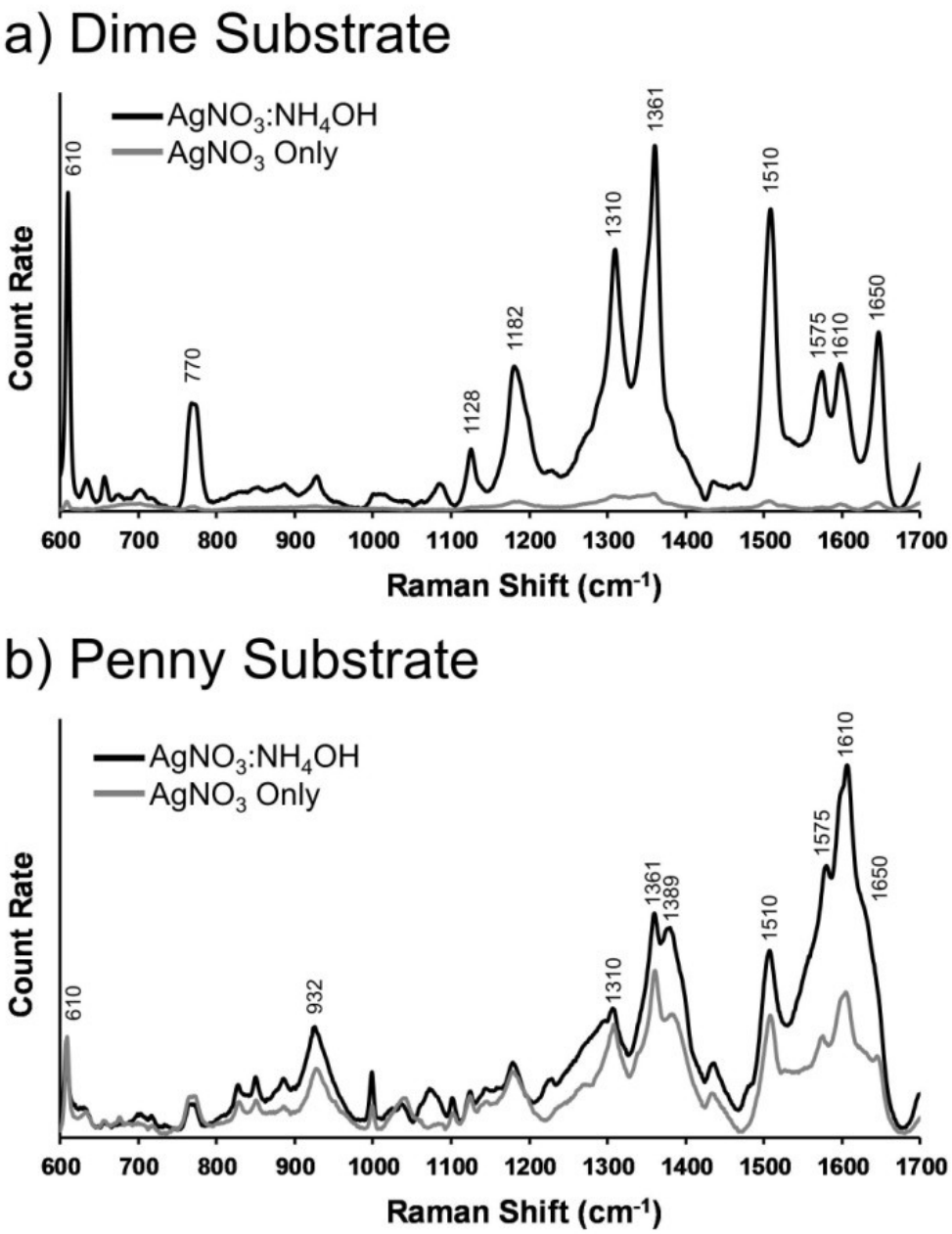

Figure 4-6. SERS spectra of 1 μM R6G on the dime (a) and penny (b) substrates. The black spectra are from the substrates formed using the $AgNO_3$:NH_4OH mixture as described, and the grey spectra are from substrates formed using only $AgNO_3$ solution. The peaks are consistent with those previously identified for R6G[103]. The presence of NH_4OH increases the photon count rate of the dime substrates by a factor of ten, and that of the penny substrates by a factor of two.

surface. Because roughened Ni and Cu surfaces are known to exhibit SERS behavior[104], the unreacted thin films were used as references to evaluate the enhancement factor of the substrates to control for the inherent heterogeneity in the topography of the coin surfaces.

To account for the spatial inhomogeneity of the coins, we recognized that the laser used to acquire these spectra has a spot radius of approximately 2 μm, which is large enough to encompass several of the larger features and their associated small, sharp features found on the dime, as well as many of the smaller features prevalent on the penny. This indicates that highly enhancing "hot spots" were approximately equal in number for the areas scanned, yielding similar average enhancement factors.

While the enhancement factors and limits of detection are nearly the same for the dime and penny substrates, there is up to an order of magnitude difference in the photon count rates of the two substrates, with the penny substrates exhibiting a higher count rate. This difference could be due to a number of different factors, including the difference in the standard reduction potentials for the metals on the coin surface, differences in the surface oxide thickness or reactivity toward the $AgNO_3$:NH_4OH solution, the number of nucleation sites at which silver can be reduced, the reaction rate, or even the bumps and scratches acquired over the individual history of each coin.

Effect of NH_4OH

The addition of NH_4OH to the $AgNO_3$ solution improves the photon count rate for the dime substrate by a factor of ten (Figure 4-6a) and the penny substrate by a factor of two

(Figure 4-6b), on average. When mixed with $AgNO_3$, the NH_4OH will coordinate Ag^+ cations, forming a diammine silver (I) complex, which changes the standard reduction potential from about +0.799V for Ag^+ to about +0.366 V[105]. While this affects only about one sixth of the available Ag^+ cations, given the solution composition, the resulting lower Gibbs free energy change of the reaction would imply that the coordinated Ag^+ cations could only react at the most favorable nucleation sites on the coin's surface or on already growing silver crystals. As the coordinated Ag^+ ion gets reduced, the NH_3 is then free to coordinate other cations in solution[90], potentially prolonging the effect. Ko and Lee[102] found a similar effect on the dissolution of copper oxide using $HClO_4$ with monoethanolamine, noting that the surface roughness reached a maximum around pH 6, close to the pH of the solution used in this paper. Furthermore, the free NH_3 can also coordinate metal cations released from the coin surface, preventing Ag^+ from oxidizing M^+ to M^{2+} in solution, where M is Ni for the dime and Cu for the penny. This would require the reduction of Ag^+ to take place at the coin surface or on an already growing silver crystal.

SERS Reproducibility

As is the case with many SERS substrates formed by random processes, the galvanic SERS sites from dime and penny substrates present challenges for quantitative or semi-quantitative applications. Figure 4-7 shows the reproducibility of signals from 1 μM R6G from different substrates formed on the same type of coin. The absolute intensity of signals from the dime (Figure 4-7a) varies by less than an order of magnitude, and the

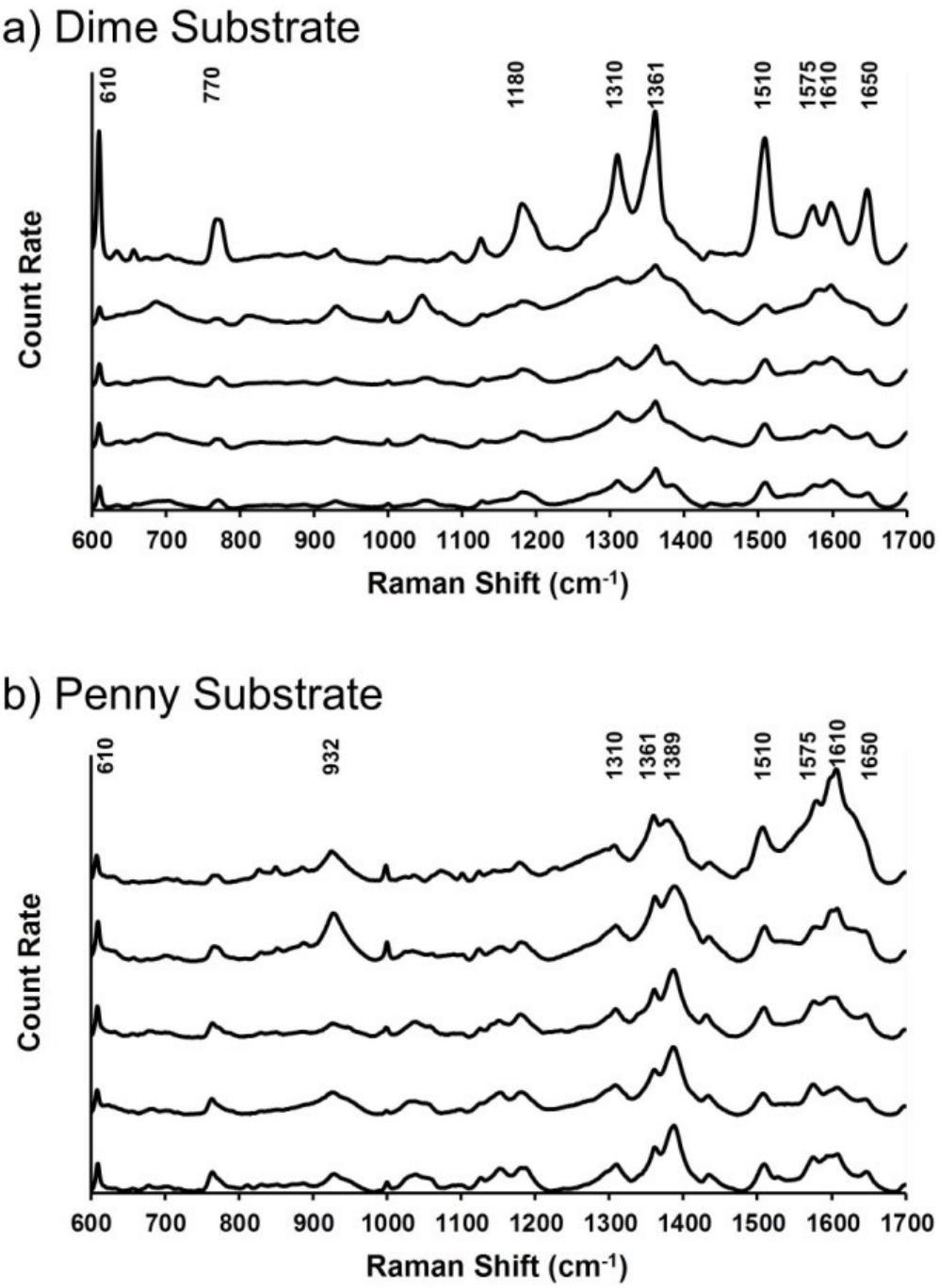

Figure 4-7. Reproducibility of SERS signals from 1 μM R6G on dime (a) and penny (b) substrates. Spectra are offset for clarity. The dime substrates exhibit more than twice the variability of the penny substrates, and are approximately an order of magnitude weaker in absolute signal intensity.

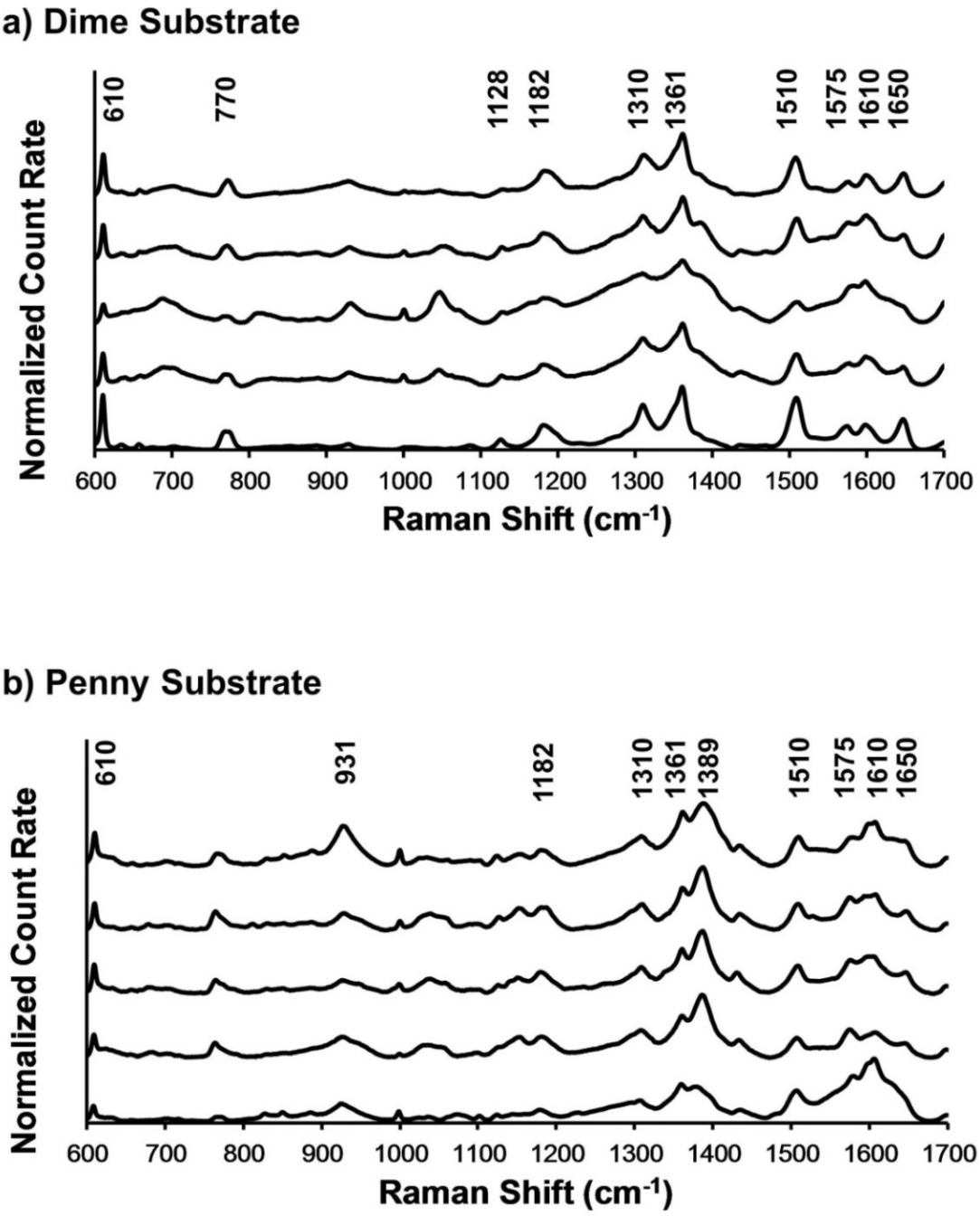

Figure 4-8. Normalized SERS spectra of 1 μM R6G showing that each spectrum can be reliably identified on different dime (a) and penny (b) substrates, despite the variability in signal intensity in Figure 4-7.

molecule can still be identified readily in every case by examining the normalized intensities (Figure 4-8a). The same holds true for the penny substrates, as demonstrated by Figure 4-7b and Figure 4-8b. While the reproducibility of this method could be improved with additional microfabrication, processing, or reagents[84, 106], that would run counter to the goal of creating a simple, fast, and inexpensive substrate.

Galvanic SERS Substrates for Melamine Detection

The effectiveness of these SERS substrates was demonstrated in an application where portable and rapid detection of contaminants could serve as a complement the traditional analytical methods, namely by detecting excessive amounts of melamine in melamine-spiked infant formula. Melamine has been added illegally to pet food, infant formula, and other foodstuffs to increase the total amount of nitrogen in the food, which in turn passes for increased protein content as measured in standard tests. This causes an anomalously high value for the amount of protein in a sample as reported by standard tests which rely on the total nitrogen content of a sample to estimate protein levels. Melamine can hydrogen bond with cyanuric acid other related compounds formed during melamine synthesis and disposal to form insoluble crystals, which can lead to renal failure[107]. A rapid, point-of-sampling detection system could be developed to detect melamine contamination of foodstuffs by combining the SERS substrates from the present work with a portable Raman spectrometer, allowing more samples to be screened in the same amount of time while simultaneously reducing the burden on other analytical instruments.

Since we previously determined that copper-based substrates worked better than nickel-based substrates, we chose to use both a penny and commercially available copper tape to create simple and portable SERS substrates. To demonstrate the ability of these substrates to detect melamine in infant formula, the formula was prepared according to the manufacturer's directions, used as prepared or mixed with melamine at 1000 ppm, 100 ppm, 10 ppm, 5 ppm, or 1 ppm, and dried on dime and penny substrates before being scanned. Figure 4-9a and b show the results on the tape and penny substrates, respectively. Unadulterated formula (0 ppm) has a broad peak spanning 650-750 cm^{-1}, as shown in Figure 4-9. Melamine contamination shows up as a distinct peak centered near 686 cm^{-1}, as can be seen clearly in the 1000 ppm and 100 ppm levels for both substrates in Figure 4-9. This peak is in good agreement with the major peak observed by Lin *et al.*[108] and Koglin *et al.*[109], which both groups assign to an in-plane deformation of the triazine ring of melamine, ring breathing vibrational mode II. At 10 ppm and below, the 686 cm^{-1} peak becomes more broad and shallow, yet still remains distinguishable down to the 5 ppm level. This allows for the rapid and simple SERS detection of melamine-contaminated infant formulas at levels down to 5 ppm, which could be used to quickly screen for melamine contamination in infant formula or other foodstuffs.

One potential drawback of using a random reaction such as galvanic displacement is that the substrates that form are often highly variable in morphology and hot spot distribution, yielding a variable SERS signal. Another potential source for variability in the signal is the inhomogeneity of the surfaces introduced during the manufacture and processing or circulation of the tape and coin, respectively. The variability of the

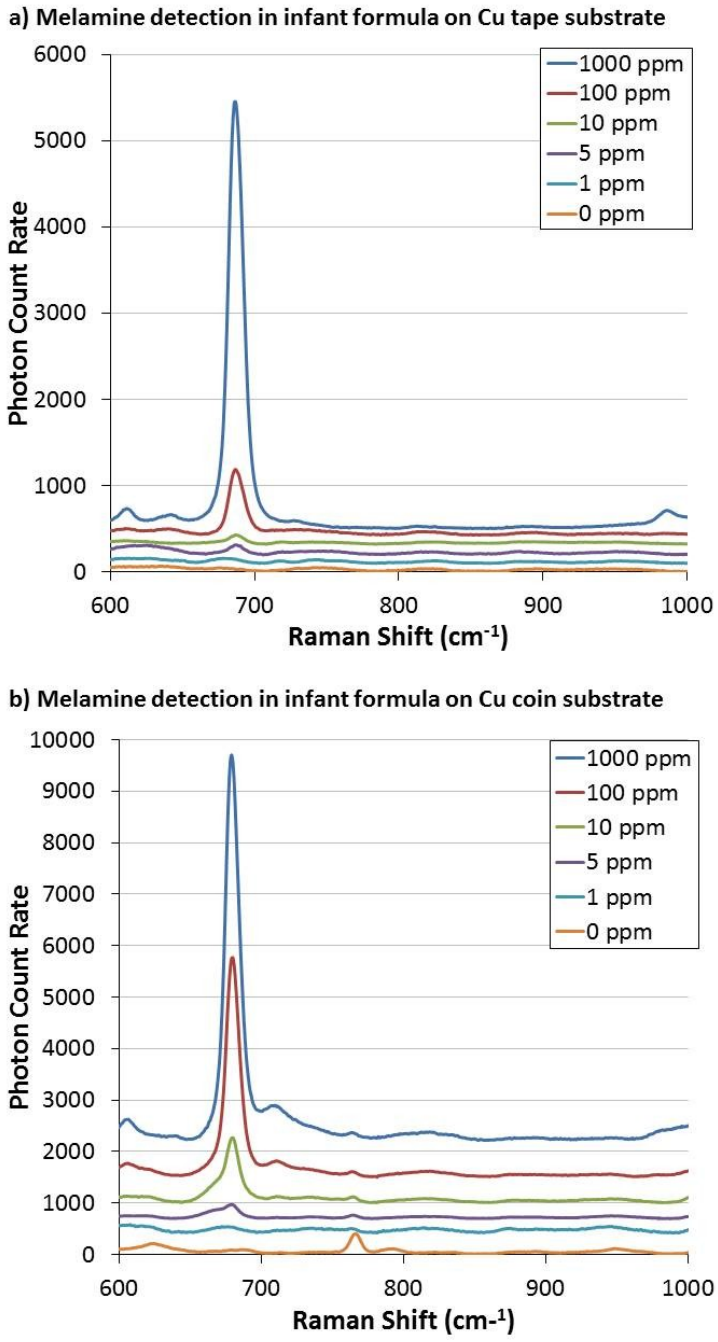

Figure 4-9. Average SERS spectra of melamine adulterated commercially available infant formula on Ag substrates formed on (a) Cu tape and (b) a Cu coin. The peak centred around 680 cm^{-1} is due to an in-plane deformation of the triazine ring of melamine, which can clearly be distinguished down to the 5 ppm levels in both cases. Spectra are offset to better show the characteristic melamine peak.

substrates was assessed by calculating a coefficient of variation (CV) for different points of the same sample droplet, a CV for different substrates, and for the Cu coin substrates, a CV for different points within the same substrate. These CVs are summarized in Table 4-1. The Cu tape substrates are less variable than the Cu coin substrates on average, which is not unexpected. The coins come from circulation and have a high degree of surface heterogeneity, which is believed to be the main source of variability between substrates formed on different coins.

Given these sources of variability, we examined the substrates using scanning electron microscopy to look for similarities since the limits of detection and average photon count rates were similar between the two substrates. Figure 4-10 shows two scanning electron micrographs, each revealing a wide variety of fractal, dendritic, and polygonal Ag structures, consistent with previously published descriptions of structures formed by galvanic displacement reactions. It is believed that the large number of branching points and facets created by the galvanic displacement reaction result in a multitude of enhancement hotspots distributed across the surface of the substrate. Furthermore, Figure 4-11 shows that on the Cu tape, Ag structures tend to form in a linear arrangement, forming along the surface striations of the Cu tape.

Comparison with Other SERS Detection Methods for Melamine

Despite the global health concern over food supply security, there were relatively few published papers addressing the detection of melamine-adulterated foodstuffs using SERS. A comparison with a selection of these papers published at the time of

Table 4-1: Coefficients of variation for the substrates

Substrate Type	**Sample CV**	**Substrate CV**	**Point CV**
Cu Tape	0.506	0.702	N/A
Cu Coin	0.534	0.998	0.385

Sample CV is the coefficient of variation for 10 different spectra acquired within the same sample droplet. Substrate CV is the coefficient of variation between five different substrates each with ten spectra. Point CV is the coefficient of variation for five different samples tested on the same coin substrate. The CV was calculated by integrating the area of the characteristic peak for melamine in the 1000 ppm case and dividing the standard deviation of these areas by the mean of the areas.

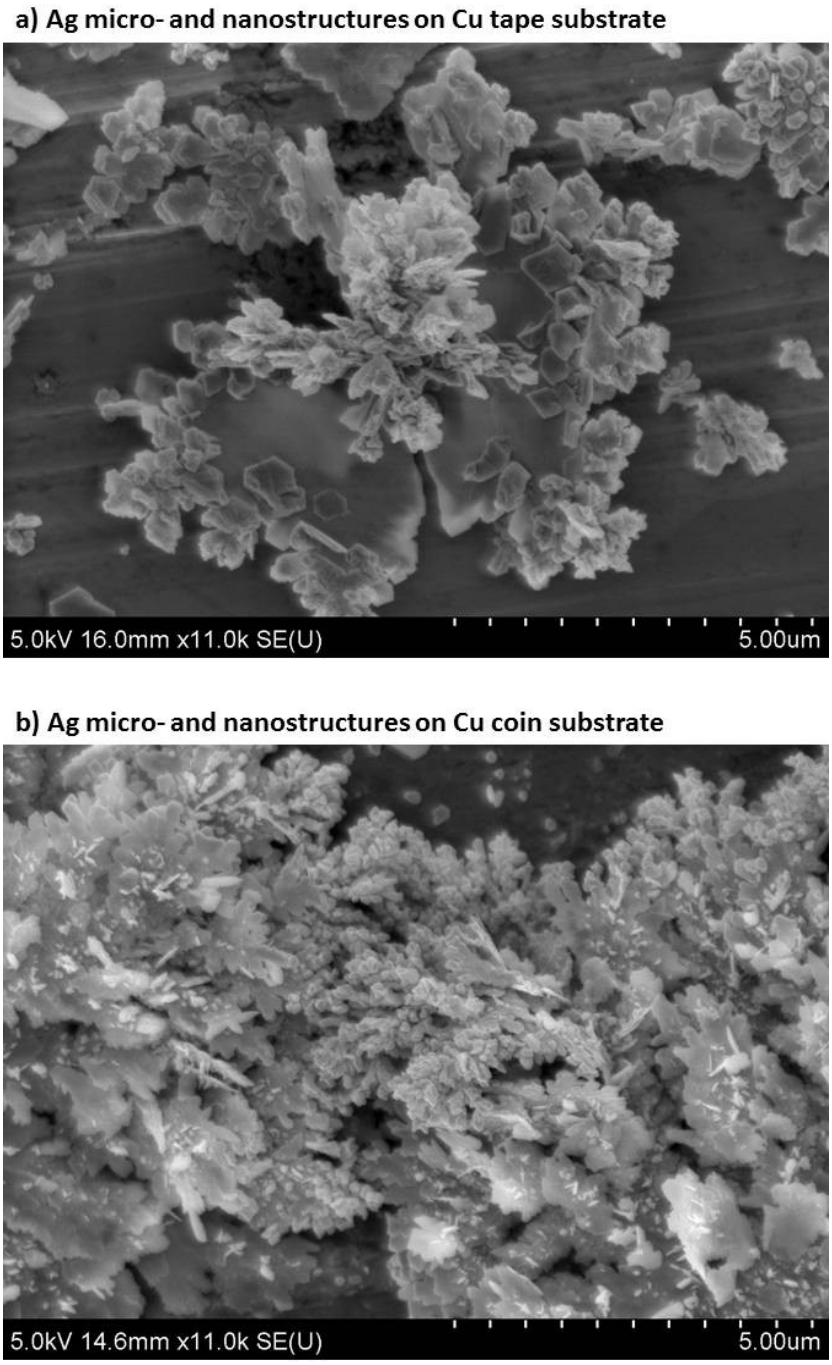

Figure 4-10. Scanning electron micrographs of representative fractal, dendritic, and polygonal Ag structures formed on Cu tape (a) and a Cu coin (b) by galvanic displacement.

a) Micro- and nanostructure growth following Cu tape striations

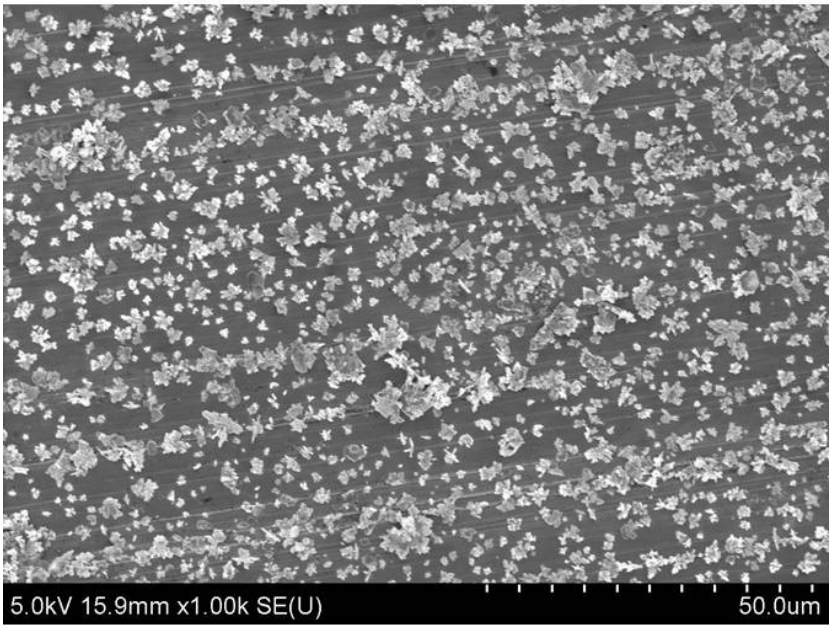

b) Lower magnification image showing growth along striations

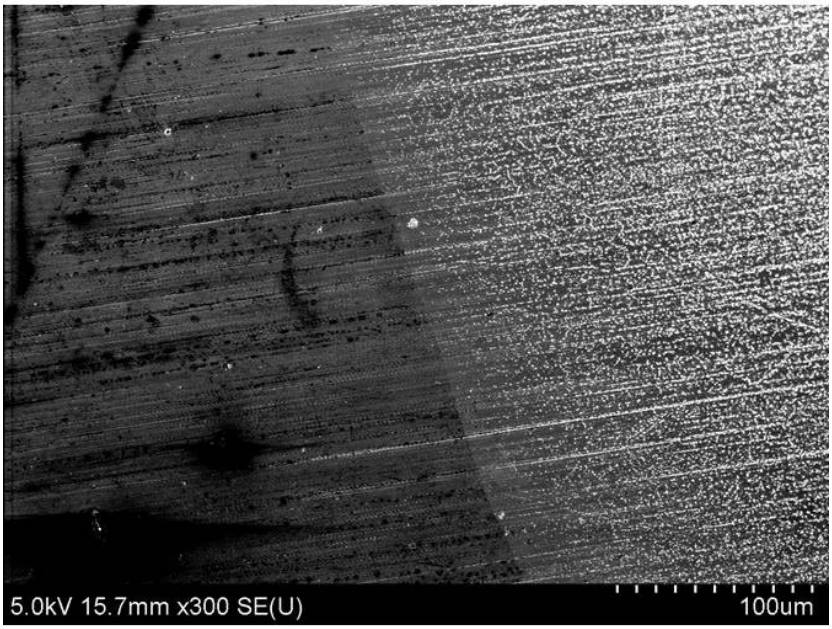

Figure 4-11. Scanning electron micrographs of the substrate created on Cu tape. Micro- and nanostructure growth is observed to align with the surface striations on the Cu tape which presumably arise during the manufacturing and processing of the tape itself.

publication[108-111] is in order to evaluate the relative advantages of this method. The majority of the papers detail detection of pure melamine preparations, as exemplified by Koglin et al.[109] and Du et al.[110]. The most relevant comparisons come from those papers that describe the detection of melamine in food, due to the fact that other compounds present in the food may compete for binding sites on the SERS substrate and reduce the overall signal from melamine. The only two known to the publications at the time were those of Lin et al.[108] and Lee et al.[111].

Lin et al. used a commercially available SERS substrate, and demonstrate detection in the range of 500 – 1,000 ppm for four different types of food after extracting melamine with a 50% (v/v) acetonitrile/water mixture. These levels of melamine contamination are still several orders of magnitude larger than those allowable in food for human consumption. Lee *et al.* used Au nanoparticles to detect melamine in powdered milk at 100 ppm after 10 minutes, and 200 ppb after immersing a roughened Au electrode in the melamine/milk solution for one day, yielding improved limits of detection without the need for solvent extraction or other pretreatment methods. While the limit of detection is an important factor in selecting a SERS substrate, one must also consider sample preparation time and complexity. The simple, fast, and robust substrates presented here represent a promising technique for portable, semi-quantitative SERS applications.

We also compared the performance of our inexpensive and portable substrates with Klarite, a commercially available SERS substrate, in Figure 4-12. Detection of melamine extracted and purified from food samples has previously been shown using Klarite[108, 112], so we sought to ascertain its performance without any sample

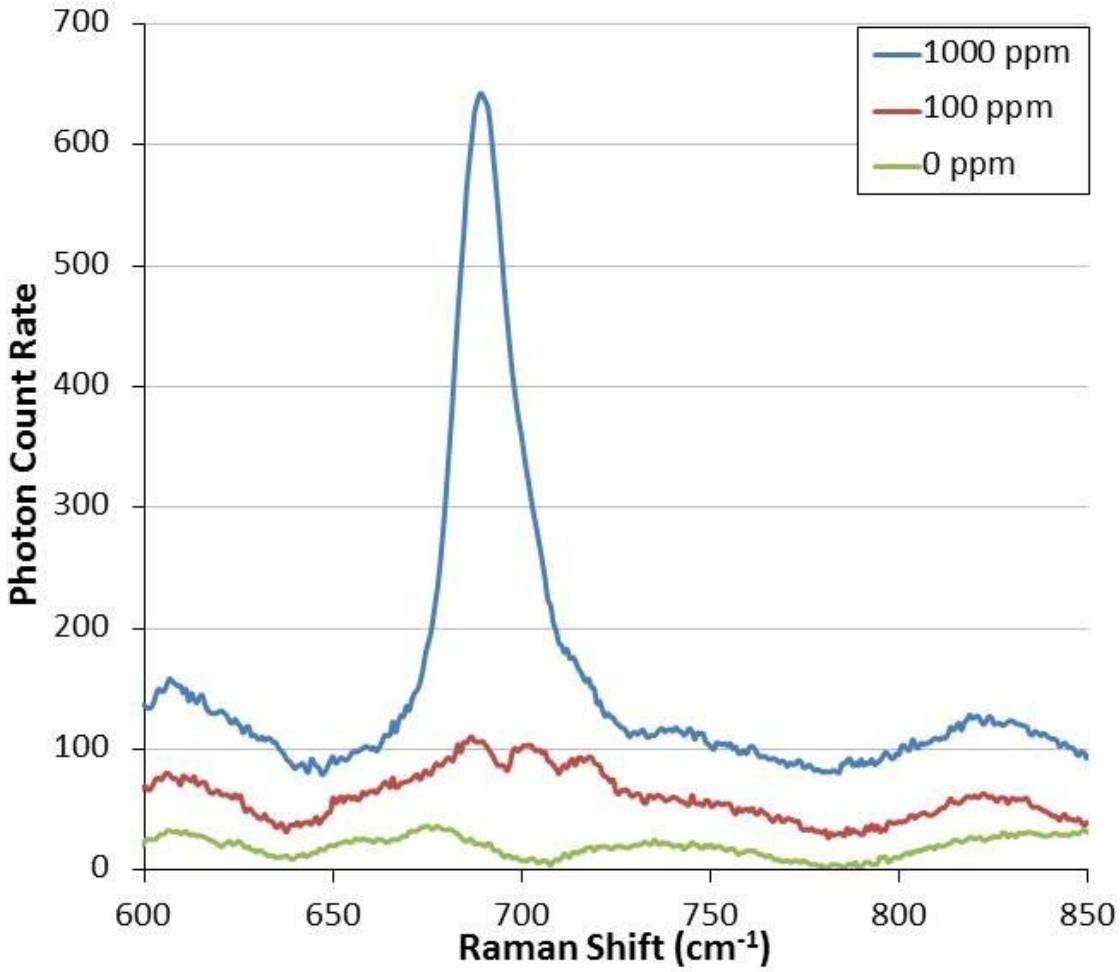

Figure 4-12. Average SERS spectra of melamine adulterated commercially available infant formula on Klarite, a commercially available SERS substrate. Note that the 680 cm^{-1} peak is readily identifiable at the 1000 ppm level but not at the 100 ppm level. Spectra are offset for clarity.

preparation. Figure 4-12 shows spectra from normal infant formula (0 ppm) and infant formula adulterated with 1000 ppm and 100 ppm melamine using experimental conditions identical to those responsible for Figure 4-9. The 680 cm-1 peak can be seen readily at the 1000 ppm level, but is not apparent at 100 ppm. While the integrated peak area on the Klarite substrate has a lower CV (0.34) than the substrates formed by galvanic displacement, it cannot be used under the same conditions to detect melamine contamination of infant formula. Thus, these simple, inexpensive, and portable substrates reported here show up to 200-fold better detection of melamine contamination in infant formula without pre-treatment than do the more expensive, commercially available Klarite substrates.

Future work

Substrate morphology control with galvanic displacement

Given that the Raman scattering enhancement is governed by the nanoscale geometry of the substrate, controlling the morphology and distribution of the resulting nanoscale features is essential for creating highly enhancing and reproducible substrates. While there are currently no reports of quantitative substrates formed by galvanic displacement, there are galvanic displacement substrates that offer reproducibility within 10-15%. These methods require the use of HF[113-116] and long reaction times[115], excluding them from consideration as simple SERS substrates amenable to portable analysis. Brejna and Griffiths used microsphere lithography to demonstrate a method to control substrate morphology and nanostructure spacing, but the extensive amount of processing necessary

(including the use of HF) to fabricate these substrates precludes them from consideration as simple SERS substrates[114]. A general method for creating simple, portable, quantitative, and reproducible substrates by galvanic displacement has not yet been put forth. We believe that by controlling the surface chemistry and characteristics of the metal or semiconductor to be displaced and the composition of the displacing solution, the problem of substrate reproducibility, which is directly related to crystal morphology and distribution, can be greatly reduced while still maintaining the excellent enhancement characteristics and simple preparation methods of galvanic displacement substrates.

Many of the previous reports of SERS substrates formed by galvanic displacement[89, 97, 113-117] relied on the use of HF to remove the native oxide layer present on metal and semiconductor surfaces, since the native oxide layer inhibits galvanic displacement[100] and defects in the oxide are believed to act as nucleation points for crystal growth. In the simplest cases, this harsh treatment is unnecessary with many metals including Al[94] and Cu[57, 118]. Since many metal oxides are amphoteric, acidification of the displacing solution, especially using a metal with a common anion (e.g. HNO_3 for $AgNO_3$ solutions), can help to remove the native oxide layer and facilitate galvanic displacement without requiring the use of concentrated acids or HF to form the substrate. Amphoteric metal oxides can also be dissolved using a basic solution, expanding the parameter space for the galvanic displacement reaction. The anions of these basic solutions can complex Ag^+ and Au^{3+}, which alters the effective reduction potential of the ions[119], changing the free energy of the reaction. Furthermore, there is evidence that the anion plays an important role in determining the morphology of the

structures that form due to standard reduction methods of nanoparticle synthesis[119] as well as galvanic displacement with Ag[118]. One could conceivably adjust the composition, pH, and free energy of the galvanic displacement solution to allow for the creation of more structures with a given morphology that produce highly enhancing SERS substrates for a given application.

Additives such as polyvinylpyrrolidone (PVP), KI, and cetyl trimethylammonium bromide (CTAB) also have been shown to influence substrate morphology in galvanic displacement reactions[120]. PVP is a common capping agent used in the synthesis of Ag nanocubes, and directs growth along the <111> direction by adsorbing selectively to the <100> facets[121]. In the case of galvanic displacement of Zn by Ag, Lv *et al.* found that Ag tends to form spherical structures with nanorods extending radially, similar to the shape of a sea urchin[120]. When they replaced PVP with KI, the structures formed a porous, irregular, interconnected mesh of Ag nanosheets. The addition of CTAB, a detergent commonly used in the formation of Au nanorods[122], results in the growth of rod-like aggregates. Furthermore, Lv *et al.* found that the presence of halide anions (I^- from KI and Br^- from CTAB) changed the nature of the reaction from a thermodynamically governed system to kinetic control which they say favors anisotropic growth of Ag particles. The order and timing of the addition of these compounds could also be adjusted to further control the morphology of the substrates. For example, since the additives mentioned result in Ag structures dominated by {111} facets, adding them to the reaction at a later time point may allow for the formation of new morphologies by

allowing early isotropic growth of nanoparticles prior to Ostwald ripening and formation of rods or dendrites[123].

Engineering well-defined oxide defects as sites for galvanic displacement

Another approach to controlling the galvanic displacement reaction would be to directly engineer the metal oxide layer itself. One example of such a method is shown schematically in Figure 4-13. While the most common method to control the oxide is to remove it entirely using acid, this need not be the only approach. Several of the techniques necessary to do this very precisely and in a controlled fashion are currently prohibitively expensive and highly specialized, and thus research in this area would primarily serve to answer the question as to whether engineering the metal oxide layer itself could control the galvanic displacement reaction. Atomic layer deposition (ALD) is a technique used extensively in the semiconductor and other industries to produce thin films with unprecedented uniformity at the atomic scale, achieved by means of an alternating, self-limiting surface reaction of metal precursors and oxidizers in ultrahigh vacuum conditions. Recent reports have extended ALD to roll-to-roll processing under atmospheric pressure conditions, driven by the dramatic lowering of cost this will achieve[124]. This can be used to tune the plasmonic properties resulting from controlled galvanic reaction with the underlying substrate[125]. Given the uniformity and control over the thickness of the oxide layer, a highly uniform metal oxide film could be deposited, and defects could then be introduced using other techniques common in the

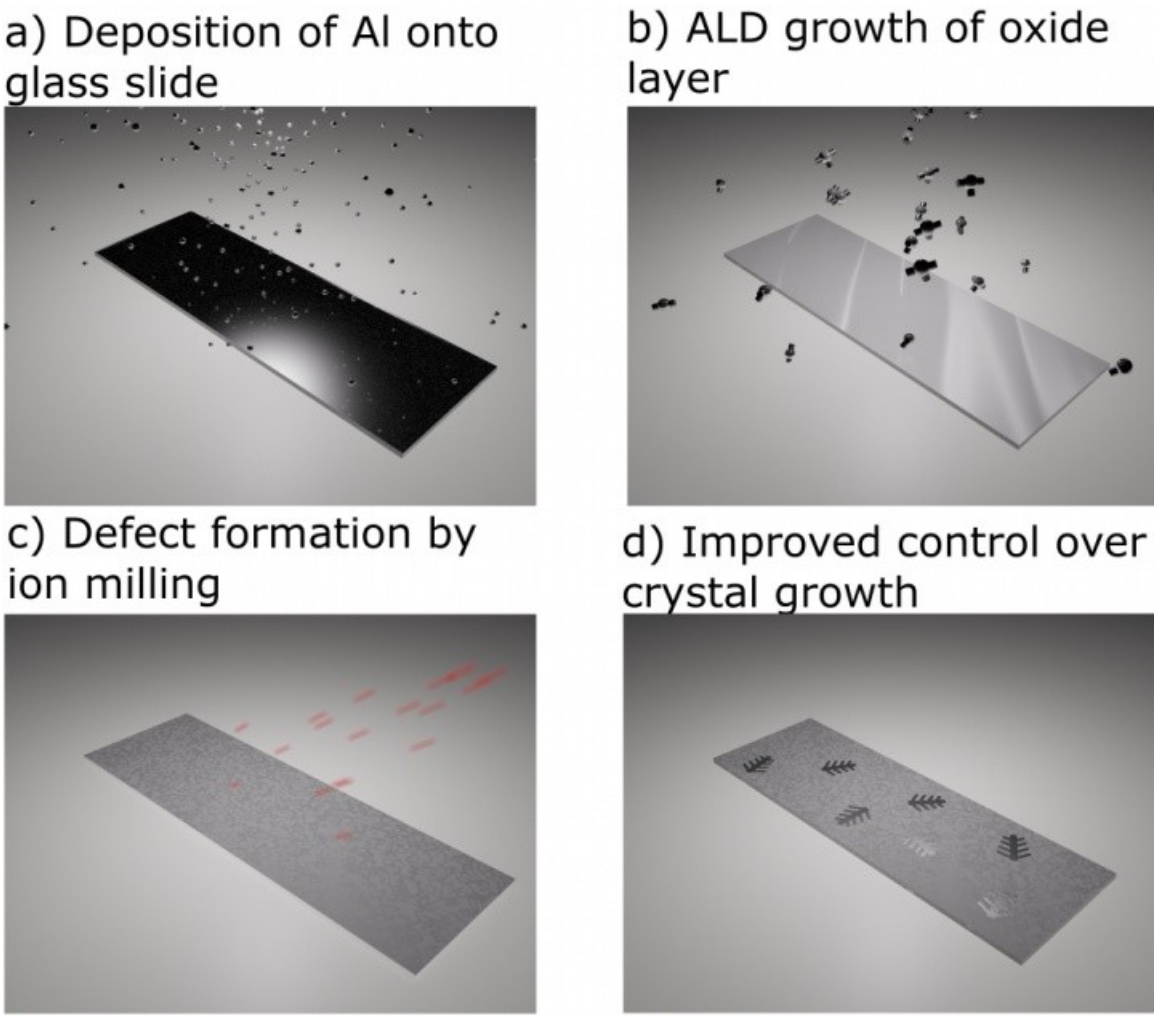

Figure 4-13. Schematic overview of how to control the galvanic displacement reaction. a) Aluminum is deposited onto a cleaned glass slide. b) Aluminum oxide is grown conformally over the aluminum metal by atomic layer deposition. c) Defects are introduced into the aluminum oxide layer by ion milling. d) A more controlled defect distribution should yield improved control over the resulting SERS-active dendrite structure and size.

semiconductor industry, such as ion implantation, ion milling, or focused ion beam ablation. By controlling the parameters of these techniques, one could achieve a desired density of defects in the oxide layer, such that the defects are all very similar (monodispersed). Uniform defect characteristics in the oxide could enable considerably more uniform SERS structures to be formed at those defects, as compared to galvanic reaction at random defects in a native oxide that has evolved without control.

A preliminary, proof-of-principle study of the effects of defects in the oxide layer on the resulting structures that form due to galvanic displacement and subsequent SERS enhancement was performed by thermal evaporation of 100 nm of aluminum metal onto a cleaned glass slide. Without breaking vacuum, the glass slide was transferred to a Cambridge Nanotech Fiji F200 atomic layer deposition (ALD) system maintained at a base pressure of 1×10^{-6} Torr and a temperature of 250ºC, where a conformal 3 nm layer of Al_2O_3 was deposited by ALD using trimethylaluminum (TMA) as the metal source precursor and H_2O as the oxidant precursor with a continuous flow of 200 mTorr Ar gas. Precursors were unheated and were pulsed for 0.06 seconds, followed by a purge of 10 seconds. This resulted in an Al_2O_3 film growth rate of 1.0 Å/cycle with a film nonuniformity of <1%. Film thickness was measured using a J. A. Woollam M-2000D Ellipsometer and a Cauchy optical model for the ALD Al_2O_3. Following ALD film growth, the slide was subjected to Ar plasma at 4 sccm with an extraction voltage of 500 V and an accelerating voltage of 1000 V for 30 seconds using a Veeco Mark III ion source before being removed from vacuum and treated with 10 µL 50 mM $AgNO_3$ for 30 seconds and rinsed with 20 µL deionized water. SERS was performed with 2 µL of 1 µM

R6G as above, except the acquisition conditions were 300 averages of 3 seconds integration time at five points.

The results of preliminary experiments utilizing ALD and argon plasma engineer the oxide layer defect density are shown in Figure 4-14. Two slides were prepared and examined as described, with the difference between the two being the amount of time in between Ar plasma milling of the Al_2O_3 layer and the reaction with $AgNO_3$. The first slide (Figure 4-14a through Figure 4-14c) was reacted as soon as the slide was cool enough to handle safely. The second slide (Figure 4-14d through Figure 4-14f) was removed to atmospheric pressure for 30 minutes before being reacted with $AgNO_3$. This was to allow atmospheric oxygen to reoxidize any exposed bulk aluminum or oxide layer defects generated by argon plasma treatment. The slides were placed half-way into the plasma stream, with one side being exposed to a higher Ar ion flux than the other, creating a gradient of oxide defects. The plasma etch rate, the ion flux, and the prevalence of doubly-charged Ar ions have not been characterized under these operating conditions, but the etch rate for Al_2O_3 is expected to be greater than 2 nm/minute.

In the case of the slide reacted immediately after removal from the vacuum chamber, there is a clear difference in the particle morphology as a function of distance from the point of maximum ion flux. Optical microscopy shows a variety of structures (Figure 4-14a) that differ from those further away from the point of maximum flux (Figure 4-14b and c). The trend is towards much larger structures forming at greater distances from the point of maximum ion flux.

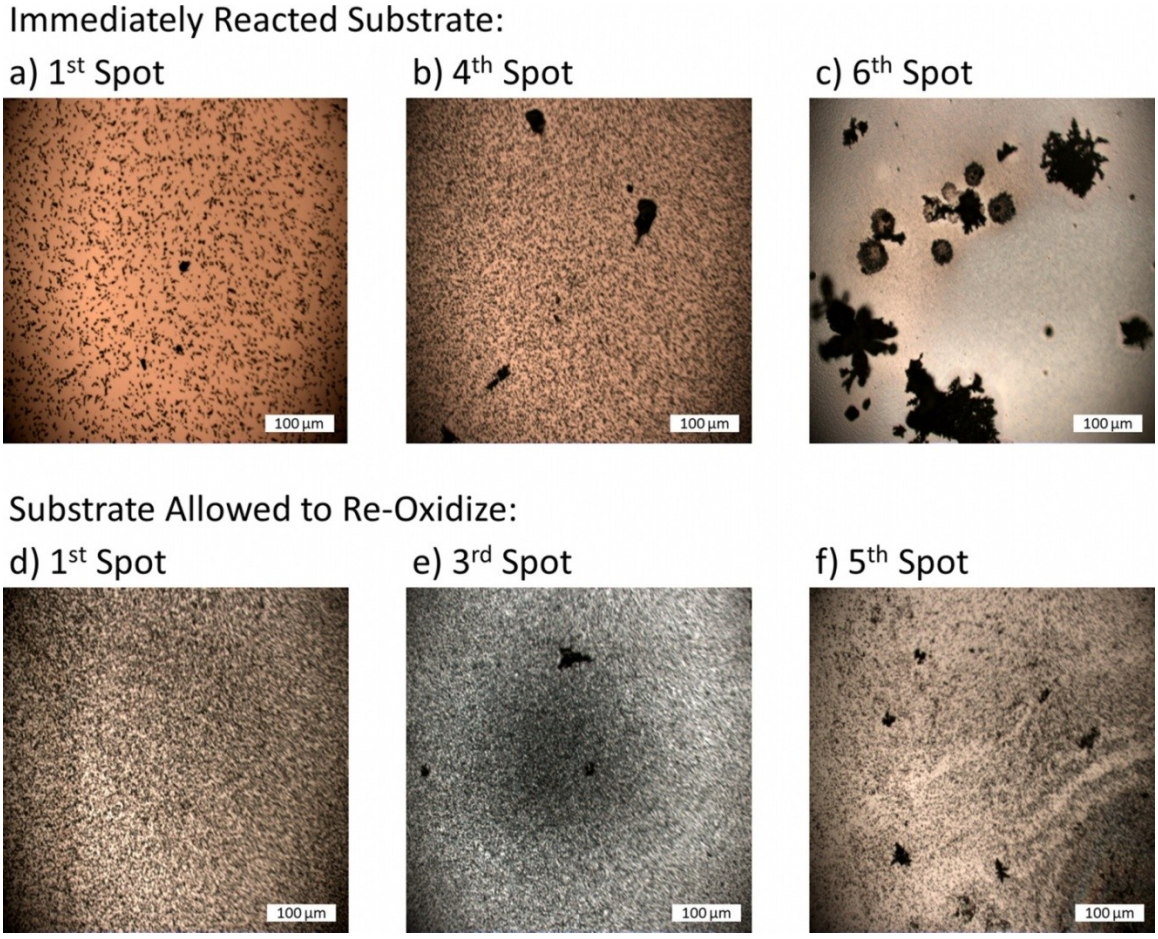

Figure 4-14. Optical microscopy of the particle morphology and distribution on two different slides with a uniform aluminum oxide layer formed by ALD. One slide was reacted immediately with $AgNO_3$ after being removed from the vacuum chamber (a-c), and the other slide was allowed to sit at atmospheric pressure for 30 minutes prior to reaction (d-f). The first spot is located closest to the maximum ion flux from the Ar plasma.

This is attributed to a lower ion flux density, and thus a lower areal density of defect sites at which galvanic displacement can occur. The lower defect density causes larger structures to form by diffusion-limited growth due to the Ag^+ atoms not having as many sites at which reduction can occur, leading to increased growth at the sites where reduction is able to occur. Due to the current configuration of the system, the point of maximum ion flux receives no aluminum due to the positioning of a shutter in the evaporation chamber. Future work with this system might involve a redesign to allow for a more complete characterization of the influence of ion flux.

The slide that was removed to atmospheric oxygen shows more homogeneous particle morphology under the optical microscope (Figure 14d-f). Larger structures do eventually form further away from the point of maximum ion flux, but the difference is nowhere near as apparent as on the slide that was reacted immediately. The reason for this is as yet unclear, and more powerful materials characterization techniques, such as electron microscopy, should be used to determine whether there is an effect on particle morphology and distribution at the nanoscale. Additionally, parameters such as the accelerating voltage, plasma exposure time, and ALD oxide thickness should be explored to understand their influence on resulting particle morphology.

SERS activity of 1 μM R6G was evaluated for each point on both of these slides, and the results are shown in Figure 4-15. The variability was characterized by plotting the median and interquartile range of the spectra at each point on the slides, as shown in Figure 4-15a for the slide reacted immediately and Figure 4-15b for the slide that was reacted after being exposed to atmospheric oxygen for 30 minutes. The slide that was

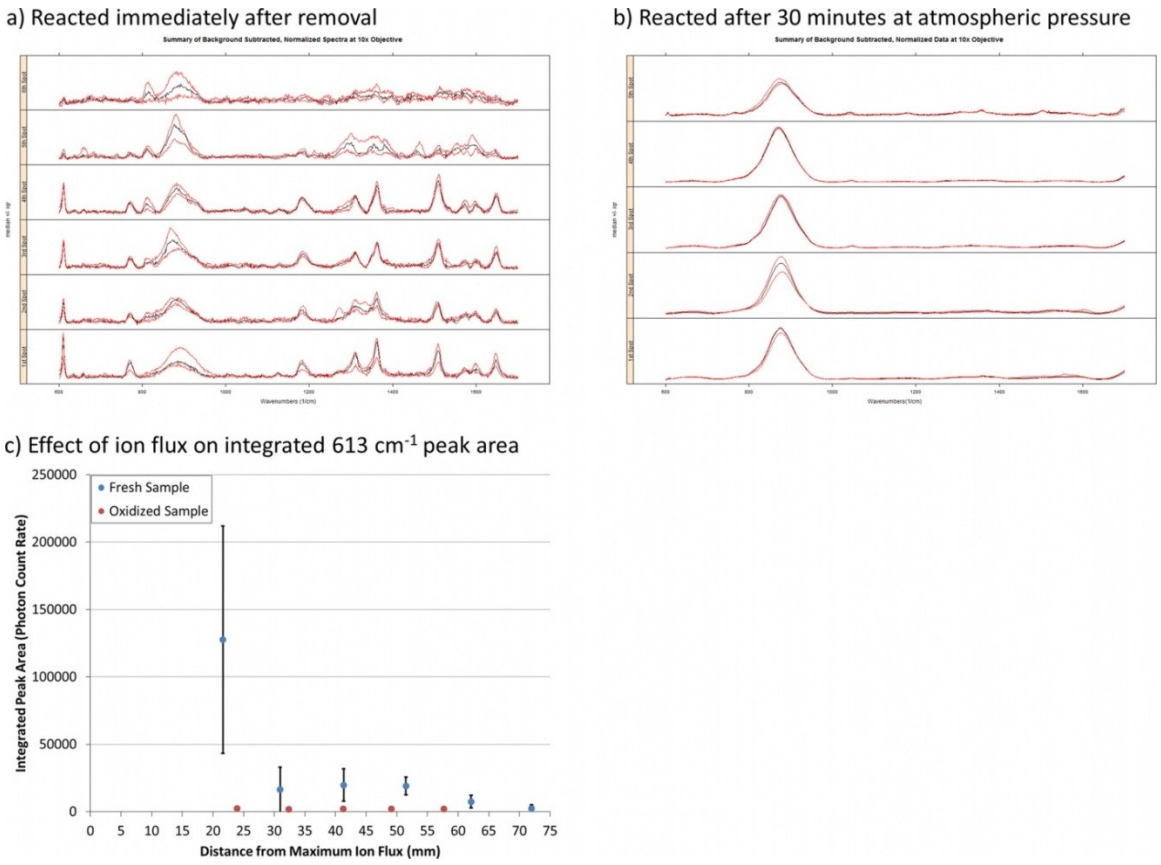

Figure 4-15. Central tendency and effect of distance from the point of maximum ion flux on the SERS of 1 µM R6G. a) Median and interquartile range of the normalized spectra from the slide reacted immediately after removal from the vacuum chamber. The point closest to the maximum ion flux is at the bottom of the figure. b) Median and interquartile range of the normalized spectra from the slide exposed to atmospheric oxygen for 30 minutes. The point closest to the maximum ion flux is at the bottom of the figure. c) Mean integrated peak area of the 613 cm^{-1} peak from 1 µM R6G as a function of distance from the point of maximum ion flux. Error bars represent 95% CI. The variability decreases with increasing distance from the maximum ion flux, while the enhancement drops initially but remains relatively constant up to a point.

reacted immediately shows stronger SERS activity, even at points far from the point of maximum ion flux. While some particles formed on the slide that was exposed to atmospheric oxygen, these particles did not contribute any appreciable surface enhancement at any point examined on the slide. Figure 4-15c shows the integrated peak area of the 613 cm^{-1} peak from R6G as a function of linear distance from the point of maximum ion flux. There is a distinct distance dependence for both the overall enhancement and the variability of the resulting spectra, as evidenced by the error bars (95% CI). More work is needed to validate and extend the findings of these experiments.

Conclusions

While galvanic displacement is known to produce effective SERS substrates for biochemical analysis, applications – particularly in biomedicine – have often been constrained by the use of harsh chemicals in forming the SERS substrates. This work shows that efficient Ag micro- and nanoscale SERS structures can be formed readily on Ni and Cu substrates using benign chemistries that facilitate nucleation of the galvanic reaction at specific sites, likely at defects in native oxide films that are soluble in these chemistries. By demonstrating this galvanic displacement-based SERS approach on everyday objects (coins) containing Ni and Cu, we underscore the easy application of the technique. Coupling such simple starting substrates to benign chemicals and relatively inexpensive portable Raman instruments, the results suggest broad field applications, particularly in remote regions.

SERS enhancements of order 10^9 are measured under non-resonant conditions for Rhodamine-6G, attributed to nanoscale Ag structures resulting from localized galvanic reactions. Additionally, we demonstrate that the approach can detect melamine in infant formula at a level of 5 ppm, which is above the current 1 ppm limit allowed in infant formula by both the US Food and Drug Administration and the World Health Organization, indicating a potential application in rapid screening of infant formula for clear melamine contamination. Melamine contamination is a global health concern: despite its health dangers, it has been illegally introduced into infant formula, pet food, and other foodstuffs to give the appearance of enhanced protein content in standard tests. While precise quantification of concentrations is difficult in any SERS technique, this work indicates that detection and semi-quantitative measures of melamine are possible with the simple galvanic reactions and everyday substrates employed here. Coupled with portable Raman instruments available at modest cost, this SERS technique is promising for applications in food safety, health, and other areas, potentially on a global scale.

Acknowledgments

I gratefully acknowledge the assistance of Yi Cheng, Omar Bekdash, Susan B. Buckhout-White, Alexander C. Kozen, Marshall A. Schroeder, Wei W. Yu, Ian M. White, and Gary W. Rubloff for this portion of my dissertation work. This research was supported by the Robert W. Deutsch Foundation and the NSF-EFRI grant NSFSC03524414. Metal evaporation and photolithography were performed in the Maryland NanoCenter (except for the proof-of-concept ALD experiments) and SEM images were acquired in the

NispLab. The NispLab is supported in part by the NSF as a MRSEC Shared Experimental Facility.

Chapter 5: SERS Detection of Bacterial Signaling Molecules Using Substrates Formed by Galvanic Displacement

Chapter Abstract

Bacteria communicate using several different signaling modalities, perhaps the best studied of which is small molecule mediated signaling. Small molecule mediated signaling influences a wide range of behaviors in bacteria, from motility and chemotaxis to biofilm formation and virulence factor production. Most methods to detect these small signaling molecules rely on cell-based systems to produce a fluorescent or luminescent response. Detecting small signaling molecules using a direct, label-free detection method such as SERS would be very beneficial to the field of cell signaling. Given their strong enhancement and simple fabrication, we used SERS substrates formed by galvanic displacement on several different surfaces (coins, metal tapes, and thin metal films) to detect three different small signaling molecules: autoinducer-2 (AI-2), indole, and *Pseudomonas* quinolone signal (PQS). AI-2 could be detected in pure solution at a concentration of 1 mM, approximately two orders of magnitude above the maximum levels found in the culture of wild type *E. coli*. Indole could be detected in pure solution at a concentration of 10 μM and 500 μM in M9 minimal medium. However, indole is not produced by bacteria in M9, so 500 μM indole was measured in 1× LB media. Due to the presence of tryptophan in LB, indole was unable to be distinguished from the background in a physiologically relevant medium. PQS could not be detected by SERS, although a Raman spectrum from a crystal of PQS was obtained. While galvanic displacement

produces SERS substrates with excellent enhancement properties for several molecules, such as Rhodamine-6G and melamine, this enhancement is not universally applicable to all analytes, possibly due to if or how the analytes interact with the substrates. Thus, these SERS substrates formed by galvanic displacement are not a viable method for the direct, label-free detection of small signaling molecules. It is worthwhile to emphasize that these conclusions are limited solely to the specific substrate and molecule combinations used in these experiments. Future work could include a more complete exploration of the parameter space or the use of other SERS substrates, such as silver or gold nanoparticles.

Introduction

Bacteria have evolved multiple methods for communication, including physical, chemical, and electrical signaling methods[126, 127]. These communication methods enable bacteria to adapt their metabolic activities based on the presence and quantity of other bacteria. Bacterial communication methods mediated by small molecules are among the best studied. A review by Ng and Bassler provides a good overview of the cell density dependent signaling phenomenon known as "quorum sensing"[128]. Quorum sensing behaviors influence a wide range of behaviors, from the formation of biofilms to the production of virulence factors to motility and bioluminescence. Accordingly, it represents an opportunity both to better understand bacterial physiology and to take advantage of the phenomenon to develop new methods to mitigate or prevent infection by pathogenic bacteria[35].

Quorum sensing is governed by small molecules called "autoinducers" that are traditionally grouped into three families: Autoinducer-1 (AI-1) is a family of acyl homoserine lactones (AHLs) that are species specific and used by Gram negative bacteria; Autoinducer-2 (AI-2) is a class of molecules derived from the molecule 4,5-dihydroxypentane-2,3-dione (DPD) and is used by both Gram positive and Gram negative bacteria; Autoinducing peptides (AIPs, sometimes called AI-3) are species specific and used by Gram positive bacteria. These three families of autoinducers do not encompass all quorum sensing mediators; *Pseudomonas aeruginosa* synthesizes another quorum sensing mediator called "*Pseudomonas* quinolone signal" or PQS that controls biofilm formation and virulence factor production.

Despite the ubiquity of intercellular signaling and the potential importance of these molecules in understanding microbiology and advancing medicine, there remains a lack of methods to detect these molecules. Reporter cells, utilizing fluorescence or bioluminescence, are far and away the most common method, although mass spectrometric methods have also been developed. FRET-based sensors have also been developed[129, 130]. Label-free methods to detect quorum sensing mediators remain limited to reports of the electrochemical detection of PQS[131] or pyocyanin as a proxy for AI-1[132] and another report of SERS of AI-1[133].

Autoinducer-2 (AI-2)

AI-2 is primarily synthesized from *S*-adenosyl homocysteine (SAH), a byproduct of *S*-adenosyl methionine demethylation. SAH is processed by an *S*-adenosylhomocysteine

hydrolase (Pfs in the case of *E. coli*) to form adenine and *S*-ribosyl homocysteine. *S*-ribosyl homocysteine is cleaved by an *S*-ribosylhomocysteine lyase (LuxS in the case of *E. coli*) to produce homocysteine and 4,5-dihydroxypentane-2,3-dione (DPD). DPD exists in a complex equilibrium with several other forms in the presence of water[134], creating the family of molecules known as AI-2. When in the presence of significant borate concentrations, as in the ocean, DPD reacts with borate to form a borodiester that is used by the *Vibrio* genus of marine bacteria.

AI-2 is brought into the cell by a transporter protein complex composed of the proteins LsrA, LsrB, LsrC, and LsrD in *E. coli*. LsrB has been identified as the transport protein for AI-2[135], and is highly selective for DPD over the borodiester form of DPD[130]. Inside the cell, AI-2 is phosphorylated by LsrK, which can then bind to the transcription repressor LsrR, enabling transcription of genes downstream of an LsrR binding site. In the *Vibrio* genus, AI-2 is not brought directly into the cell but instead binds to a receptor (LuxP) that is part of a complex (LuxPQ). This leads to a signal transduction by a phosphorylation/dephosphorylation cascade (depending on AI-2 concentration), which leads to the production of LuxR, a transcription factor necessary for the increased transcription of genes under the control of a lux box consensus sequence. As with LsrB, LuxP has been demonstrated to be highly selective for the borodiester form of AI-2, and does not bind DPD[129].

Pseudomonas quinolone signal (PQS)

PQS is the name given to the molecule 2-heptyl-3-hydroxy-4-quinolone, produced by *Pseudomonas aeruginosa*. PQS is biosynthesized from anthranilic acid, which is derived from either shikimic acid or tryptophan by different metabolic pathways[136]. The enzymes PqsA, PqsB, PqsC, and PqsD convert anthranilic acid to 2-heptyl-4-quinolone (HHQ), a precursor for PQS. HHQ has intercellular signaling properties itself. The enzyme PqsH converts HHQ into PQS. Due to the highly hydrophobic nature of its structure, PQS is transferred between cells in membrane bound vesicles[137].

Production of PQS is modulated by the two AI-1 based quorum sensing circuits present in *P. aeruginosa*. In turn, PQS modulates the production of siderophores for regulating Fe^{3+} acquisition and metabolism, as well as the production of virulence factors like pyocyanin, elastase, proteases, and surfactants[138]. As a quinolone, PQS is electrochemically active, and has previously been detected by electrochemical methods[131]. PQS was selected for study by SERS due to the aromatic nature of the quinolone moiety and the presence of an alkyl tail, both of which are often observable under Raman and SERS, in addition to the potential healthcare applications of being able to detect PQS in a real time, label free manner.

Indole

Quroum sensing, while a very important bacterial signaling behavior, is not the only small molecule mediated signaling mechanism used by bacteria. Indole is another small molecule produced by bacteria that can alter the behavior of nearby bacteria[139] and

even mammalian cells[140]. Indole is generally not regarded as being a quorum sensing mediator, although that is still debated within the literature. Indole is synthesized from tryptophan via a tryptophanase (TnaA in *E. coli*), beginning late in the exponential phase and is produced throughout the stationary phase. Indole can be produced at levels up to 0.6 mM in rich media. Indole production is sensitive to local environmental conditions such as pH and temperature[141].

Indole is produced by over 85 different bacterial species and has many effects as an intercellular signaling molecule. In co-culture with *Pseudomonas aeruginosa*, indole provides a competitive advantage to *E. coli* by inhibiting quorum sensing by *P. aeruginosa*[142]. Additional effects include spore formation, changes to biofilm formation, virulence factor production or inhibition, increased drug/antibiotic resistance, and formation of bacterial persisters[140, 143]. The differing responses to indole among the bacteria that use and sense indole reflect the complexity of bacterial interspecies interactions. Although much of the Raman and SERS work surrounding indole have focused on derivatives of indole being important in mammals (e.g., tryptophan, serotonin) and plants (e.g., auxins), there are reports of SERS and Raman of indole, as well as accompanying density functional theory (DFT) calculations of the spectra[144].

Experimental

Reagents

$AgNO_3$ (ACS grade) and aluminum shot (99.999%) were obtained from Alfa Aesar. $HAuCl_4$ (99.999% trace metal basis), indole (≥99%), and 2-heptyl-3-hydroxy-4(1*H*)-

quinolone (PQS, ≥96%, HPLC) were obtained from Sigma-Aldrich. LB media was obtained from Fischer Scientific. Azure Hi-Def media was obtained from Teknova. Copper and aluminum tapes (3M) were obtained from McMaster-Carr. M9 minimal media was made according to a standard protocol[32] using reagents from Sigma Aldrich. AI-2 and analogues were synthesized according to previously published methods[33-35].

SERS substrate fabrication

SERS substrates were formed on coins, thin aluminum films, and metal tapes. The coins, U.S. pennies from circulation, were ultrasonicated for 15 minutes in deionized H_2O, rinsed with 70% isopropanol, rinsed with deionized water, and dried under flowing air. The substrates were formed by galvanic displacement using 50 mM $AgNO_3$ placed on the coin surface for 30 minutes in the dark, followed by removal of the $AgNO_3$ and rinsing the reacted surface with two volumes of deionized water before drying under flowing air.

Substrates formed on Al or Cu tape were formed using a similar method- first the tape surfaces were washed with acetone, followed by 70% isopropanol, and then deionized water before being dried under flowing air. 80 μL of deionized water was placed on each metal circle to be reacted, and 20 μL of 50 mM of either $AgNO_3$ or $HAuCl_4$ was added to the deionized water and allowed to react in the dark for 30 minutes before removing the solution, rinsing with two volumes of deionized water, and drying under flowing air.

For the SERS of indole, aluminum films of 100 nm thickness were formed by thermal evaporation of aluminum onto standard glass microscope slides cleaned by piranha solution (3:1 H_2SO_4:H_2O_2). Thermal evaporation was performed using a Metra thermal evaporator. The slides were then patterned using standard photolithography techniques, exposing circles of metal 8 mm in diameter using SU-8 photoresist (Microchem). 80 μL of deionized water or 100 mM NaOH was placed on each metal circle to be reacted, and 20 μL of 50 mM of either $AgNO_3$ or $HAuCl_4$ was added to the deionized water and allowed to react in the dark for 30 minutes before removing the solution, rinsing with two volumes of deionized water, and drying under flowing air. The morphology of these substrates were examined by scanning electron microscopy using a Hitachi SU-70 scanning electron microscope at an accelerating voltage of 10keV. As a reference, SERS of indole on the galvanic displacement substrates was compared against SERS of indole on a commercially available SERS substrate, Klarite (Renishaw Diagnostics).

SERS parameters

20 μL of the analyte at the indicated concentration was added to the surface of the substrate and allowed to dry in air. Raman spectra were obtained at 50x magnification using a Horiba Jobin-Yvon LabRamHR-800 system using the internal HeNe laser with a wavelength of 632.8 nm and spectra were acquired over the range of 600 cm^{-1} to 1700 cm^{-1} unless otherwise indicated. LabSpec software (v. 5.25.15, Horiba) was used to

control the instrument, acquire spectra, perform background subtraction, and analyze the spectra.

AI-2 and derivative spectra represent an average of five points with an integration time of 900 seconds per point (300 three second integrations averaged per point). Indole spectra represent an average of five points with an integration time of 30 seconds per point (30 one second integrations averaged for each point). PQS spectra represent an average of five points with an integration time of 900 seconds per point (300 three second integrations averaged per point). These times were selected after varying acquisition parameters and integration times to obtain the best possible signal to noise ratios.

Additional analysis of SERS spectra was performed using the ChemoSpec chemometrics package version 1.61-3[95], in the R statistical programming environment, version 3.0.1[96]. This includes principal component analysis (PCA), hierarchical clustering analysis (HCA), and measures of central tendency.

Results and discussion

SERS of AI-2 and analogues

Given the prevalence of AI-2 as a signaling molecule in the bacterial world, it represents a prime candidate for label-free direct detection methods. We acquired SERS spectra from 10 mM chemically-synthesized AI-2 on a SERS substrate formed by galvanic displacement on a penny by Ag. This represents the first reported SERS detection of AI-2, shown in Figure 5-1. We were able to detect AI-2 at 10 mM and 1 mM in pure

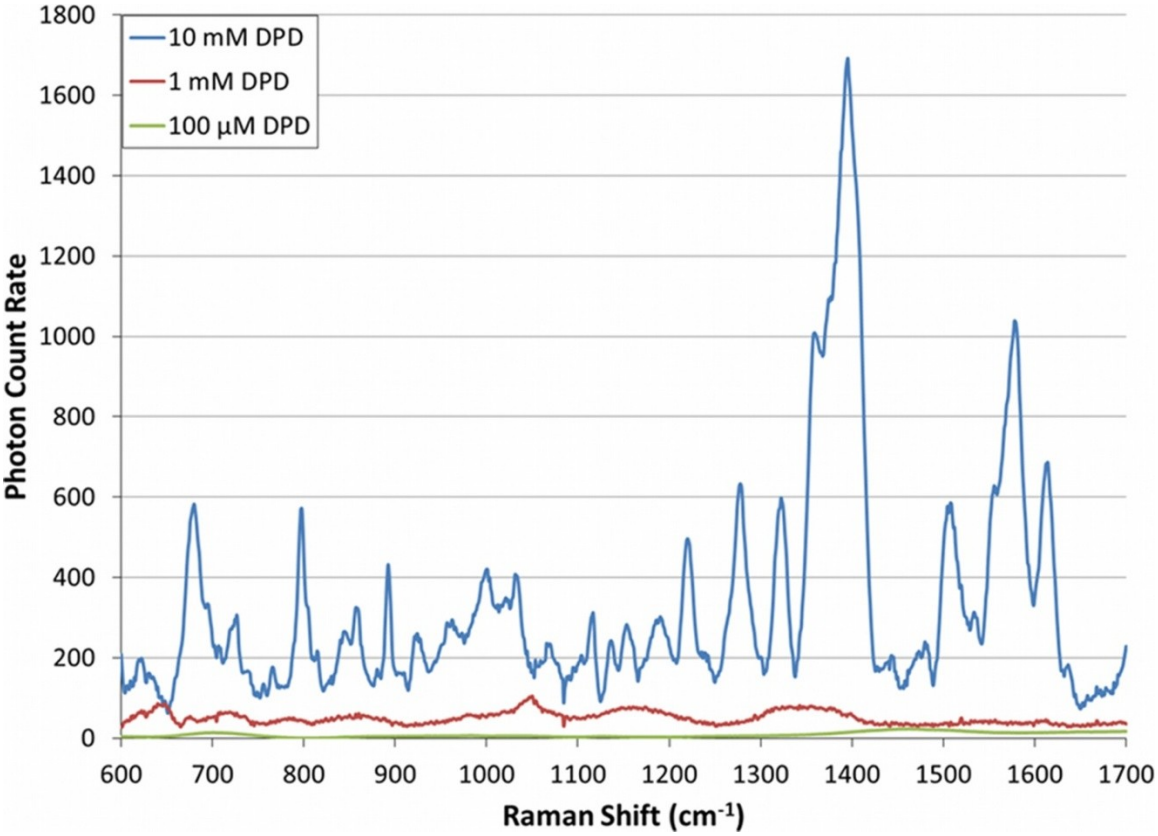

Figure 5-1. SERS spectra of chemically synthesized DPD (AI-2). At 10 mM, DPD shows a feature-rich spectrum. Many of the features disappear at a concentration of 1 mM, but it still retains features (e.g., the broad peak between 1300 and 1400 cm^{-1} possibly due to band broadening of the relatively intense peaks located in that range for the 10 mM concentration). At 100 µM, the spectrum is effectively featureless. This limit of detection around 10 mM is between two and four orders of magnitude above concentrations of AI-2 produced in laboratory cultured wild type strains of *E. coli* such as W3110. Spectra are offset for clarity.

solution, however, concentrations below 1 mM in H_2O were indistinguishable from background. When AI-2 was present in a complex mixture (Figure 5-2), such as LB, M9, Teknova's Hi-Def Azure defined media, it was indistinguishable from the background signal contributed by the media. The AI-2 spectrum is complex and rich in spectral features- this may be a result of the complex equilibrium that AI-2 exhibits in the presence of water[134].

Figure 5-3 shows AI-2 spectra obtained using substrates formed by galvanic displacement of an Al thin film, as well as a different excitation wavelength, provided by a 784 nm diode laser. None of them produced appreciable improvement over the Ag on penny substrates. The Ag on Al thin film yielded high count rates, but this led to the loss of some spectral information due to the overlapping of peaks. While the parameter space for the galvanic displacement reaction was not completely explored, the data obtained thus far indicate that galvanic displacement is not an ideal method for producing substrates to detect AI-2 by SERS.

While AI-2 itself does not scatter well on the galvanic displacement substrates, we reasoned that aromatic analogues of AI-2 might be easier to detect than the parent molecule itself using SERS. The aromatic AI-2 analogues 1-(furan-2-yl)-3,4-dihydroxybutane-1,2-dione (furanyl-DPD), 1-(4-fluorophenyl)-3,4-dihydroxybutane-1,2dione (fluorophenyl-DPD), and 3,4-dihydroxy-1-(4-nitrophenyl)butane-1,2-dione (nitrophenyl-DPD), whose structures are shown in Figure 5-4, were examined on Ag-penny SERS substrates. The resulting spectra are shown in Figure 5-5. Principal component analysis (PCA) failed to reliably distinguish between the spectra for different

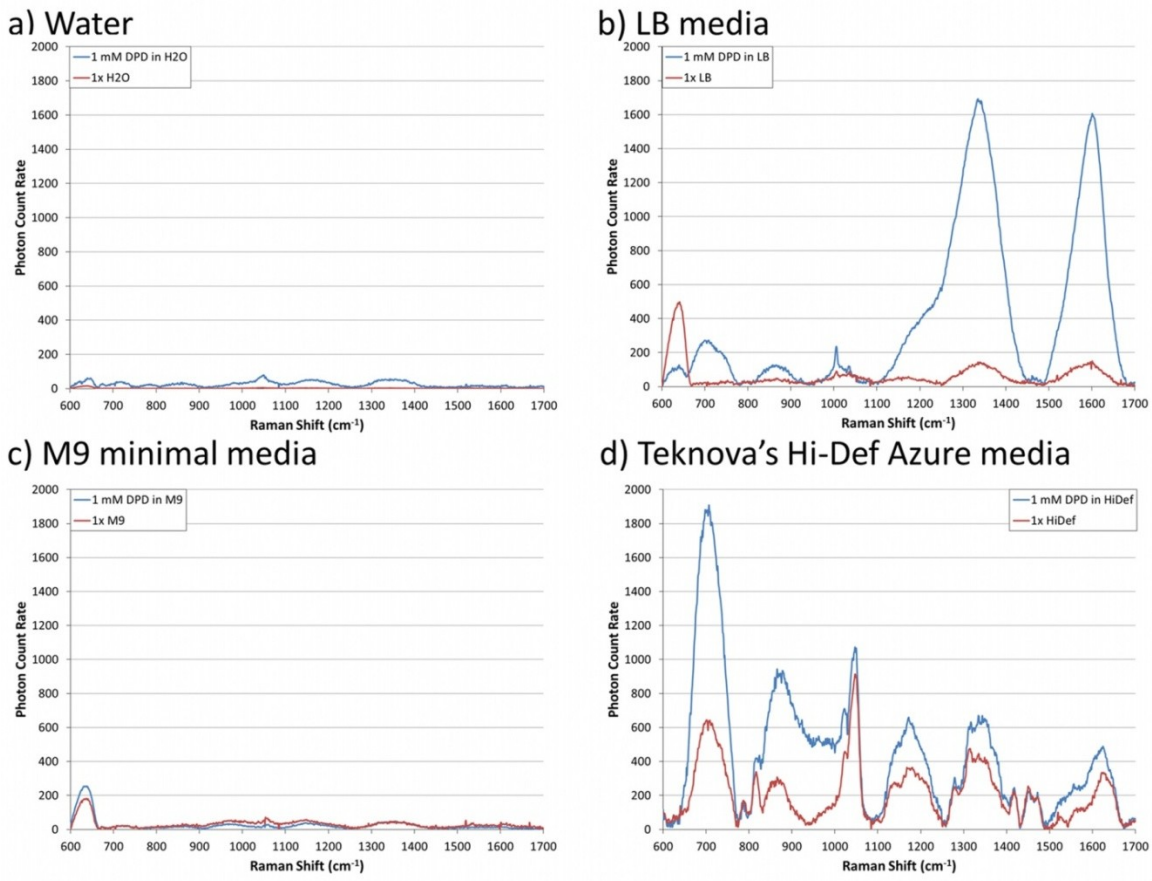

Figure 5-2. Comparison of 1 mM DPD in various media. All four graphs are on the same scale. a) 1 mM DPD in H_2O. As seen in Figure 5-1b, 1 mM DPD can be identified in H_2O. b) 1 mM DPD in LB media. While there are differences in the absolute intensities of some of the peaks, none of these are uniquely identifying for DPD, and are attributed to local variations in the composition of LB media. c) 1 mM DPD in M9 minimal media. Minimal media has very few components that should scatter (primarily glucose), but DPD cannot be distinguished from the background. d) 1 mM DPD in Teknova's Hi-Def Azure chemically defined medium. Hi-Def contains many components that contribute significantly to the background, eliminating any possibility of distinguishing DPD unambiguously.

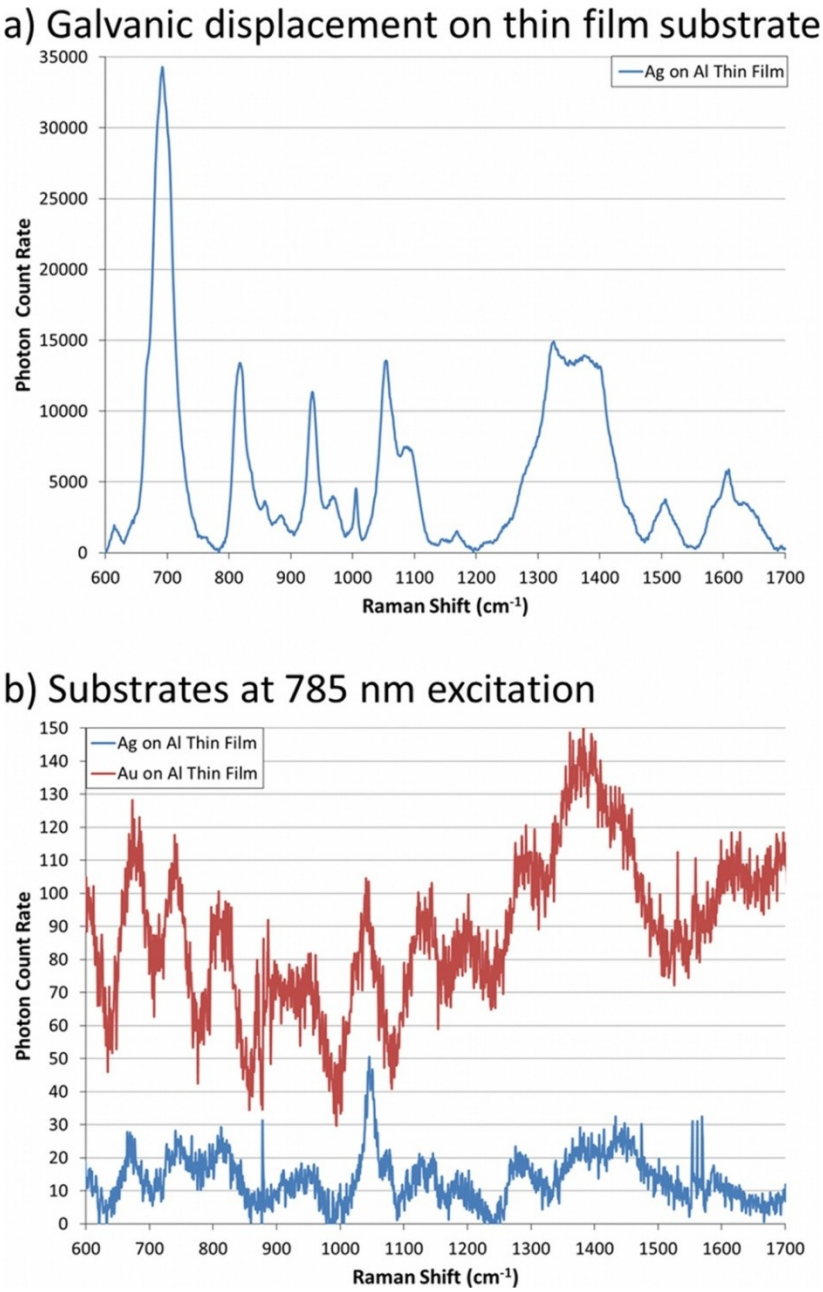

Figure 5-3. 10 mM DPD in H_2O with different substrates and excitation wavelengths. a) DPD on a SERS substrate formed by galvanic displacement of an Al thin film by Ag. b) DPD on SERS substrates formed by galvanic displacement of an Al thin film by Ag or Au under the excitation of a 784 nm laser. Due to the different geometry of the substrates, the spectra look somewhat different than that in Figure 5-1, but retain several similar features.

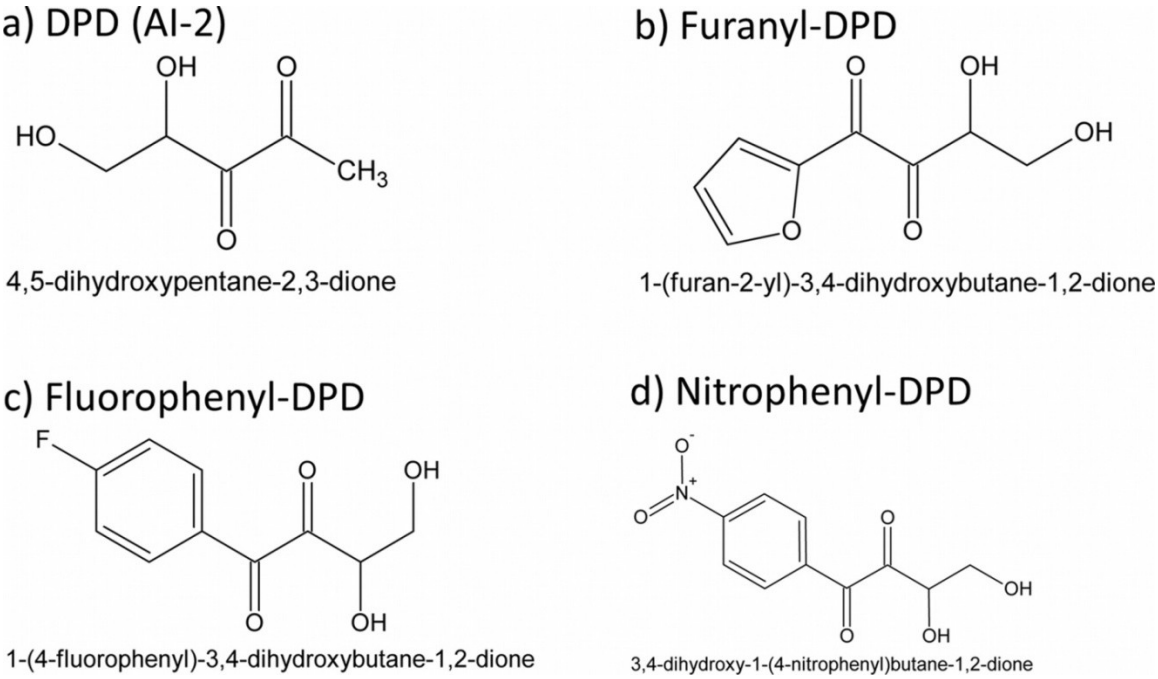

Figure 5-4. Structure of DPD (AI-2) and the aromatic analogues used in this study. The abbreviated names are given in addition to the IUPAC names.

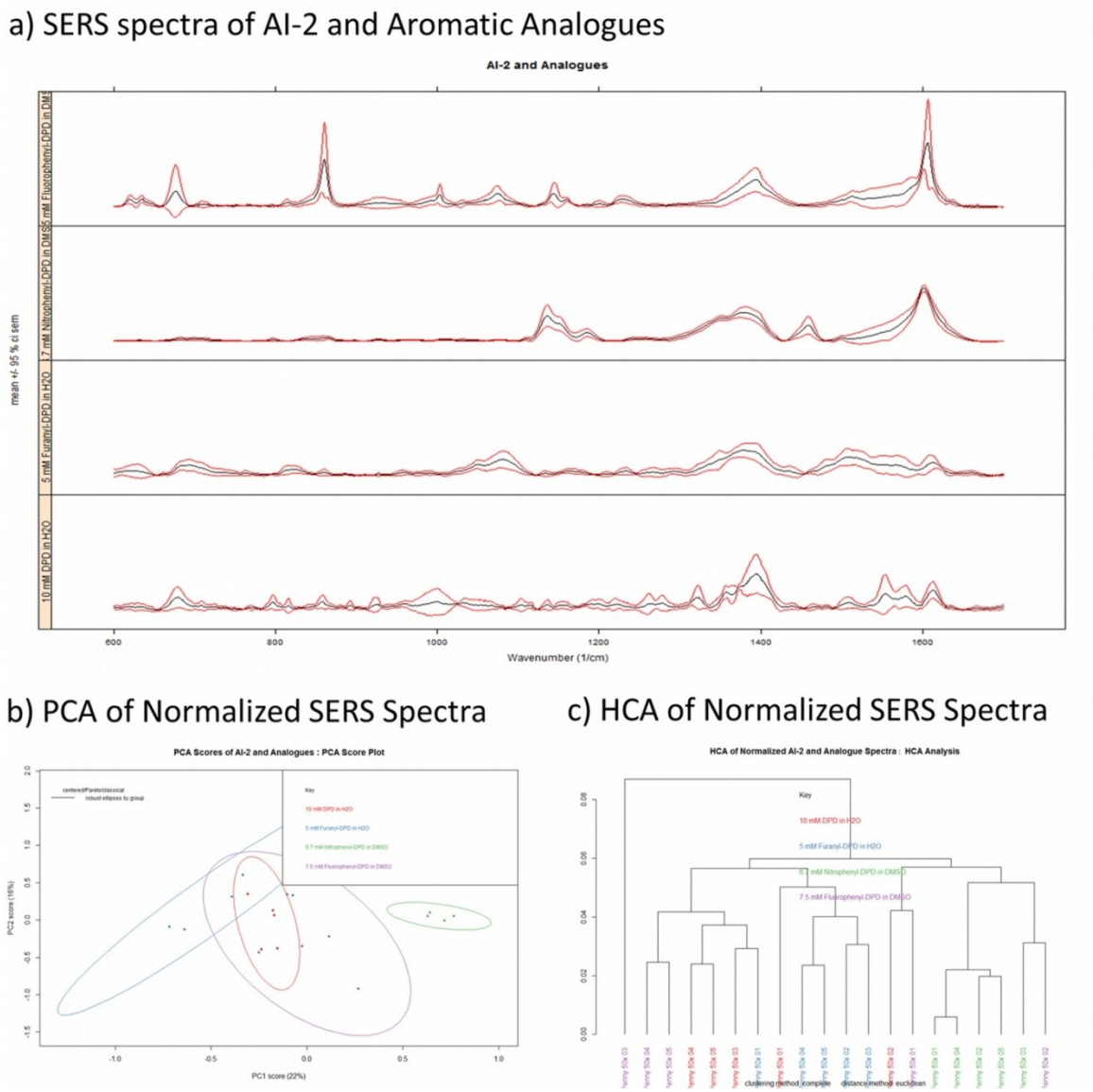

Figure 5-5. SERS and analysis of aromatic analogues of AI-2. a) SERS spectra of 10 mM DPD in H_2O, 5 mM Furanyl-DPD in H_2O, 6.7 mM Nitrophenyl-DPD in DMSO, and 7.5 mM Fluorophenyl-DPD in DMSO (from bottom to top). b) Classical principal component analysis of the normalized spectra, using Pareto weighting and with 95% CI ellipses around the groups. c) Hierarchical clustering analysis of the normalized spectra. Nitrophenyl-DPD clusters together, with the addition of a Fluorophenyl-DPD spectrum, possibly due to the presence of DMSO.

molecules at the 95% CI level (Figure 5-5b), and hierarchical clustering analysis (HCA) does not accurately classify the spectra (Figure 5-5c). The solutions containing DMSO as a solvent for the AI-2 analogues (fluorophenyl-DPD and nitrophenyl-DPD) showed marginally better discrimination in PCA and clustering with HCA, although this is possibly due to the presence of DMSO, since the nitrophenyl-DPD lacks appreciable peaks characteristic of nitrobenzene[145].

SERS of PQS

We anticipated that PQS, with the aromatic quinolone moiety and seven carbon alkyl tail, would yield a feature-rich SERS spectrum and possibly enable *in situ* detection of the molecule. The normal Raman spectrum of the molecule, shown in Figure 5-6, shows a variety of strong peaks in the fingerprint region. However, once dissolved in methanol and placed on an Ag-penny SERS substrate, the results were underwhelming. Figure 5-6 also shows the SERS spectrum of 1 mM PQS in methanol, dried on the substrate. There are no readily apparent characteristic peaks- the peaks are all broad and have very low photon count rates. When superimposed on one another, the peaks do line up somewhat, which implies that while there is some Raman scattering going on, the galvanic displacement substrates used are not ideal for SERS of PQS. This is highly unexpected, and warrants further investigation.

SERS of indole

The SERS of indole was investigated in water, M9 minimal media, and LB media using SERS substrates formed by galvanic displacement of Al thin films by Ag or Au.

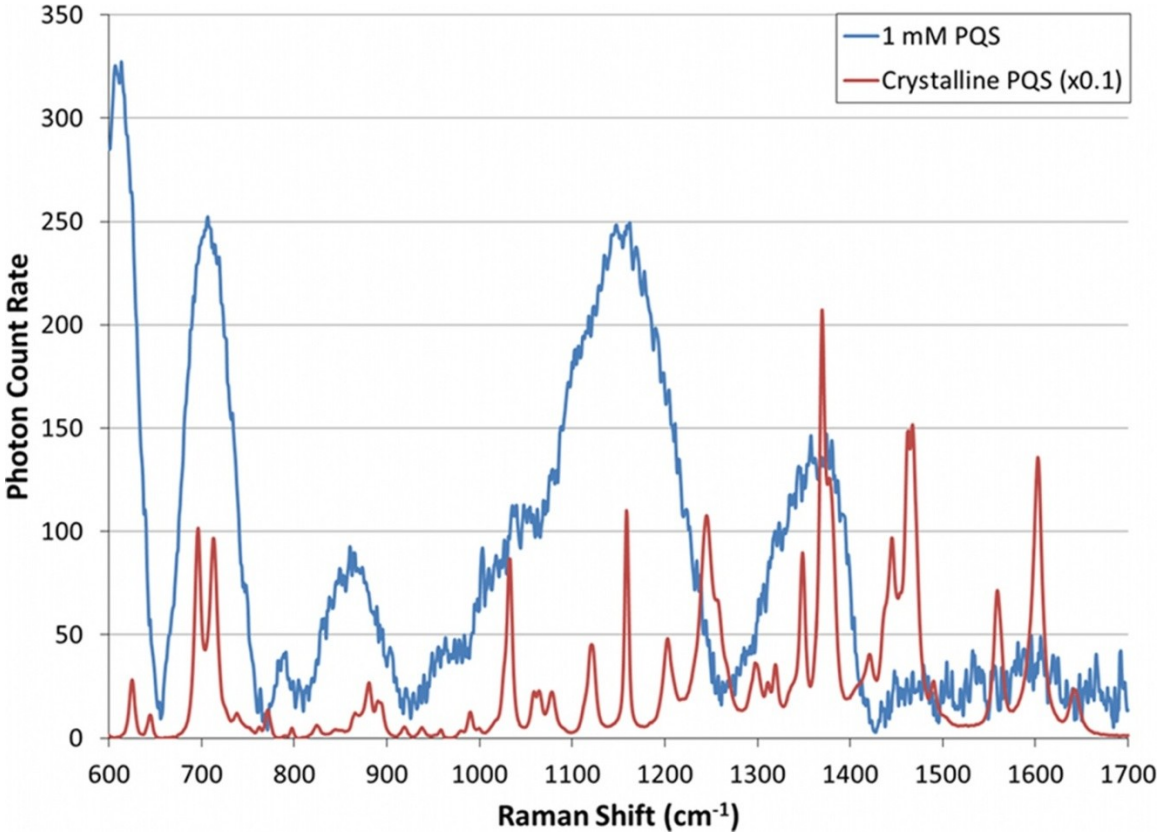

Figure 5-6. Comparison of the SERS of 1 mM PQS in methanol on an Ag on penny SERS substrate formed by galvanic displacement with a scaled version of the normal Raman spectrum of crystalline PQS. There are no uniquely identifying peaks present in the SERS spectrum, the peaks present are very broad, and the photon count rates are very low. This is highly unexpected, given the prominence of several peaks in the normal Raman spectrum of PQS.

Representative scanning electron micrographs of the substrate morphologies is shown in Figure 5-7. The difference in the resulting substrate morphology as a function of both the oxidizing agent (Ag^{+} or Au^{3+}) and the pH of the solution (with or without 100 mM NaOH) underscores the importance of these (and other) reaction parameters in the galvanic displacement reaction. Indeed, substrates formed by $AgNO_3$ alone were not able to adequately enhance indole solutions; subsequently, their results are not discussed here. Substrates formed by Au fared better than those formed by Ag, possibly due to the high density of dendritic structures that form creating a higher local density of tips and branch points that are believed to lead to high SERS enhancement.

Figure 5-8 shows a limit of detection study of indole in H_2O on an Au in NaOH substrate. Indole can be detected down to 10 μM in pure solution. However, detecting an analyte in pure solution serves little purpose when the ultimate goal is to detect molecules *in situ*- they must be detected in a biological medium. Figure 5-9 shows the detection of 500 μM indole in M9 minimal medium on Au in NaOH substrates (Figure 5-9a) and a comparison with Klarite, a commercially available SERS substrate (Figure 5-9b). Klarite produces no appreciable enhancement of indole at either 500 μM in M9 or 1 mM in pure solution. In rich media, indole is produced at concentrations up to 600 μM[140]; however M9 is a minimal medium and does not provide an accurate comparison.

Figure 5-10 shows the detection of 500 μM indole in LB media. Peaks at 900 cm^{-1} and 1160 cm^{-1} appear to be more prominent in the LB containing 500 μM indole relative to those in LB alone. The results of the detection are inconclusive, as LB media contains tryptophan, whose side chain is an indole moiety. The presence of an indole moiety in the

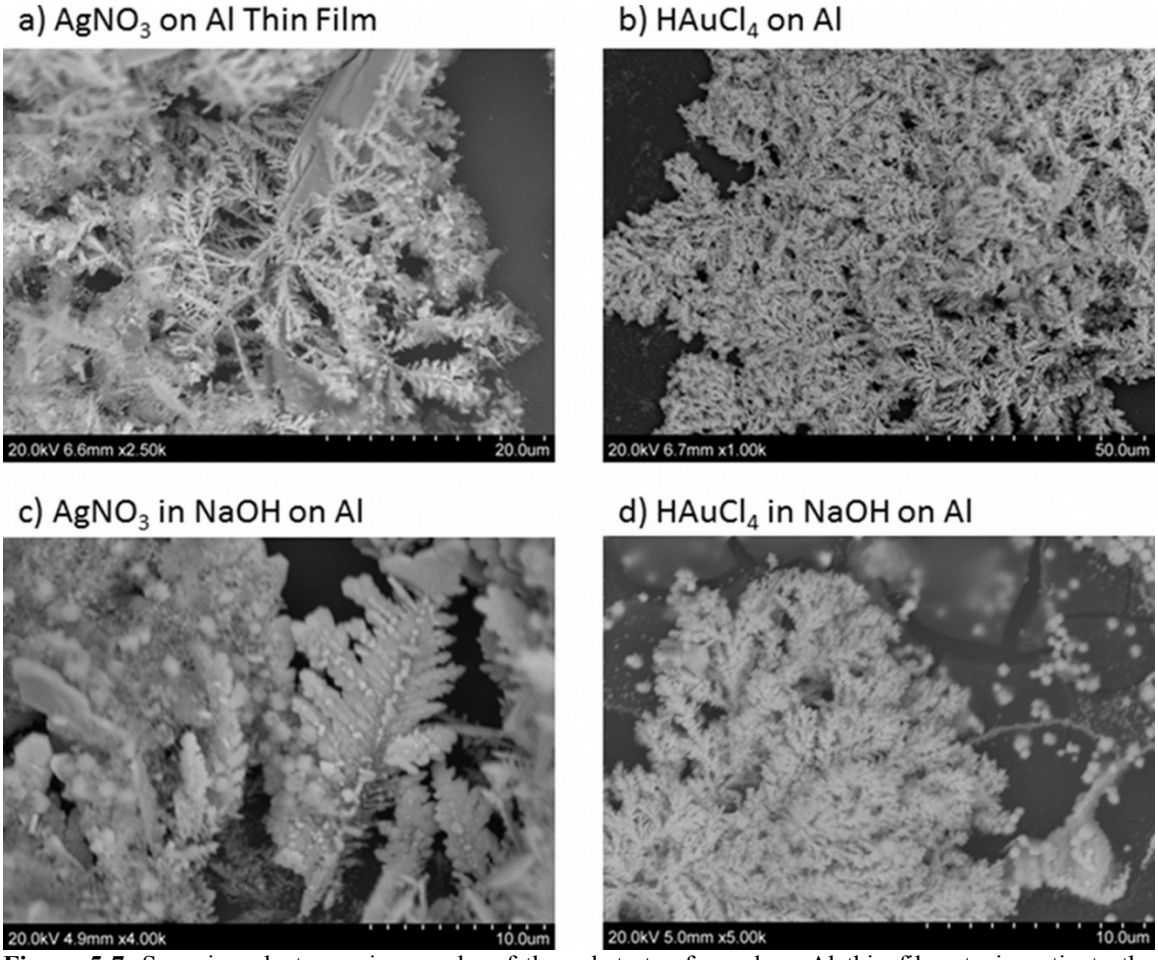

Figure 5-7. Scanning electron micrographs of the substrates formed on Al thin films to investigate the SERS of indole. a) 50 mM $AgNO_3$ forms dendrites similar to those observed in the previous chapter. b) 50 mM $HAuCl_4$ forms smaller, more densely-packed dendrites. c) 50 mM $AgNO_3$ in 100 mM NaOH forms much broader and flatter dendritic structures. d) 50 mM $HAuCl_4$ in 100 mM NaOH forms dendrites similar to those observed for 50 mM $HAuCl_4$ by itself, but with the addition of several smaller satellite particles.

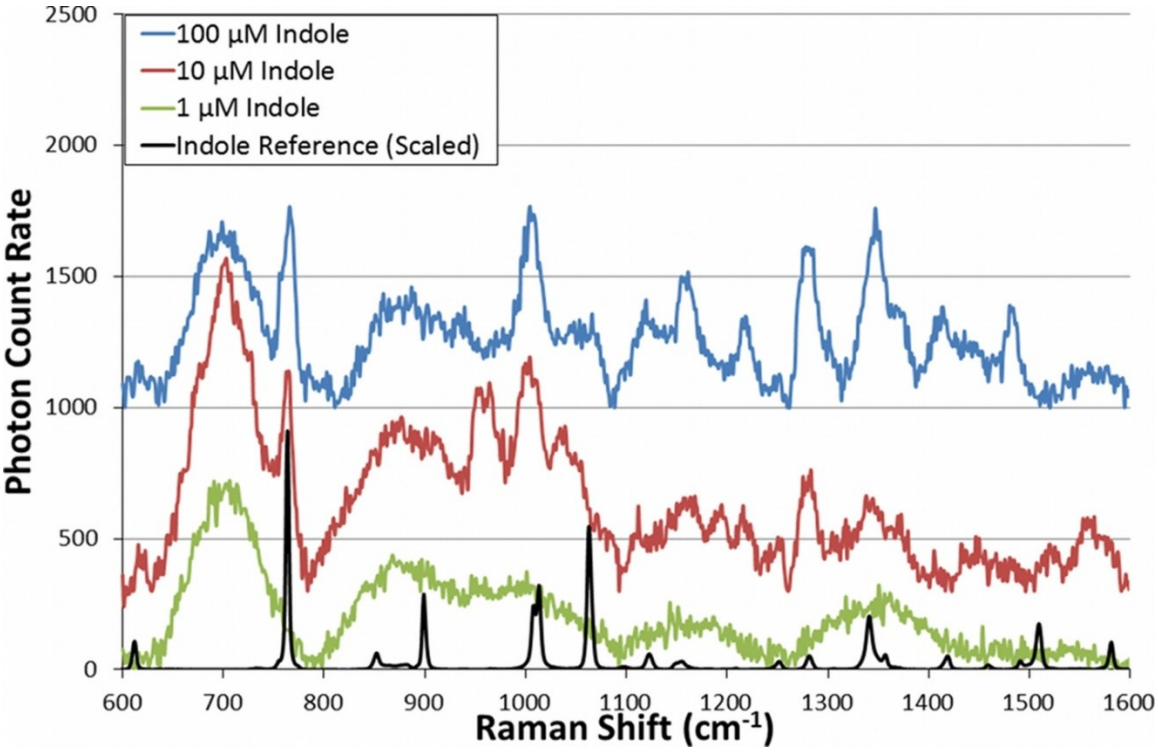

Figure 5-8. Limit of detection of indole in H_2O on Au substrate formed on Al thin film. The limit of detection was determined to be on the order of 10 µM, as the ring breathing mode (760 cm^{-1}) and several other vibrational modes are clearly visible at the 10 µM concentration level but not at the 1 µM level.

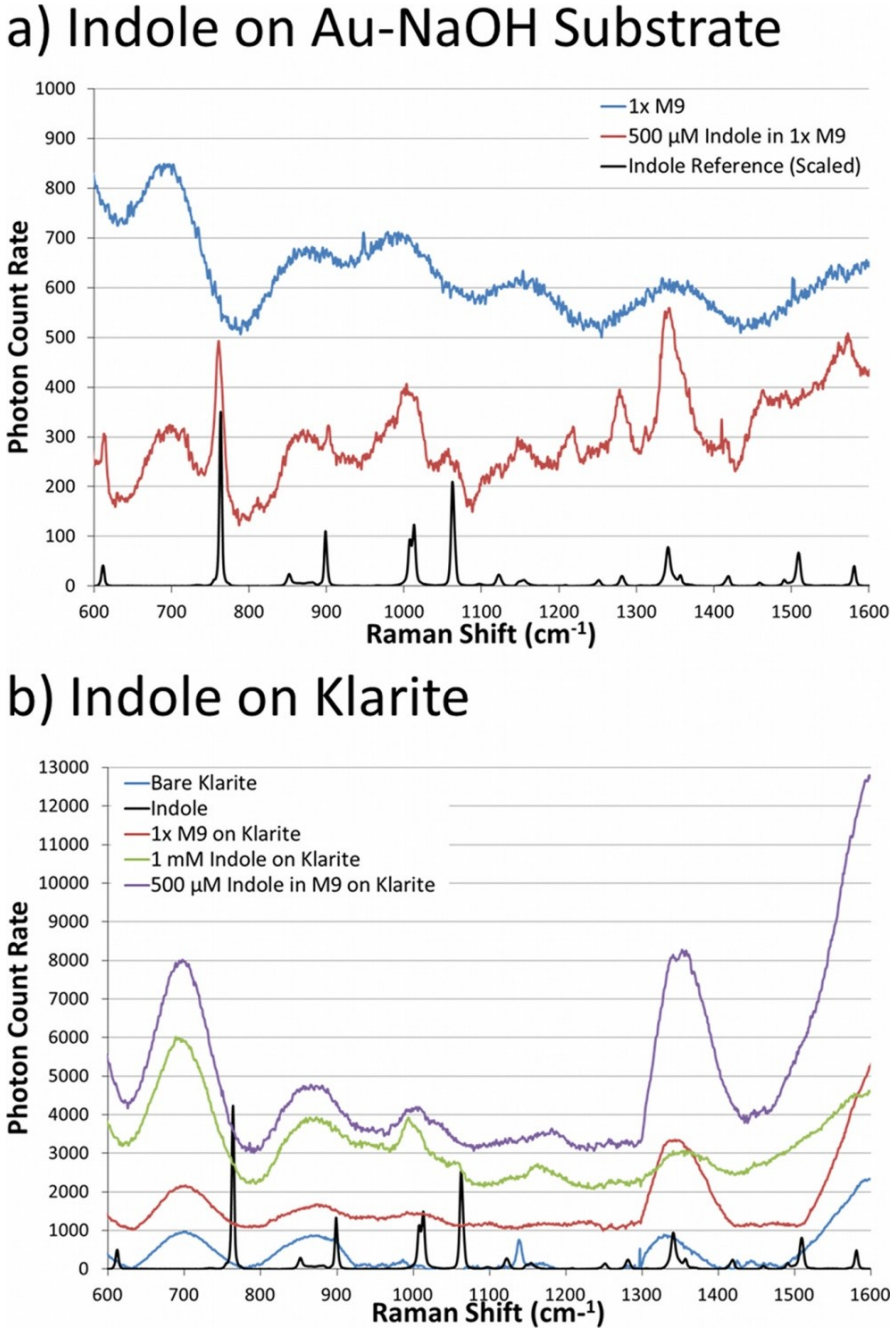

Figure 5-9. Indole detection in M9 minimal media. a) SERS substrates formed by galvanic displacement of an Al thin film by 50 mM $HAuCl_4$ in 100 mM NaOH. 500 µM Indole in M9 can be detected using these substrates. b) Klarite, a commercially available SERS substrate, is ineffective at enhancing indole in either H_2O at 1 mM or in M9 at 500 µM.

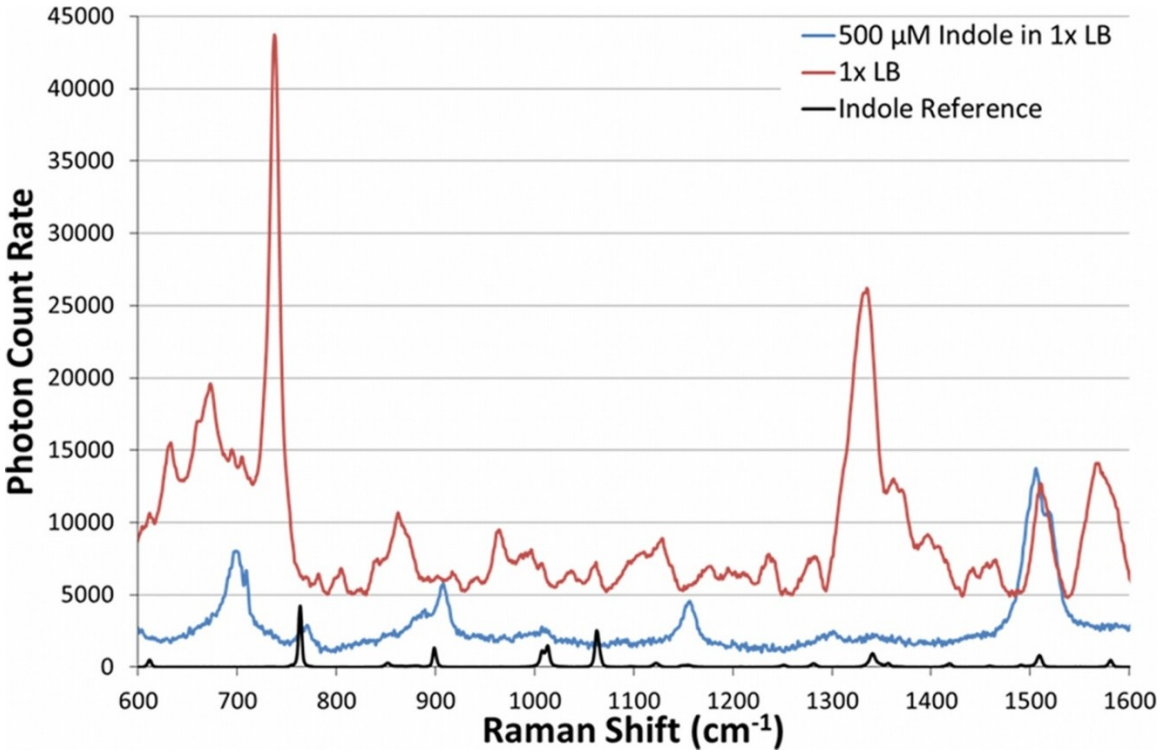

Figure 5-10. Indole in LB on a SERS substrate formed by galvanic displacement of an Al thin film by 50 mM $AgNO_3$ in 100 mM NaOH. While certain peaks seem to be more prominent in the 500 µM indole in LB spectrum, especially the 900 cm^{-1} and 1160 cm^{-1} peaks, the heterogeneity of LB media and the presence of tryptophan (whose side chain is an indole moiety) in LB makes reliably distinguishing indole from the background difficult at best, even at high concentrations.

medium, combined with the lack of a defined media composition render a definitive detection optimistic at best.

Future work

The parameter space for the galvanic displacement reaction is immense. It is conceivable that some combination of reactants, surface topology, and oxide defect density could produce a SERS substrate capable of enhancing AI-2 and other signaling molecules. However, the amount of work necessary to conduct such a search may not be worth the effort. It is also entirely possible that the physicochemical properties of the signaling molecules investigated here are such that they will not interact with the substrates in such a way that provides surface enhancement. Capping agents, such as thiols with additional functionalities (e.g., a borate group to react with AI-2, forming the borodiester AI-2), may enable close interaction with the surface, giving rise to SERS of the signaling molecules. There is a single previous report of SERS of the AI-1 family of autoinducers[133] that made use of Lee and Meisel citrate-reduced Ag colloids[146] with no capping agent. Using other more popular and well-characterized SERS substrates such as these may prove more fruitful than a search of a parameter space that grows with combinatorial complexity.

Density Functional Theory (DFT) calculations could be employed to assign vibrations observed in the 10 mM AI-2 and crystalline PQS spectra. It is likely that the AI-2 spectrum obtained earlier is a composite of the spectra of the individual molecules that make up the complex equilibrium that AI-2 exhibits, and as such, the DFT of AI-2 is

a nontrivial endeavor. However, it would be interesting to see whether some linear combination of the spectra obtained from DFT correspond with the equilibrium ratios of the individual components of the equilibrium. Given the crystalline nature of PQS as obtained from Sigma-Aldrich, the DFT of this molecule may be much more straightforward.

Perhaps a better approach would be to develop a biosensor based on the AI-2 receptor protein LsrB. FRET-based LuxP sensors have been reported for the borodiester form of AI-2 previously, but LsrB, a structural homologue of LuxP, did not exhibit a strong enough FRET effect to serve as an effective biosensor[129, 130]. Since AI-2 does not exhibit efficient inelastic scattering or present any strong characteristic peaks, perhaps a refractive index sensor based on localized surface plasmon resonance or spectroscopic ellipsometry or a mass-based sensor such as a functionalized quartz crystal microbalance may be able to provide a quantitative measure of AI-2 present in a sample.

Conclusions

SERS substrates formed by galvanic displacement are not an effective way to detect AI-2 or PQS in a label-free fashion. SERS substrates formed by galvanic displacement of aluminum by gold are capable of detecting indole in M9 minimal medium at a concentration of 1 mM, but not below that and not in a relevant medium where indole is produced (e.g., LB media). While not an exhaustive characterization, exploration of the parameter space of galvanic displacement may lead to the discovery of a set of reaction conditions that enable the detection of these molecules. Alternatively, other SERS

substrates such as nanoparticles or nanosphere lithography can be explored to see if they possess the proper physical and chemical characteristics to produce SERS of these signaling molecules.

Acknowledgments

I gratefully acknowledge the incredible amount of assistance I received from Min Guo and Herman O. Sintim for the synthesis of DPD and the AI-2 analogues. I also gratefully acknowledge additional assistance from Varnika Roy, Yi Cheng, Chen-Yu Tsao, William E. Bentley, and Gary W. Rubloff for this portion of my dissertation work. This research was supported by the Robert W. Deutsch Foundation. Metal evaporation and photolithography were performed in the Maryland NanoCenter and SEM images were acquired in the NispLab. The NispLab is supported in part by the NSF as a MRSEC Shared Experimental Facility.

Chapter 6: Summary and Conclusions

This dissertation details our work in the development of new sensing modalities for bacterial and environmental interactions. The work has currently generated two published papers, an invited paper currently in revision, an additional paper in preparation, and 11 conference presentations. In this chapter, I will briefly summarize the findings of each chapter, discuss the significance and innovation of each chapter, and then highlight future directions for work.

Optically clear calcium alginate hydrogels

Given the importance of optical and fluorescent microscopies in understanding biological systems and their interactions with their environments, we sought to improve the ability of researchers to immobilize cells at a desired point in space and time and be able to image the entire population of cells entrapped within the hydrogel using confocal microscopy. Furthermore, this aligns well with the ongoing research in the Maryland Biochip Collaborative, which exploits the ability to assemble populations of cells in alginate in a desired spatial relation to one another in order to better understand intercellular signaling phenomena.

Significance

The ability to control where and when a population of cells is placed is a very powerful tool for research, and accordingly has been essential to our work in the Maryland Biochip collaborative. This work extends the significance of this already powerful technique by providing a more complete, more accurate overview of cell growth and behavior due to

the optically clear gels employed in this technique. By removing the need for $CaCO_3$ particles throughout the entire hydrogel, researchers are able to monitor population and cell-scale behaviors in a more quantitative fashion.

Innovation

The use of a two-step bilayer geometry of alginate hydrogels in which the first layer contains $CaCO_3$ particles to provide free Ca^{2+} to gel a clear, second hydrogel layer is a first for this work. The creation of an optically clear alginate gel using only an electrical signal (obviating the need for an acidic rinse to dissolve excess $CaCO_3$ particles) is yet another first. Additionally, this work was the first to show a standard bacterial growth curve within the clear alginate hydrogel in a microfluidic device.

Future work

Future work will involve exploring the parameter space for the deposition conditions to determine optimal conditions for depositing and culturing many cell types in addition to *E. coli*. Perhaps not an obvious part of this parameter space characterization is the study of how media components contribute to autofluorescence, which thus far has limited the use of fluorophores to fluorophores that emit at wavelengths beyond green. Finally, development of this technique into creating structures with multiple layers containing different cell types or an array of fluorescent/luminescent biosensors would be beneficial for the field.

New nonviral nucleic acid delivery method

The ability to deliver nucleic acids to a cell effectively enables a researcher to reprogram the cell to execute a desired genetic program. This process, called “transformation” in bacteria, has been essential to modern biotechnology. We developed a new transformation technique that allows electrocompetent cells to be transformed as they are immobilized within a calcium alginate hydrogel in response to an electric field. The conditions for transformation are completely compatible with the spatially programmed assembly and entrapment of cell populations within microfluidics, which is central to much of the research by the Maryland Biochip Collaborative.

Significance

The transformation method we developed occurs outside the traditional electroporation and heat shock regimes. The discovery that low electric field strength coupled with a long exposure time leads to transformation and subsequent culture of viable cells is a significant development, as prior work has focused on high intensity electric fields with brief exposure times. This development is significant, as the voltages we used were on the order of 3V- a transformation that effectively could be performed using two alkaline batteries.

Innovation

This is the first instance of a bacterium being transformed at a low electric field- other groups have reported low voltages (but with small electrode gaps, leading to a high field) or low fields (but using large eukaryotic cells, which electroporate at lower fields). Our

evidence points to an electroporation mechanism outside the traditional parameter space of electroporation- exposure to a lower electric field for a longer period of time may have the same effect as a brief exposure to a high intensity field. This also represents the first simultaneous immobilization and transformation of a population of cells at a desired point in space and time.

Future work

The main issue to resolve with this work is the mechanism- how exactly does it work? This will be a significant challenge. If it truly is an electroporation, equations exist that can guide the inevitable downstream optimization work that must occur. If there is some contribution from Joule heating and/or the Ca^{2+} ion flux, the (largely empirical) results from the literature could also assist in optimization. After the mechanism is determined and the process optimized, new applications can be developed in the transformation of eukaryotic cells and the dynamic creation of cell-based sensor arrays.

Galvanic displacement for SERS substrate fabrication

Label-free detection of molecules using surface enhanced Raman spectroscopy allows for the direct detection of a wider range of molecules than methods that require fluorescent, isotopic, or affinity labeling. The development of a rapid and simple method to create highly enhancing SERS substrates by galvanic displacement led to the direct detection of melamine in liquid infant formula at concentrations down to 5 ppm. These substrates also produced maximum analytical enhancement factors on the order of 10^9 for Rhodamine-6G, which is on par with previous reports of substrates formed by galvanic displacement.

Significance

The push toward developing simple, field-deployable label free sensing systems will revolutionize point of care diagnostics and point of sampling analysis, leading to an overall reduction in cost and turnaround time for sample analysis. This work represents one step toward realizing that incredibly important goal. Additionally, our work with galvanic displacement on common metal objects has inspired other groups, with our paper receiving 10 citations according to Web of Science at the time of writing.

Innovation

The use of galvanic displacement on common metal objects underscored the simplicity and portability of this method. Our preliminary experiments with engineering the defect density of the oxide layer to control the galvanic displacement reaction is also a first, as very few research groups have capabilities in both SERS and ultra-high vacuum technologies like atomic layer deposition.

Future work

The most important basic science work to come out of this will be the determination of a set of reaction parameters that enable the fabrication of reproducible, (semi-)quantitative SERS substrates with the high enhancement characteristic of substrates produced by galvanic displacement. We listed several possible ways to approach this, and one of the most intriguing methods involves the engineering of defects in the oxide layer using atomic layer deposition, as we described in the chapter.

SERS of bacterial signaling molecules with galvanic displacement substrates

The ability to eavesdrop on intercellular communication using a label-free detection method such as SERS would be incredibly beneficial to the research community, hence our efforts to do just that. We were able to acquire SERS spectra for autoinducer 2 (AI-2) and some of its analogues, as well as indole. We were only able to obtain a normal Raman spectrum of *Pseudomonas* quinolone signal (PQS). None of the molecules were detectable at physiologically relevant concentrations in physiologically relevant media.

Significance

We were able to demonstrate the first SERS spectra for AI-2 and analogues. The detection of signaling molecules at any concentration in any solvent is a first step toward detection under more relevant conditions. Significant effort was exerted in employing galvanic displacement to detect these molecules under relevant conditions. The failure to detect these molecules under relevant conditions with SERS substrates formed by galvanic displacement on coins and thin metal films indicates that the combination of SERS substrates formed by galvanic displacement (with their random density of features with different nanoscale morphology), analytes (which must interact closely with the SERS substrate to exhibit surface enhancement), and environmental conditions (which can affect the degree to which surface-analyte interactions occur) are not ideally matched for the detection of these molecules under relevant conditions- this can inform future substrate choice for label-free detection of signaling molecules.

Innovation

Several variations of the galvanic displacement reaction were employed, some of which resulted in interesting substrate morphologies that warrant future investigation. We acquired the first known SERS spectra of AI-2 and three of its aromatic analogues, as well as a normal Raman spectrum of PQS.

Future work

A lot of work remains to be done here, which could potentially prove quite useful to the understanding of intercellular communication by bacteria. On the label-free detection front, employing any of a number of possible alternative SERS substrate fabrication methods and/or capping agents may lead to better detection limits under more relevant conditions. The spectra that we have acquired can be studied and paired with density functional theory (DFT) calculations. Combined experimental and DFT studies can help future researchers better understand the spectra generated by these signaling molecules. Finally, for the goal of eavesdropping on intercellular communication mediated by AI-2, a biosensor approach based on the AI-2 binding protein LsrB may prove more fruitful.

Conclusions

Several years ago, we set out to build a microfluidic device that would allow us to culture separate populations of bacteria and detect intercellular signaling between these populations *in situ* and in real time. This was an incredibly ambitious undertaking that was tempered by the realities of the omnipresent forces that every scientist and engineer encounters, namely “time” and “the laws of physics”. However, in attempting to achieve

this goal, we have developed new processes and techniques that expand the capabilities of researchers worldwide across many disciplines and subdisciplines, each one related in some way to the overall field of “bioengineering”. Additionally, and this is no small matter to me, this experience has afforded me the opportunity to learn and grow into becoming an independent scientist.

References

1. Ng, W.-L. and B.L. Bassler, *Bacterial Quorum-Sensing Network Architectures.* Annual Review of Genetics, 2009. **43**: p. 197-222.

2. Ito, A., et al., *Increased Antibiotic Resistance of Escherichia coli in Mature Biofilms.* Applied and Environmental Microbiology, 2009. **75**: p. 4093-4100.

3. Potera, C., *Forging a Link Between Biofilms and Disease.* Science, 1999. **283**: p. 1837-1839.

4. Collier, D.N., et al., *A bacterial cell to cell signal in the lungs of cystic fibrosis patients.* FEMS Microbiology Letters, 2002. **215**: p. 41-46.

5. Shi, X.-W., et al., Electroaddressing of Cell Populations by Co-Deposition with Calcium Alginate Hydrogels. Advanced Functional Materials, 2009. **19**: p. 2074-2080.

6. Cheng, Y., et al., Biocompatible multi-address 3D cell assembly in microfluidic devices using spatially programmable gel formation. Lab on a Chip, 2011. **11**: p. 2316-2318.

7. Cheng, Y., et al., Electroaddressing Functionalized Polysaccharides as Model Biofilms for Interrogating Cell Signaling. Advanced Functional Materials, 2012. **22**: p. 519-528.

8. Tsao, C.-Y., et al., Autonomous induction of recombinant proteins by minimally rewiring native quorum sensing regulon of E. coli. Metabolic Engineering, 2010. **10**: p. 291-297.

9. Wu, H.-C., et al., Autonomous bacterial localization and gene expression based on nearby cell receptor density. Molecular Systems Biology, 2013. **9**: p. 636.

10. Betz, J.F., et al., Optically clear alginate hydrogels for spatially controlled cell entrapment and culture at microfluidic electrode surfaces. Lab on a Chip, 2013. **13**: p. 1854-1858.

11. Huh, D., et al., *Microengineered physiological biomimicry: Organs-on-Chips.* Lab on a Chip, 2012. **12**: p. 2156-2164.

12. Chung, B.G., et al., Microfluidic fabrication of microengineered hydrogels and their application in tissue engineering. Lab on a Chip, 2012. **12**: p. 45-59.

13. Dvir, T., et al., *Nanotechnological strategies for engineering complex tissues.* Nature Nanotechnology, 2011. **6**: p. 13-22.

14. Lee, K.Y. and D.J. Mooney, *Alginate: Properties and biomedical applications.* Progress in Polymer Science, 2012. **37**: p. 106-126.

15. Hunt, N.C. and L.M. Grover, *Cell encapsulation using biopolymer gels for regenerative medicine.* Biotechnology Letters, 2010. **32**: p. 733-742.

16. Braschler, T., et al., Fluidic microstructuring of alginate hydrogels for the single cell niche. Lab on a Chip, 2010. **10**: p. 2271-2277.

17. Yu, L., M.C.W. Chen, and K.C. Cheung, Droplet-based microfluidic system for multicellular tumor spheroid formation and anticancer drug testing. Lab on a Chip, 2010. **10**: p. 2424-2432.

18. Huang, K.-S., et al., In situ synthesis of twin monodispersed alginate microparticles. Soft Matter, 2011. **7**: p. 6713-6718.

19. Kim, C., et al., Generation of core-shell microcapsules with three-dimensional focusing device for efficient formation of cell spheroid. Lab on a Chip, 2011. **11**: p. 246-252.

20. Mazzitelli, S., et al., Optimised production of multifunctional microfibres by microfluidic chip technology for tissue engineering applications. Lab on a Chip, 2011. **11**: p. 1776-1785.

21. Hu, Y., et al., Shape controllable microgel particles prepared by microfluidic combining external ionic crosslinking. Biomicrofluidics, 2012. **6**: p. 026502.

22. Kang, E., et al., Microfluidic Spinning of Flat Alginate Fibers with Grooves for Cell-Aligning Scaffolds. Advanced Materials, 2012. **24**: p. 4271-4277.

23. Kim, C., et al., In vitro angiogenesis assay for the study of cell-encapsulation therapy. Lab on a Chip, 2012. **12**: p. 2942-2950.

24. Luo, X., et al., Biofabrication of stratified biofilm mimics for observation and control of bacterial signaling. Biomaterials, 2012. **33**: p. 5136-5143.

25. Martinez, C.J., et al., A Microfluidic Approach to Encapsulate Living Cells in Uniform Alginate Hydrogel Microparticles. Macromolecular Bioscience, 2012. **12**: p. 946-951.

26. Nam, J., et al., Density-dependent separation of encapsulated cells in a microfluidic channel by using a standing surface acoustic wave. Biomicrofluidics, 2012. **6**: p. 024120.

27. Cheng, Y., et al., *Mechanism of anodic electrodeposition of calcium alginate.* Soft Matter, 2011. **7**: p. 5677-5684.

28. Yang, X., et al., In-Film Bioprocessing and Immunoanalysis with Electroaddressable Stimuli-Responsive Polysaccharides. Advanced Functional Materials, 2010. **20**: p. 1645-1652.

29. Terrell, J.L., et al., *Integrated biofabrication for electro-addressed in-film bioprocessing.* Biotechnology Journal, 2011. **7**: p. 428-439.

30. Cheng, Y., et al., In situ quantitative visualization and characterization of chitosan electrodeposition with paired sidewall electrodes. Soft Matter, 2010. **6**: p. 3177-3183.

31. Strack, R.L., et al., *A noncytotoxic DsRed variant for whole-cell labeling.* Nature Methods, 2008. **5**: p. 955-957.

32. Sambrook, J. and D. Russell, *Molecular Cloning: A Laboratory Manual (Third Edition)*. 2001: Cold Spring Harbor Laboratory Press.

33. Smith, J.A.I., et al., Biological screening of a diverse set of AI-2 analogues in Vibrio harveyi suggests that receptors which are involved in synergistic agonism of AI-2 and analogues are promiscuous. 2009. **45**: p. 7033-7035.

34. Gamby, S., et al., Altering the Communication Networks of Multispecies Microbial Systems Using a Diverse Toolbox of AI-2 Analogues. ACS Chemical Biology, 2012. **7**: p. 1023-1030.

35. Guo, M., et al., Small Molecule Inhibitors of AI-2 Signaling in Bacteria: State-of-the-Art and Future Perspectives for Anti-Quorum Sensing Agents. International Journal of Molecular Sciences, 2013. **14**: p. 17694-17728.

36. Schneider, C.A., W.S. Rasband, and K.W. Eliceiri, *NIH Image to ImageJ: 25 years of image analysis.* Nature Methods, 2012. **9**: p. 671-675.

37. Bansal, T., et al., Temporal regulation of enterohemorrhagic Escherichia coli virulence mediated by autoinducer-2. Applied Microbiology and Biotechnology, 2008. **78**: p. 811-819.

38. Carattoli, A., *Plasmids and the spread of resistance.* International Journal of Medical Microbiology, 2013. **303**: p. 298-304.

39. Arutyunov, D. and L.S. Frost, *F conjugation: back to the beginning.* Plasmid, 2013. **70**: p. 18-32.

40. Kim, J.-M., et al., *Gene delivery platforms.* Biotechnology and Bioprocess Engineering, 2013. **18**: p. 637-647.

41. Leffers, G. and V.B. Rao, A Discontinuous Headful Packaging Model for Packaging Less Than Headful Length DNA Molecules by Bacteriophage T4. Journal of Molecular Biology, 1996. **258**: p. 839-850.

42. Kumar, M., et al., Systematic Determination of the Packaging Limit of Lentiviral Vectors. Human Gene Therapy, 2001. **12**: p. 1893-1905.

43. Fielder, S. and R. Wirth, *Transformation of Bacteria with Plasmid DNA by Electroporation.* Analytical Biochemistry, 1988. **170**: p. 38-44.

44. Yoshida, N. and M. Sato, *Plasmid uptake by bacteria: a comparison of methods and efficiencies.* Applied Microbiology and Biotechnology, 2009. **83**: p. 791-798.

45. Maeda, S., A. Sawamura, and A. Matsuda, *Transformation of colonial Escherichia coli on solid media.* FEMS Microbiology Letters, 2004. **236**: p. 61-64.

46. Zimmermann, U., *Electrofusion of cells: principles and industrial potential.* Trends in Biotechnology, 1983. **1**: p. 149-155.

47. André, F. and L.M. Mir, DNA electrotransfer: its principles and an updated review of its therapeutic applications. Gene Therapy, 2004. **11**: p. S33-S42.

48. Movahed, S. and D. Li, *Microfluidics Cell Electroporation.* Microfluidics and Nanofluidics, 2011. **10**: p. 703-734.

49. Shah, D., M. Steffen, and L. Lilge, Controlled electroporation of the plasma membrane in microfluidic devices for single cell analysis. Biomicrofluidics, 2012. **6**: p. 014111.

50. Wu, M., et al., Method for Electric Parametric Characterization and Optimization of Electroporation on a Chip. Analytical Chemistry, 2013. **85**: p. 4483-4491.

51. Asada, A., et al., A Novel Gene Transformation Technique Using Water-in-Oil Droplet in an Electrostatic Field. IEEE Transactions on Industry Applications, 2013. **49**: p. 311-315.

52. Hanahan, D. and F.R. Bloom, *Mechanisms of DNA transformation*, in *Escherichia coli and Salmonella: Cellular and Molecular Biology*, F.C. Niedhardt, Editor. 1996, ASM Press: Washington, D. C., United States. p. 2449-2459.

53. Li, S., et al., *DNA transformation via local heat shock.* Applied Physics Letters, 2007. **91**: p. 013902.

54. Hong, J.W., et al., *Molecular biology on a microfluidic chip.* Journal of Physics: Condensed Matter, 2006. **18**: p. S691-S701.

55. DeLisa, M.P., et al., DNA Microarray-Based Identification of Genes Controlled by Autoinducer 2-Stimulated Quorum Sensing in Escherichia coli. Journal of Bacteriology, 2001. **183**: p. 5239-5247.

56. Pawlowicz, R., *Calculating the Conductivity of Natural Waters.* Limnology and Oceanograpy: Methods, 2008. **6**: p. 489-501.

57. Betz, J.F., Y. Cheng, and G.W. Rubloff, Direct SERS detection of contaminants in a complex mixture: rapid, single step screening for melamine in liquid infant formula. Analyst, 2012. **137**(4): p. 826-828.

58. Betz, J.F., et al., *Simple SERS substrates: Powerful, portable, and full of potential.* Physical Chemistry Chemical Physics, 2013, in revision.

59. Kneipp, K., et al., *Single Molecule Detection Using Surface-Enhanced Raman Scattering (SERS).* Physical Review Letters, 1997. **78**(9): p. 1667-1670.

60. Nie, S., Probing Single Molecules and Single Nanoparticles by Surface-Enhanced Raman Scattering. Science, 1997. **275**(5303): p. 1102-1106.

61. Michaels, A.M., M. Nirmal, and L.E. Brus, *SERS of Individual Rhodamine 6G Molecules on Large Ag Nanocrystals.* Journal of the American Chemical Society, 1999. **121**: p. 9932-9939.

62. Qian, X.M. and S.M. Nie, Single-molecule and single-nanoparticle SERS: from fundamental mechanisms to biomedical applications. Chemical Society Reviews, 2008. **37**(5): p. 912-920.

63. Kneipp, J., H. Kneipp, and K. Kneipp, *SERS—a single-molecule and nanoscale tool for bioanalytics.* Chemical Society Reviews, 2008. **37**(5): p. 1052-1060.

64. Tripp, R.A., R.A. Dluhy, and Y. Zhao, *Novel nanostructures for SERS biosensing.* Nano Today, 2008. **3**(3-4): p. 31-37.

65. Vo-Dinh, T., H.-N. Wang, and J. Scaffidi, *Plasmonic nanoprobes for SERS biosensing and bioimaging.* Journal of Biophotonics, 2009. **3**(1-2): p. 89-102.

66. Wang, G., et al., Surface-enhanced Raman scattering in nanoliter droplets: towards high-sensitivity detection of mercury (II) ions. Analytical and Bioanalytical Chemistry, 2009. **394**(7): p. 1827-1832.

67. Mulvihill, M., et al., *Surface-Enhanced Raman Spectroscopy for Trace Arsenic Detection in Contaminated Water.* Angewandte Chemie, International Edition, 2008. **47**(34): p. 6456-6460.

68. Dasary, S.S.R., et al., Gold Nanoparticle Based Label Free SERS Probe for Ultrasensitive and Selective Detection of Trinitrotoluene. Journal of the American Chemical Society, 2009. **131**: p. 13806-13812.

69. Jarvis, R.M. and R. Goodacre, *Characterisation and identification of bacteria using SERS.* Chemical Society Reviews, 2008. **37**(5): p. 931-936.

70. Premasiri, W.R., et al., *Characterization of the Surface Enhanced Raman Scattering (SERS) of Bacteria.* Journal of Physical Chemistry B, 2005. **109**: p. 312-320.

71. Qian, X., et al., In vivo tumor targeting and spectroscopic detection with surface-enhanced Raman nanoparticle tags. Nature Biotechnology, 2007. **26**(1): p. 83-90.

72. Zavaleta, C.L., et al., *Multiplexed imaging of surface enhanced Raman scattering nanotags in living mice using noninvasive Raman spectroscopy.* Proceedings of the National Academy of Sciences of the United States of America, 2009. **106**(32): p. 13511-13516.

73. Otto, A. and M. Futamata, *Electronic Mechanisms of SERS*, in *Surface-Enhanced Raman Scattering: Physics and Applications*, K. Kneipp, M. Moskovits, and H. Kneipp, Editors. 2006, Springer-Verlag: Berlin. p. 147-182.

74. Schatz, G.C., M.A. Young, and R.P. Van Duyne, *Electromagnetic mechanism of SERS*, in *Surface-Enhanced Raman Scattering - Physics and Applications*, K. Kneipp, M. Moskovits, and H. Kneipp, Editors. 2006, Springer-Verlag: Berlin. p. 19-45.

75. Ko, H., S. Singamaneni, and V.V. Tsukruk, *Nanostructured Surfaces and Assemblies as SERS Media.* Small, 2008. **4**(10): p. 1576-1599.

76. Lin, X.-M., et al., *Surface-enhanced Raman spectroscopy: substrate-related issues.* Analytical and Bioanalytical Chemistry, 2009. **394**(7): p. 1729-1745.

77. Mulvihill, M.J., et al., Anisotropic Etching of Silver Nanoparticles for Plasmonic Structures Capable of Single-Particle SERS. Journal of the American Chemical Society, 2010. **132**: p. 268-274.

78. Munro, C.H., et al., Characterization of the Surface of a Citrate-Reduced Colloid Optimized for Use as a Substrate for Surface-Enhanced Raman Scattering. Langmuir, 1995. **11**: p. 3712-3720.

79. Tao, A., et al., Langmuir-Blodgett Silver Nanowire Monolayers for Molecular Sensing Using Surface-Enhanced Raman Spectroscopy. Nano Letters, 2003. **3**(9): p. 1229-1233.

80. Tao, A., P. Sinsermsuksakul, and P. Yang, *Tunable plasmonic lattices of silver nanocrystals.* Nature Nanotechnology, 2007. **2**(7): p. 435-440.

81. Fan, M. and A.G. Brolo, Silver nanoparticles self assembly as SERS substrates with near single molecule detection limit. Physical Chemistry Chemical Physics, 2009. **11**(34): p. 7381-7389.

82. Albrecht, M.G. and J.A. Creighton, *Anomalously Intense Raman Spectra of Pyridine at a Silver Electrode.* Journal of the American Chemical Society, 1977. **99**(15): p. 5215-5217.

83. Yang, K.-H., Y.-C. Liu, and C.-C. Yu, Simple Strategy To Improve Surface-Enhanced Raman Scattering Based on Electrochemically Prepared Roughened Silver Substrates. Langmuir, 2010. **26**(13): p. 11512-11517.

84. He, Y., et al., Fabrication of two-dimensional staggered silver nanosheets on an aluminium foil. Nanotechnology, 2005. **16**(6): p. 791-796.

85. Song, Y.-Y., et al., *Galvanic Deposition of Nanostructured Noble-Metal Films on Silicon.* Electrochem. Solid-State Lett., 2005. **8**(10): p. C148-C150.

86. Gutes, A., C. Carraro, and R. Maboudian, *Silver Nanodesert Rose as a Substrate for Surface-Enhanced Raman Spectroscopy.* ACS Applied Materials and Interfaces, 2009. **1**(11): p. 2551-2555.

87. Gutes, A., et al., *Silver Nanostructures on Silicon Based on Galvanic Displacement Process.* Journal of Physical Chemistry C, 2009. **113**(39): p. 16939-16944.

88. Sun, X., et al., *Novel Ag-Cu substrates for surface-enhanced Raman scattering.* Materials Letters, 2009. **63**: p. 2306-2308.

89. Gutes, A., C. Carraro, and R. Maboudian, *Silver Dendrites from Galvanic Displacement on Commercial Aluminum Foil as an Effective SERS Substrate.* Journal of the American Chemical Society, 2010. **132**: p. 1476-1477.

90. Klupp Taylor, R.N., et al., Facile Route to Morphologically Tailored Silver Patches on Colloidal Particles. Langmuir, 2010. **26**(16): p. 13564-13571.

91. Gu, C. and T.-Y. Zhang, Electrochemical Synthesis of Silver Polyhedrons and Dendritic Films with Superhydrophobic Surfaces. Langmuir, 2008. **24**: p. 12010-12016.

92. Zou, S. and G.C. Schatz, *Coupled Plasmonic Plasmon/Photonic Resonance Effects in SERS*, in *Surface-Enhanced Raman Scattering - Physics and Applications*, K. Kneipp, M. Moskovits, and H. Kneipp, Editors. 2006, Springer-Verlag: Berlin. p. 67-87.

93. Wang, Z., et al., *Immersion/Electroless Deposition of Cu on Ta.* Electrochemical and Solid-State Letters, 2004. **7**(5): p. C67-C69.

94. Zhang, Y., et al., Atom Probe Tomography Characterization of Thin Copper Layers on Aluminum Deposited by Galvanic Displacement. Langmuir, 2012. **28**(3): p. 1673-1677.

95. Hanson, B.A., ChemoSpec: Exploratory Chemometrics for Spectroscopy. 2013.

96. R Core Team, *R: A language and environment for statistical computing*. 2013, R Foundation for Statistical Computing: Vienna, Austria.

97. Bechelany, M., et al., Simple Synthetic Route for SERS-Active Gold Nanoparticles Substrate with Controlled Shape and Organization. Langmuir, 2010. **26**(17): p. 14364-14371.

98. Fang, J., et al., Double-interface growth mode of fractal silver trees within replacement reaction. Applied Physics Letters, 2006. **89**(17): p. 173104.

99. Kanaya, K. and S. Okayama, *Penetration and energy loss theory of electrons in solid targets.* Journal of Physics D: Applied Physics, 1972. **5**: p. 43-58.

100. Brevnov, D.A., et al., Electroless Deposition of Silver by Galvanic Displacement on Aluminum Alloyed with Copper. Journal of Physical Chemistry B, 2004. **108**: p. 17531-17536.

101. Tremaine, P.R. and J.C. Leblanc, *The solubility of nickel oxide and hydrolysis of Ni^{2+} in water to 573 K.* Journal of Chemical Thermodynamics, 1980. **12**: p. 521-538.

102. Ko, C.K. and W.G. Lee, *Effects of pH variation in aqueous solutions on dissolution of copper oxide.* Surface and Interface Analysis, 2010. **42**(6-7): p. 1128-1130.

103. Watanabe, H., et al., DFT Vibrational Calculations of Rhodamine 6G Adsorbed on Silver: Analysis of Tip-Enhanced Raman Spectroscopy. Journal of Physical Chemistry B, 2005. **109**: p. 5012-5020.

104. Zuo, C. and P.W. Jagodzinski, Surface-Enhanced Raman Scattering of Pyridine Using Different Metals: Differences and Explanation Based on the Selective Formation of α-Pyridyl on Metal Surfaces. Journal of Physical Chemistry B, 2005. **109**: p. 1788-1793.

105. Polk, B.J., et al., *Microelectroplating Silver on Sharp Edges toward the Fabrication of Solid-State Nanopores.* Journal of the Electrochemical Society, 2004. **151**(9): p. C559-C566.

106. Qu, L. and L. Dai, *Novel Silver Nanostructures from Silver Mirror Reaction on Reactive Substrates.* Journal of Physical Chemistry B, 2005. **109**: p. 13985-13990.

107. Dobson, R.L.M., et al., Identification and Characterization of Toxicity of Contaminants in Pet Food Leading to an Outbreak of Renal Toxicity in Cats and Dogs. Toxicological Sciences, 2008. **106**(1): p. 251-262.

108. Lin, M., et al., Detection of Melamine in Gluten, Chicken Feed, and Processed Foods Using Surface Enhanced Raman Spectroscopy and HPLC. Journal of Food Science, 2008. **73**(8): p. T129-T134.

109. Koglin, E., B.J. Kip, and R.J. Meier, Adsorption and Displacement of Melamine at the Ag/Electrolyte Interface Probed by Surface-Enhanced Raman Microprobe Spectroscopy. Journal of Physical Chemistry, 1996. **100**: p. 5078-5089.

110. Du, X., et al., Qualitative and Quantitative Determination of Melamine by Surface-Enhanced Raman Spectroscopy Using Silver Nanorod Array Substrates. Applied Spectroscopy, 2010. **64**(7): p. 781-785.

111. Lee, S.Y., et al., Detection of Melamine in Powdered Milk Using Surface-Enhanced Raman Scattering with No Pretreatment. Analytical Letters, 2010. **43**(14): p. 2135-2141.

112. Cheng, Y. and Y. Dong, Screening melamine contaminant in eggs with portable surface-enhanced Raman Spectroscopy based on gold nanosubstrate. Food Control, 2011. **22**(5): p. 685-689.

113. Coluccio, M.L., et al., Silver-based surface enhanced Raman scattering (SERS) substrate fabrication using nanolithography and site selective electroless deposition. Microelectronic Engineering, 2009. **85**: p. 1085-1088.

114. Brejna, P.R. and P.R. Griffiths, Electroless Deposition of Silver onto Silicon as a Method of Preparation of Reproducible Surface-Enhanced Raman Spectroscopy Substrates and Tip-Enhanced Raman Spectroscopy Tips. Applied Spectroscopy, 2010. **64**(5): p. 493-499.

115. Gutes, A., C. Carraro, and R. Maboudian, *Silver Nanodesert Rose as a Substrate for Surface-Enhanced Raman Spectroscopy.* ACS Applied Materials & Interfaces, 2009. **1**(11): p. 2551-2555.

116. Gutes, A., R. Maboudian, and C. Carraro, *Gold-Coated Silver Dendrites as SERS Substrates with an Improved Lifetime.* Langmuir, 2012. **28**(51): p. 17846-17850.

117. Song, Y.-Y., et al., *Galvanic Deposition of Nanostructured Noble-Metal Films on Silicon.* Electrochemical and Solid-State Letters, 2005. **8**(10): p. C148-C150.

118. Xie, S., et al., Fast Growth Synthesis of Silver Dendrite Cyrstals Assisted by Sulfate Ion and Its Application for Surface-Enhanced Raman Scattering. Journal of Physical Chemistry C, 2011. **115**(20): p. 9943-9951.

119. Goia, D.V. and E. Matijević, *Preparation of monodispersed metal particles.* New Journal of Chemistry, 1998. **22**(11): p. 1203-1215.

120. Lv, S., et al., Effect of additives on the morphologies of silver nanostructures prepared by galvanic displacement reaction. Solid State Sciences, 2010. **12**: p. 1287-1291.

121. Sun, Y. and Y. Xia, Shape-Controlled Synthesis of Gold and Silver Nanoparticles. Science, 2002. **298**: p. 2176-2179.

122. Gao, J., C.M. Bender, and C.J. Murphy, Dependence of the Gold Nanorod Aspect Ratio on the Nature of the Directing Surfactant in Aqueous Solution. Langmuir, 2003. **19**: p. 9065-9070.

123. Zhang, G., et al., Morphology-Controlled Green Synthesis of Single Crystalline Silver Dendrites, Dendritic Flowers, and Rods, and Their Growth Mechanism. Crystal Growth and Design, 2011. **11**: p. 2493-2499.

124. Knez, M., K. Nielsch, and L. Niinistö, *Synthesis and Surface Engineering of Complex Nanostructures by Atomic Layer Deposition.* Advanced Materials, 2007. **19**(21): p. 3425-3438.

125. Im, H., et al., Atomic layer deposition: A versatile technique for plasmonics and nanobiotechnology. Journal of Materials Research, 2012. **27**(4): p. 663-671.

126. Prindle, A., et al., *A sensing array of radically coupled genetic biopixels.* Nature, 2012. **481**: p. 39-44.

127. Dubey, G.P. and S. Ben-Yehuda, *Intercellular Nanotubes Mediate Bacterial Communication.* Cell, 2011. **144**: p. 590-600.

128. Ng, W.-L. and B.L. Bassler, *Bacterial Quorum-Sensing Network Architectures.* Annual Reviews of Genetics, 2009. **43**: p. 197-222.

129. Rajamani, S., et al., A LuxP-FRET-Based Reporter for the Detection and Quantification of AI-2 Bacterial Quorum-Sensing Signal Compounds. Biochemistry, 2007. **46**: p. 3990-3997.

130. Zhu, J. and D. Pei, *A LuxP-Based Fluorescent Sensor for Bacterial Autoinducer II.* ACS Chemical Biology, 2008. **3**: p. 110-119.

131. Zhou, L., et al., Detection of the Pseudomonas Quinolone Signal (PQS) by cyclic voltammetry and amperometry using a boron doped diamond electrode. Chemical Communications, 2011. **47**: p. 10347-10349.

132. Bukelman, O., et al., *Electrochemical analysis of quorum sensing inhibition.* Chemical Communications, 2009: p. 2836-2838.

133. Pearman, W.F., et al., Surface-Enhanced Raman Spectroscopy for in Situ Measurements of Signaling Molecules (Autoinducers) Relevant to Bacteria Quorum Sensing. Applied Spectroscopy, 2007. **61**: p. 1295-1300.

134. Globisch, D., et al., Uncharacterized 4,5-Dihydroxy-2,3-Pentanedione (DPD) Molecules Revealed Through NMR Spectroscopy: Implications for a Greater Signaling Diversity in Bacterial Species. Angewandte Chemie, International Edition, 2012. **51**: p. 4204-4208.

135. Miller, S.T., et al., Salmonella typhimurium recognizes a chemically distinct form of the bacterial quorum-sensing signal AI-2. Molecular Cell, 2004. **15**: p. 677-687.

136. Dubern, J.-F. and S.P. Diggle, Quorum sensing by 2-alkyl-4-quinolones in Pseudomonas aeruginosa and other bacterial species. Molecular BioSystems, 2008. **4**: p. 882-888.

137. Huse, H. and M. Whiteley, *4-Quinolones: Smart Phones of the Microbial World.* Chemical Reviews, 2011. **111**: p. 152-159.

138. Schertzer, J.W., M.L. Boulette, and M. Whiteley, *More than a signal: non-signaling properties of quorum sensing molecules.* Trends in Microbiology, 2009. **17**: p. 189-195.

139. Wang, D., X. Ding, and P.N. Rather, *Indole Can Act as an Extracellular Signal in Escherichia coli.* Journal of Bacteriology, 2001. **183**: p. 4210-4216.

140. Lee, J.-H. and J. Lee, *Indole as an intercellular signal in microbial communities.* FEMS Microbiology Reviews, 2010. **34**: p. 426-444.

141. Han, T.H., et al., *Environmental factors affecting indole production in Escherichia coli.* Research in Microbiology, 2011. **162**: p. 108-116.

142. Chu, W., et al., Indole Production Promotes Escherichia coli Mixed-Culture Growth with Pseudomonas aeruginosa by Inhibiting Quorum Signaling. Applied and Environmental Microbiology, 2012. **78**: p. 411-419.

143. Lee, H.H., et al., Bacterial charity work leads to population-wide resistance. Nature, 2010. **467**: p. 82-85.

144. Deng, S.D. and J.P.M. Schelvis, Analysis of Measured and Calculated Raman Spectra of Indole, 3-Methylindole, and Tryptophan on the Basis of Observed and Predicted Isotope Shifts. Journal of Physical Chemistry A, 2010. **114**: p. 10897-10905.

145. Gao, P., D. Gosztola, and M.J. Weaver, Surface-Enhanced Raman Spectroscopy as a Probe of Electroorganic Reaction Pathways. 1. Processes Involving Adsorbed Nitrobenzene, Azobenzene, and Related Species. Journal of Physical Chemistry, 1988. **92**: p. 7122-7130.

146. Lee, P.C. and D. Meisel, *Adsorption and Surface-Enhanced Raman of Dyes on Silver and Gold Sols.* Journal of Physical Chemistry, 1982. **86**: p. 3391-3395.